

OCEAN

ENGINEERING

GROUP

Propeller Lifting Line/Rudder Interaction

Fahad Mohammed

August 2006

Report No. 06-2

ENVIRONMENTAL AND WATER RESOURCES ENGINEERING

DEPARTMENT OF CIVIL ENGINEERING

THE UNIVERSITY OF TEXAS AT AUSTIN

Austin, TX 78712

Copyright
by
Fahad Mohammed
2006

Propeller Lifting Line/Rudder interaction

by

Fahad Mohammed, B.Tech.

Thesis

Presented to the Faculty of the Graduate School
of The University of Texas at Austin
in Partial Fulfillment
of the Requirements
for the Degree of

Master of Science in Engineering

The University of Texas at Austin

August 2006

Propeller Lifting Line/Rudder interaction

APPROVED BY
SUPERVISING COMMITTEE:

Supervisor: _____
Spyros A. Kinnas

Reader: _____
Kamy Sepehrnoori

To my parents, my brother and sister and all my friends.

Acknowledgements

I would like to take this opportunity to thank several people whose constant support, guidance and encouragement were invaluable during my research work and helped me complete my Masters thesis.

At the onset, I would like to thank my supervisor, Dr. Spyros A. Kinnas with greatest appreciation. I am especially grateful for his unending support and guidance, which helped me immensely during the course of my graduate studies and research. I am thankful to him for his understanding nature.

I would also like to thank Dr. Kamy A. Sepehrnoori for agreeing to be my reader despite his busy schedule. His comments, assistance and encouragement were invaluable to give this thesis its final shape.

I would like to thank my parents, my sister Farah, my brother Faizan and my friends, especially Shashank, Shiva and Shankar who stood by me throughout this time and encouraged me to move on at every fallen step.

I would like to thank the members of the Computational Hydrodynamics Laboratory, Dr. Hanseong Lee, Mr. Hua Gu, Mr. Yi-Hsiang Yu, Ms. Hong Sun, Mr. Vimal Vinayan, Mr. Bikash Mishra, Mr. Yumin Deng and Mr. Lei He for their unending support and suggestions. It is with great fondness that I would like to thank Mr. Yoonsik Hwang and Dr. Ilsung Moon for their advice and concern.

Support for this research was provided by Phase IV of the “Consortium

on Cavitation Performance of High Speed Propulsors” with the following members: AB Volvo Penta, American Bureau of Shipping, Daewoo Shipbuilding and Marine Engineering Co. Ltd., Kawasaki Heavy Industries, Naval Surface Warfare Center Carderock Division, Office of Naval Research (Contract N0001404-1-0287), Rolls-Royce Marine AB, Rolls-Royce Marine AS, VA Tech Escher Wyss GMBH, Wärtsilä Propulsion Netherlands B.V., Wärtsilä Propulsion Norway AS and Wärtsilä CMEZ Propeller Co. Ltd. Partial support of this work was also provided by the Office of Naval Research under the National Naval Responsibility for Naval Engineering (NNR-NE) program, through Florida Atlantic University (Subagreement TRD67).

In the end, I would like to thank the excellent faculty of the College of Engineering at the University of Texas at Austin for the excellent education they provided.

Propeller Lifting Line/Rudder interaction

by

Fahad Mohammed, M.S.E.

The University of Texas at Austin, 2006

SUPERVISOR: Spyros A. Kinnas

A complete understanding of the flow dynamics around a rudder will help us create accurate models for flow around rudder. These models will help us study completely unsteady propeller rudder interactions and create efficient rudder design by accurately predicting the cavitation on the rudder surface. The effect of the cavitating tip vortex on the rudder needs to be studied to model truly unsteady propeller/rudder interaction and study its effect on cavitation.

At first, the vortex/hydrofoil interactions are modelled using a commercial CFD solver, FLUENT. The dynamics of a 2D vortex in a uniform flow and a 3D vortex/hydrofoil interaction is studied. Various grid and time stepping scheme dependence studies are performed to understand the modeling nuances of vortex/hydrofoil interactions using a CFD solver and to control the amount of vortex dissipation.

Next, the vortex/hydrofoil interactions were modelled as a line vortex/hydrofoil interaction model using a BEM based flow solver, PROPCAV. PROPCAV solves for

the flow around the hydrofoil including the effects of a line vortex. After solving for the foil, total velocity at the line vortex location is evaluated and the vortex is convected with this velocity. The pressure distribution on the foil surface is obtained to evaluate the effect of the vortex on the hydrofoil.

Then a lifting line model for a propeller was used to model the alignment of the tip vortex wake with the total flow velocities to maintain the force free condition on the wake. This alignment model was coupled with the line vortex/hydrofoil interaction model to evaluate the effect of the tip vortex wake on the hydrofoil. This tip vortex/hydrofoil interaction model is truly unsteady and at each lifting line angle, the minimum pressure on the foil surface was obtained to study its variation with the lifting line angle.

The objective of this research is to predict the pressure distribution on the foil surface in the presence of a vortex and study the variation of minimum pressure with the lifting line blade angle.

Table of Contents

Acknowledgements	v
Abstract	vii
List of Figures	xi
Nomenclature	xv
Chapter 1. Introduction	1
1.1 Background	1
1.2 Motivation	2
1.3 Objectives	5
1.4 Overview	6
Chapter 2. Literature Review	8
2.1 Vortex Hydrofoil Interactions	8
2.2 Boundary Element Method	10
Chapter 3. Mathematical Formulation	12
3.1 Boundary Element Method for flow around hydrofoils	12
3.1.1 Background	12
3.1.2 Governing Equation	13
3.1.3 Boundary Conditions	14
3.1.4 Green's Theorem	15
3.1.5 Green's formula for a three dimensional body	16
3.1.6 Green's formula for hydrofoil	18
3.1.7 Numerical Implementation	19
3.2 Line Vortex/hydrofoil interactions using BEM	21
3.2.1 The Biot-Savart Law	21

3.2.2	Velocity induced by a line vortex in a 3D space	22
3.2.3	Numerical Implementation	25
3.2.4	BEM formulation for line vortex/hydrofoil interaction	27
3.3	Propeller flows as lifting line flows	28
3.4	Lifting line wake alignment	30
3.5	Lifting line tip vortex/hydrofoil interactions	37
Chapter 4.	Vortex/Hydrofoil Interactions Using FLUENT	40
4.1	2D Vortex in uniform flow	41
4.2	3D Vortex/hydrofoil interactions in a uniform flow	59
Chapter 5.	Vortex/Hydrofoil Interactions Using PROPCAV	74
5.1	Line Vortex/Hydrofoil interactions using PROPCAV, a BEM solver	75
5.2	Convergence studies	81
Chapter 6.	Lifting Line Wake alignment	88
6.1	Alignment results for a vortex ring	88
6.2	Convergence studies on a vortex ring	91
6.3	Alignment Results for Lifting Line Tip Vortex	94
6.4	Convergence tests for helical wake	99
Chapter 7.	Lifting Line Tip Vortex/Rudder interactions	109
7.1	Lifting Line tip vortex/hydrofoil interactions	109
Chapter 8.	Conclusions	117
8.1	Conclusions	117
8.2	Recommendations for Future Work	119
Vita		126

List of Figures

1.1	The tip vortices impinging on a rudder as seen in an experiment by Kracht [1989a,b].	3
1.2	The tip vortices impinging on a rudder at an angle of attack as seen in experiment by Kracht [1989a,b].	4
3.1	Potential Flow around a hydrofoil.	14
3.2	Volume ν enclosed by boundary S , adjusted from Kinnas [2006]. . .	16
3.3	Body B and unit source P , adjusted from Kinnas [2006].	17
3.4	Discretized hydrofoil with the wake under an inflow velocity \vec{V}_{in} . . .	20
3.5	Velocity induced at point P by a vortex segment.	22
3.6	Velocity induced at point P by a segment 1-2 of a line vortex.	23
3.7	Vortex self-induced velocity model.	24
3.8	Lifting Line with the tip vortex wake.	29
3.9	Lifting line tip vortex wake alignment process.	33
3.10	Angular velocity transformation in $y - z$ plane.	36
3.11	Lifting line tip vortex/rudder system.	38
4.1	Tangential velocity distribution for a Rankine vortex.	41
4.2	The domain and the grid for a 2D vortex in uniform flow for 5 grid points across the vortex core.	42
4.3	Vortex positions through vorticity contours shown at times (a) $t = 0$, (b) $t = 50\Delta t$, (c) $t = 100\Delta t$, (d) $t = 150\Delta t$, (e) $t = 200\Delta t$ and (f) $t = 250\Delta t$. $\Delta t = 0.001 \text{ sec}$ and $u_{in} = 5 \text{ m/s}$	47
4.4	Vorticity contours shown for (a) $\frac{r_0}{\Delta x} = 2$, (b) $\frac{r_0}{\Delta x} = 5$, (c) $\frac{r_0}{\Delta x} = 10$ and (d) $\frac{r_0}{\Delta x} = 20$ at $t = 0$. $r_o^* = 0.02$, $u_{in} = 5.0 \text{ m/s}$ and $\Delta t = 0.001 \text{ sec}$	49
4.5	Vorticity contours shown for (a) $\frac{r_0}{\Delta x} = 2$, (b) $\frac{r_0}{\Delta x} = 5$, (c) $\frac{r_0}{\Delta x} = 10$ and (d) $\frac{r_0}{\Delta x} = 20$ at $t = 50\Delta t$. $r_o^* = 0.02$, $u_{in} = 5.0 \text{ m/s}$ and $\Delta t = 0.001 \text{ sec}$	50

4.6	Vorticity contours shown for (a) $\frac{r_0}{\Delta x} = 2$, (b) $\frac{r_0}{\Delta x} = 5$, (c) $\frac{r_0}{\Delta x} = 10$ and (d) $\frac{r_0}{\Delta x} = 20$ at $t = 100\Delta t$. $r_o^* = 0.02$, $u_{in} = 5.0$ m/s and $\Delta t = 0.001$ sec.	51
4.7	Vorticity contours shown for (a) $\frac{r_0}{\Delta x} = 2$, (b) $\frac{r_0}{\Delta x} = 5$, (c) $\frac{r_0}{\Delta x} = 10$ and (d) $\frac{r_0}{\Delta x} = 20$ at $t = 100\Delta t$. $r_o^* = 0.02$, $u_{in} = 5.0$ m/s and $\Delta t = 0.001$ sec.	52
4.8	Comparison of vorticity magnitudes at (a) $t = 50\Delta t$, (b) $t = 100\Delta t$ and (c) $t = 150\Delta t$ between 1 st and 2 nd order implicit unsteady scheme.	54
4.9	Vorticity contours shown at $t = 50\Delta t$ for <i>Laminar</i> and $k - \epsilon$ models. $\Delta t = 0.001$ sec.	56
4.10	Vorticity contours shown at $t = 100\Delta t$ for <i>Laminar</i> and $k - \epsilon$ models. $\Delta t = 0.001$ sec.	57
4.11	Vorticity contours shown at $t = 150\Delta t$ for <i>Laminar</i> and $k - \epsilon$ models. $\Delta t = 0.001$ sec.	58
4.12	Domain for 3d vortex/hydrofoil interactions.	59
4.13	The 3D grid in the (a) $x - y$ plane at $z = -0.25$ and (b) $x - z$ plane at $y = 0.05$	60
4.14	Vorticity contours shown in the $x - y$ plane at (a) $t = 0$, (b) $t = 100\Delta t$, (c) $t = 200\Delta t$, (d) $t = 300\Delta t$, and (e) $t = 400\Delta t$. $\Delta t = 0.001$ sec and $u_{in} = 1.0$ m/s.	64
4.15	Contours of C_P on the foil surface shown at times (a) $t = 100\Delta t$, (b) $t = 200\Delta t$, (c) $t = 300\Delta t$, (d) $t = 400\Delta t$ and (e) $t = 500\Delta t$	66
4.16	The grid for a vortex/cambered foil interaction shown in the $x - y$ plane.	67
4.17	The grid for a vortex/cambered foil interaction shown in the $x - z$ plane.	68
4.18	Vorticity magnitude in x-y plane for (a) $t = 0$, (b) $t = 150\Delta t$, (c) $t = 300\Delta t$ and (d) $t = 450\Delta t$. $\Delta t = 0.001$ and $U_{in} = 1.0$	70
4.19	Contours of C_P over the foil surface at (a) $t = 150\Delta t$, (b) $t = 300\Delta t$ and (c) $t = 450\Delta t$	73
5.1	The domain for vortex/hydrofoil interaction model.	76
5.2	The numerical limit L_T defined around the hydrofoil.	76
5.3	Vortex movement towards the hydrofoil at different times.	78

5.4	$-C_P$ along the leading edge of the foil at (a) $t^* = 0$, (b) $t^* = 6\Delta T$, (c) $t^* = 12\Delta T$ and (d) $t^* = 18\Delta T$. $\Delta T = 0.01$	79
5.5	Contours of C_P at (a) $t^* = 0$, (b) $t^* = 6\Delta T$, (c) $t^* = 12\Delta T$ and (d) $t^* = 18\Delta T$. $\Delta T = 0.01$	80
5.6	Vortex position around the hydrofoil for different limits at $t^* = 12\Delta T$ and $t^* = 18\Delta T$. $\Gamma^* = 0.05$ and $V_a^* = 1.0$	82
5.7	The pressure distribution on the leading edge at $t^* = 12\Delta T$ and $t^* = 18\Delta T$ for different values of the numerical limit L_T	83
5.8	Convergence of leading edge pressure for the foil discretization shown in figure legend at $t^* = 12\Delta T$	84
5.9	Pressure contours shown on the foil at $t^* = 18\Delta T$ for different spanwise discretizations of the foil: (a) 80×10 , (b) 80×20 , (c) 80×30 , (d) 80×40 , (e) 80×50 and (f) 80×60	86
5.10	Pressure contours shown on the foil at $t^* = 18\Delta T$ for different chordwise discretizations of the foil: (a) 20×40 , (b) 40×40 , (c) 60×40 and (d) 80×40	87
6.1	Discretized vortex ring with the direction of motion.	89
6.2	Convection of the vortex ring in the axial direction. The location of the ring is shown for every $10\Delta T$ from $t = 0$ to $t = 40\Delta T$	90
6.3	Induced velocity on the vortex ring (a) without and (b) with the self induced velocity of the vortex elements.	93
6.4	Lifting line system with the tip vortex wake.	94
6.5	Initial wake geometry, aligned wake geometry at iteration step t_c and wake geometry at $t_c - 1$ is shown for $\Gamma^* = 0.1$	95
6.6	Velocity vectors along the aligned wake for $\Gamma^* = 0.1$ and $\Delta\theta = 12^\circ$	96
6.7	Angle α in degrees between the velocity vector \vec{V}_{tot} and the directional vector \vec{dr} along the aligned wake at the initial step, the converged iteration step t_c and $t_c - 1$ for $\Gamma^* = 0.1$ and $\Delta\theta = 12^\circ$	97
6.8	The error ΔX_{err} along the wake after the initial iteration step, the converged iteration step t_c and $t_c - 1$ for $\Gamma^* = 0.1$ and $\Delta\theta = 12^\circ$	98
6.9	L^2 norm of the error ΔX_{err} at the iteration steps I for $\Gamma^* = 0.1$ and $\Delta\theta = 12^\circ$	98
6.10	Convergence of aligned wake for $\Delta\theta = 12^\circ, 6^\circ$ and 3° . The vortex strength, $\Gamma^* = 0.1$ and $J = 1.0$	99
6.11	$(u, v, w)_{wk}$ along the tip vortex wake for $\Delta\theta = 12^\circ, 6^\circ$ and 3° . $\Gamma^* = 0.1$ and $J = 1.0$	101
6.12	α along the tip vortex wake for $\Delta\theta = 12^\circ, 6^\circ$ and 3° . $\Gamma^* = 0.1$ and $J = 1.0$	102

6.13	Initial tip vortex wake geometry for $0.5P$, P and $2P$, where P is the original pitch for the inflow conditions. $\Gamma^* = 0.1$, $J = 1.0$ and $\Delta\theta = 12^\circ$	103
6.14	Aligned tip vortex wake geometry for initial pitch of $0.5P$, P and $2P$. $\Gamma^* = 0.1$, $J = 1.0$ and $\Delta\theta = 12^\circ$	103
6.15	α along the aligned tip vortex wake geometry for initial pitch of $0.5P$, P and $2P$. $\Gamma^* = 0.1$, $J = 1.0$ and $\Delta\theta = 12^\circ$	104
6.16	Initial wake geometry for 2, 4 and 8 revolutions of the transition wake. $\Gamma^* = 0.1$, $J = 1.0$ and $\Delta\theta = 12^\circ$	105
6.17	Convergence of aligned wake geometry for 2, 4 and 8 revolutions of the transition wake. $\Gamma^* = 0.1$, $J = 1.0$ and $\Delta\theta = 12^\circ$	106
6.18	α along the aligned tip vortex wake for 2, 4 and 8 revolutions of the transition wake. $\Gamma^* = 0.1$, $J = 1.0$ and $\Delta\theta = 12^\circ$	106
6.19	Initial wake geometry for 4, 8 and 16 revolutions of the ultimate wake. $\Gamma^* = 0.1$, $J = 1.0$ and $\Delta\theta = 12^\circ$	107
6.20	Convergence of aligned wake geometry for 4, 8 and 16 revolutions of the ultimate wake. $\Gamma^* = 0.1$, $J = 1.0$ and $\Delta\theta = 12^\circ$	108
6.21	α along the aligned tip vortex wake for 4, 8 and 16 revolutions of the ultimate wake. $\Gamma^* = 0.1$, $J = 1.0$ and $\Delta\theta = 12^\circ$	108
7.1	The lifting line tip vortex/hydrofoil interaction model.	110
7.2	Contours of $-C_P$ on the foil for the lifting line location of (a) $\delta_k = 0^\circ$, (b) $\delta_k = 90^\circ$, (c) $\delta_k = 180^\circ$ and (d) $\delta_k = 270^\circ$	113
7.3	α° along the aligned tip vortex wake.	114
7.4	$-C_{P_{min}}$ on the foil surface at different lifting line angles.	115
7.5	$-C_{P_{min}}$ along lifting line angle for $\Delta\theta = 12^\circ$, 6° , and 3°	115
7.6	Convergence of the aligned tip vortex wake at (a) $\delta_k = 0^\circ$ and (b) $\delta_k = 180^\circ$ for $\Delta\theta = 12^\circ$, 6° , and 3°	116

Nomenclature

Latin Symbols

- A_{ij} dipole influence coefficients
- B_{ij} source influence coefficients
- A assembled matrix of dipole influence coefficients
- a vortex core radius
- B assembled matrix of source influence coefficients
- B a body in space
- C_p pressure coefficient,
 $C_p = (P - P_o)/(0.5\rho n^2 D^2)$ for propeller
 $C_p = (P - P_o)/(0.5\rho U_{in}^2)$ otherwise
- D propeller diameter, $D = 2R$
- F Green's function
- G Green's function
- J advance ratio based on V_a , $J = V_a/nD$
- L reference length used in non-dimensionalization
- n propeller rotational frequency (rev/s), or
- \hat{n} normal direction vector
- P pressure, or
pitch of the propeller/lifting line
- P_o far upstream pressure, at the propeller axis

p, q	field point and variable point
\vec{q}	velocity field
R	propeller/lifting line radius, or distance between the field and variable points
Re	Reynolds number based on reference length L , $Re = \frac{\rho U_{\infty} L}{\mu}$
r	distance between points in space, $r = \vec{r} $
S	bounding surface
t	time
U_{in}	inflow/far field velocity magnitude
u, v, w	x, y and z -direction velocities
\vec{V}	Velocity field
\vec{V}_{tot}	total velocity field
\vec{V}_{in}	inflow velocity field
\vec{V}_{wk}	lifting line tip vortex wake induced velocity field
\vec{V}_{rud}	velocity field induced by the hydrofoil and its wake
V_a	axial inflow velocity
V_t	tangential inflow velocity
\vec{X}	location vector on the lifting line fixed system, $\vec{X} = (x, y, z)$ coordinate system
Z	number of lifting lines/propeller blades

Greek Symbols

α	angle between the total velocity vectors and wake elements
β	pitch angle of the lifting line wake
γ	vorticity
Γ	propeller blade/lifting line, line vortex circulation
δ_k	lifting line/propeller blade angle of the k^{th} blade
ΔT	non dimensional time step size
Δt	time step size
$(\Delta x, \Delta y)$	cell size in x and y direction
θ	angular coordinate of the lifting line tip vortex wake
κ	turbulence kinetic energy
ϵ	turbulence dissipation rate
μ	dynamic viscosity of water
ν	kinematic viscosity of water
ϕ	perturbation potential
Φ	total potential
ρ	fluid density
ω	propeller angular velocity

Subscripts

$1, 2, 3, 4, \dots$	node numbers
tot, in, wk, rud	total, inflow, wake induced and hydrofoil induced velocities

Superscripts

- * non dimensional variables
- $t, t + 1$ iteration step indices

Acronyms

- BEM Boundary Element Method
- CFD Computational Fluid Dynamics
- CPU Central Processing Unit (time)
- DBC Dynamic Boundary Condition
- FVM Finite Volume Method
- KBC Kinematic Boundary Condition
- MIT Massachusetts Institute of Technology
- NACA National Advisory Committee for Aeronautics
- RANS Reynolds Averaged Navier-Stokes(equations)
- RSM Reynolds Stress Model
- TE Trailing Edge

Computer Program Names

- PROPCAV cavitating propeller potential flow solver based on BEM
- FLUENT commercial CFD software

Chapter 1

Introduction

1.1 Background

A marine rudder is essential for the maneuverability, directional control and the steering of any ship. The rudders are typically placed in the aft of the ship, behind a propeller, in the slipstream of a propeller. Rudders operate by redirecting the flow of water past the hull, thus imparting a turning moment to the ship. The effectiveness of a rudder in producing a turning moment is proportional to the amount of lift generated by the rudder.

The problem of cavitation on the rudder surface is an important issue in the design of a rudder. Cavitation on a rudder produces undesirable effects on it, thus decreasing the efficiency of a rudder in the maneuverability of any ship. It may lead to increased loads and erosion on the rudder surface, thereby greatly reducing the performance of the rudder. It may also lead to unwanted acoustic effects on the hull and vibrations on the rudder and the adjoining hull. The various forms of cavitation that can affect the rudder are sheet cavitation, which can occur on either the face side or the back side of the rudder, gap cavitation, which occurs due to low pressures in the gap between the rudder and hull and tip vortex cavitation which can occur due to the tip vortex bursting or due to the low pressures induced by the tip vortices on the rudder.

Cavitation is an important phenomenon that occurs when the pressure falls below the vapour pressure. This causes the formation of cavities, which on bursting could lead to the material erosion. This subsequently could lead to the loss of performance of the rudder. This makes it essential to study all the possible sources of rudder cavitation.

A complete understanding of the flow dynamics that take place in the vicinity of a rudder can help us to accurately model the flow around it and obtain efficient rudder designs. A particularly interesting and important phenomenon is the interaction of the propeller blade tip vortices with the rudder. The tip vortices from the propeller blade tip, impinging on the rudder are seen in Figs. 1.1 and 1.2. The curling of the tip vortices around the rudder and the tip vortex wake contraction can also be seen in these figures.

These tip vortices are cavitating vortices, i.e these vortices have a cavity core. Since these vortices induce a low pressure on the rudder surface it is important to analyse the effects, if any, of these tip vortices on the process of cavitation on the rudder surface. Since these vortices impinge with a regular frequency, based on the rotational speed of the propeller, on the rudder, it is also important to analyse the effect of these vortices on the vibrational aspects of the rudder and the hull and the creation of acoustic noise as well.

1.2 Motivation

The advancement of ship technology has led to increased loads on the ship propellers. This increases the complexity of the vortical inflow to the rudder. Hence, a

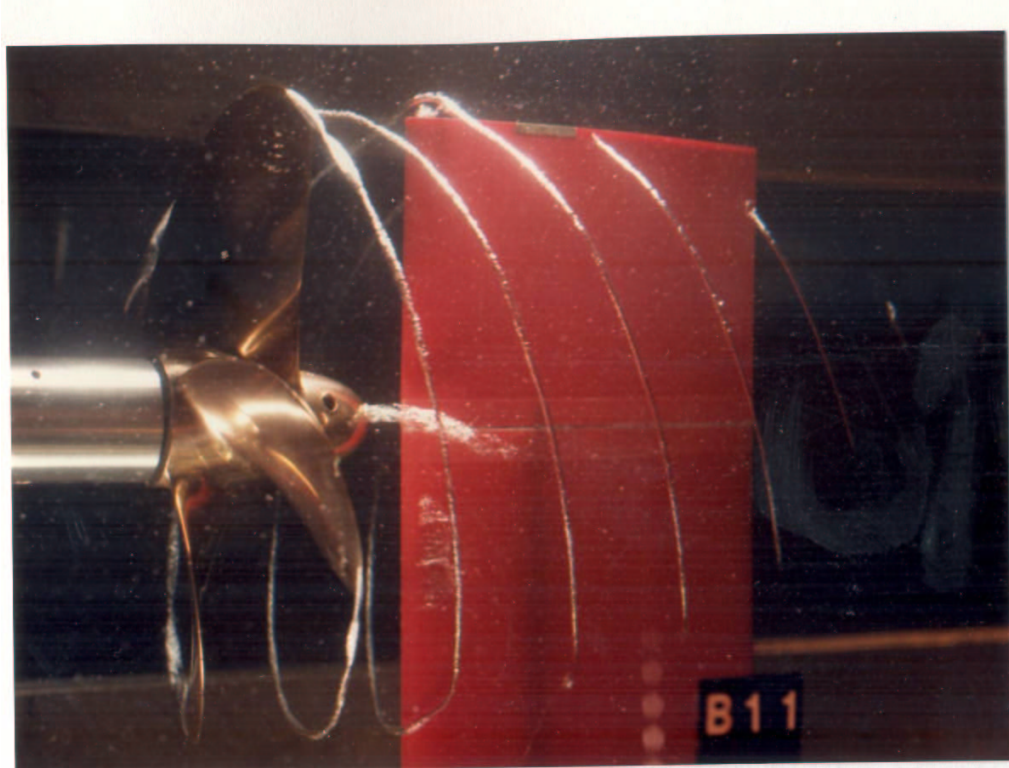


Figure 1.1: The tip vortices impinging on a rudder as seen in an experiment by Kracht [1989a,b].

complete understanding of the flow dynamics around a rudder will help us to create efficient rudder designs and accurate numerical models of the flow around a rudder. These models can help us to study all the possible sources of cavitation on a rudder and lead to better models of cavity prediction on the rudder surface. Thus, it is essential to study all the possible sources of cavitation on the rudder.

The tip vortex flow requires a careful study to understand its effect on the rudder. These vortices are cavity core vortices. Hence, the study of the interaction between these vortices and the rudder will enable us to understand the effect of these vortices on the rudder cavitation. This will also enable us to study the phenomenon of vortex bursting that might occur when these vortices impinge on the rudder. The effect of

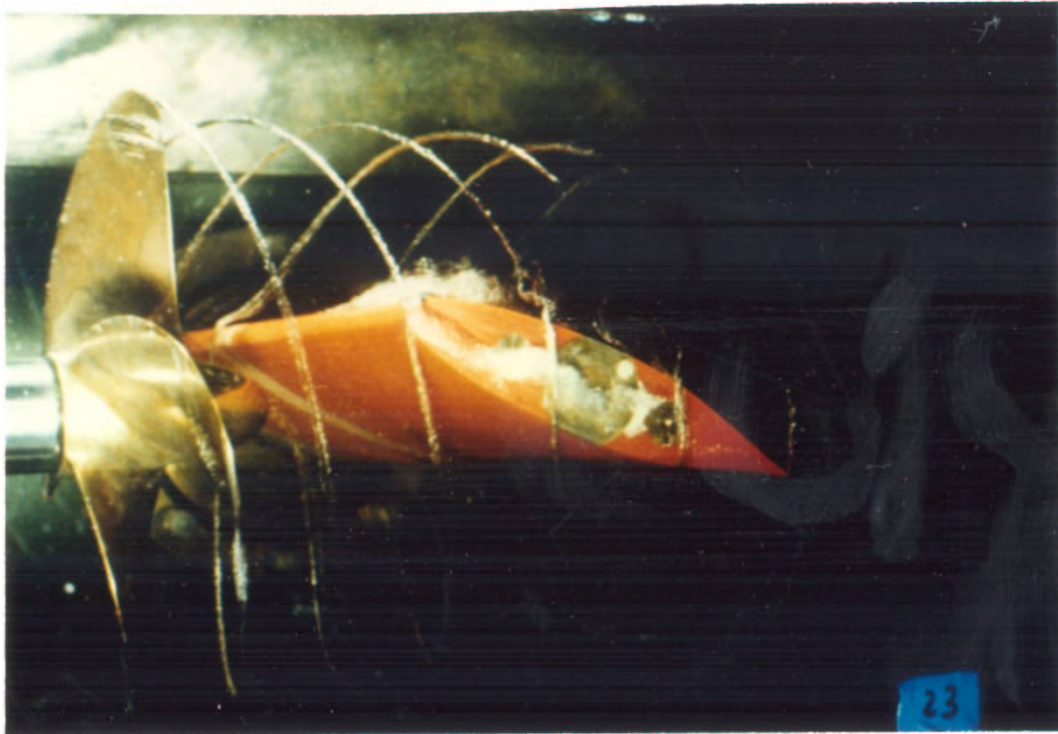


Figure 1.2: The tip vortices impinging on a rudder at an angle of attack as seen in experiment by Kracht [1989a,b].

these vortices and their contribution to the cavitation occurring on the rudders can also be investigated.

Since most propeller rudder interaction studies are based on the effect of the circumferentially averaged propeller flows onto the rudder, a fully unsteady tip vortex/rudder interaction will help us to predict the unsteady effects of these tip vortices on the rudder. This, in future, can lead to the modeling of truly unsteady propeller rudder interaction models.

It is important to understand the physics behind vortex/body interactions in order to understand and evaluate the effect of the propeller blade tip vortices on a rudder of a ship. A clear understanding can also help us to accurately model the interaction

between these tip vortices and the rudder. There are several CFD tools available to model this problem and to evaluate the interactions. A complete CFD model of the ship propeller and its rudder can track the evolution of these tip vortices from the propeller blade and its convection downstream over the rudder. CFD models can help us in evaluating these interactions and assess the effect of these tip vortices on the rudder. However, the size of the domain and the complexity involved in meshing the domain demands large computational requirements. When the problem is solved as an unsteady problem, the requirements further increase, owing to the complexity of involving a time dependent mesh and the solution. Thus, a BEM based model will greatly reduce the complexity of the computational involved, when compared to a CFD model, since only the boundary of the domain needs to be meshed, unlike the meshing of the entire domain in a CFD model.

Thus, a BEM based model for propeller tip vortices/rudder interaction is developed to understand the effect of the tip vortices on the pressure distribution on the surface of the rudder.

1.3 Objectives

The work presented in this thesis focuses on developing a numerical model to study and understand propeller tip vortex/rudder interaction. The aim of developing such a model is to predict the pressure distributions on the rudder surface due to these tip vortices, which in future, can help us to predict the effect of the tip vortices on the rudder cavitation and acoustic noise on the rudder and the hull.

The tip vortex/rudder interaction model consists of

- A line vortex/ interaction model, using a BEM based flow solver to solve for the flow around the hydrofoils, PROPCAV.
- A lifting line model of propeller flows is used to model the lifting line and its tip vortex wake. This model includes the alignment of the tip vortex wake to the total flow field to satisfy the force free condition on the wake.
- The line vortex/hydrofoil interaction model is coupled with the lifting line tip vortex alignment model to finally model the tip vortex/rudder interactions.

1.4 Overview

This section gives an overview of the complete thesis.

Chapter 1 gives an introduction to rudder flows, the actual problem, the motivation to solve the problem, the objectives of this work and the overview of the entire thesis.

Chapter 2 presents a summary of previous work done on vortex/hydrofoil interactions, and on Boundary Element Methods for hydrofoil flow problems on which PROPCAV is based on.

Chapter 3 gives a formal definition of the problem, the solution of the problem, the mathematical formulation of the solution and the numerical implementation of the formulation for line/vortex hydrofoil interactions, lifting line tip vortex wake alignment and the coupling of these two models.

In Chapter 4, the results for vortex/hydrofoil interactions using a commercial CFD solver, FLUENT are presented.

Chapter 5 discusses results of vortex/hydrofoil interactions and the convergence tests and studies performed, using a BEM flow solver, PROPCAV.

Chapter 6 describes the tip vortex alignment process using the lifting line flow representation of the propeller flows.

Chapter 7 gives the results of the effect of the aligned lifting line tip vortex on the rudder.

Chapter 8 summarises the work done, the conclusions, the possible improvements and the future work.

Chapter 2

Literature Review

The tip vortex cavitation of propeller blades has been studied extensively (see Kuiper [2001]), but very few studies exist on the effect of these tip vortices on a rudder. In Kracht [1989a,b], an experiment was performed to study propeller-rudder interactions. Here, the various vortex phenomenon such as the vortex evolution, the curling of the tip vortices around the rudder and the slipstream contraction in terms of the reduction of the radius of the tip vortex can be seen. An attempt has been made in this work to model the phenomenon observed in the experiment done by Kracht [1989a,b] and to predict the pressure distributions on the surface of the rudder due to these tip vortices.

2.1 Vortex Hydrofoil Interactions

Understanding the physics of vortex body interactions will help us to create better and accurate models to predict the behaviour of the vortex around the body and its effect on the body. These interactions give rise to various phenomenon such as production of noise, onset of cavitation, etc thus leading to unsteady loads on the body.

In Rockwell [1998], the underlying physics of the vortex body interactions were discussed with the emphasis on the origin of the induced loading on the bodies due to the vortex. Various cases of vortex body interactions were also discussed. The interaction of a normal vortex with a cylinder was studied in detail by Krishnamoorthy et al. [1999] for the case of a cylinder having a diameter much larger than the normal vortex core diameter. The vortex core deformation was studied including the formation of secondary streamwise vortices along the cylinder. This normal vortex cylinder interaction can be extended to the interaction of a normal vortex with a hydrofoil. Liu and Marshall [2004] performed a computational study of the interaction of a normal vortex with a hydrofoil. These computations were performed by solving full Navier-Stokes equations in primitive-variable form using a finite-volume method, by meshing the entire domain with hexahedral elements. Wood and Grace [2001] employed a low order BEM based model to investigate the unsteady wing response to the presence of a spanwise vortex.

The study of vortex hydrofoil interactions can be extended to study the effect of propeller blade tip vortices on a rudder and the hull. Exhaustive studies exist on a similar phenomenon in the case of the rotor blades tip vortex interaction with the other blades or the fuselage of a helicopter. A tip vortex model for the rotor blades tip vortex was developed by Ramasamy and Leishman [2002] based on the vortex Reynolds number. This model, in combination with a model for vortex filament stretching and rotational flow on the turbulence inside the tip vortices was developed to estimate the temporal growth properties of the helicopter blade tip vortices. Ananthan et al. [2002] investigated the effects of vortex filament strain or stretching on the rotor wake modeling by solving the Navier-Stokes equations represented by a velocity-vorticity formulation. The authors evaluated the evolution of the rotor tip

vortices using a Lamb-Oseen core model for the tip vortex, and explored the strain effects on the rotor tip vortices. Li et al. [2004] investigated the formation of the rotor tip vortex for a two-bladed rotor using lifting line and lifting surface methods, and presented numerical results for the circulations and the contracted wake geometries.

The main difficulty in accounting for the effects of the propeller tip vortices on the rudder is in the modeling of these vortices and tracking its deformation under the influence of the rudder. A RANS model can determine the track of a tip vortex and its interaction with the rudder and the hull. But a full RANS computation can be cumbersome due to the complexity and size of the domain. A BEM model for hydrofoil flows, coupled with an appropriate vortex model (with a cavity core), can solve the rudder-vortex interaction with relative ease and computational efficiency. Most of the theoretical studies on propeller-rudder interaction were carried out based on coupled potential methods, in which the propeller and rudder problems were solved separately, and the interaction taken into account via the circumferentially averaged flow induced by the propeller (Pyo and Suh [2000]; Han et al. [2001]; Achkinadze et al. [2003]; Greco and Salvatore [2004]; Kinnas et al. [2006]). However, the circumferentially averaged flow can not correctly represent the flow field around the rudder, since the flow is fully non-uniform and in an unsteady state.

Hence, this thesis aims to develop a completely unsteady propeller/rudder interaction model by first understanding vortex/hydrofoil interactions. The line vortex/hydrofoil model is developed by modifying a Boundary Element Method based routine, PROPCAV for unsteady flow around a hydrofoil.

2.2 Boundary Element Method

Boundary Element Methods have been found to be very effective in solving potential flow problems around hydrofoils and propellers. Generally, the domain of the problem for flow around propeller or hydrofoil will be complex. Using CFD solvers require the meshing of the entire domain. But, solving the same problem using BEM requires only the boundary of the domain to be meshed, thus making it a viable option to solve for complex flow problems such as flow around a cavitating propeller or a cavitating rudder.

The perturbation potential based panel method was introduced for the analysis of non-cavitating propeller performance in steady flow by Lee [1987] and Kerwin et al. [1987]. Hsin [1990] and Kinnas and Hsin [1992] extended the analysis of non-cavitating propellers in unsteady flow using the hyperboloidal geometry.

A low-order potential based boundary element method was introduced by Kinnas and Fine [1992, 1993] and Fine and Kinnas [1993] for the non-linear analysis of 3-D flow around cavitating hydrofoils or cavitating propellers under the influence of non-axisymmetric inflows. This method was named PROPCAV. Over the years, improvements were made and additional features were introduced in PROPCAV such as prediction of leading edge and mid-chord partial cavitation on the face or back of the blades by Mueller and Kinnas [1999], treatment of mixed partial and super cavity on both sides of the hydrofoil simultaneously by Young and Kinnas [1999, 2001] and treatment of super cavitating propellers with finite thickness trailing edge as well as surface piercing propellers by Young and Kinnas [2001, 2003]. The treatment of a developed tip vortex cavity and a fully unsteady wake alignment procedure were also included in PROPCAV by Lee and Kinnas [2001, 2004].

In the present work, the hydrofoil version of PROPCAV is used to solve the problem of the unsteady flow around a non-cavitating hydrofoil and to predict the pressure distributions on the hydrofoil due to the presence of a line vortex and due to the lifting line tip vortex wake.

Chapter 3

Mathematical Formulation

In this chapter, the first section deals with the mathematical formulation for solving the potential flow around a three dimensional hydrofoil using Boundary Element Methods or panel methods. In the next section, the methodology used to evaluate the effect of a line vortex on a hydrofoil is shown. The third section deals with the technique involved in aligning a helical vortex to the total flow field in order to maintain the force free condition on the aligned vortex. The last section deals with the combination of the helical vortex alignment and the line vortex/hydrofoil interaction to evaluate the effect of a lifting line tip vortex wake on a hydrofoil.

3.1 Boundary Element Method for flow around hydrofoils

3.1.1 Background

There has been a significant amount of evolution in computational methods for engineering design and analysis. They have now become an essential simulation tool for increasing accuracy of the design process. One of the popular tools for numerical computations is the Boundary Element Method, which is based on integral equations.

BEM involves the transformation of the partial differential equations describing the behaviour of variables in the domain under consideration in terms of the integral equations, relating only on boundary values.

The advantages of using BEM are :

1. Only boundaries need to be discretized, thus minimizing storage and computational time used.
2. Problems involving infinite or semi infinite domains can be solved, since the domain at infinity need not be discretized.
3. Problems involving singularity or discontinuity can be effectively dealt with.
4. Boundaries of discontinuities, such as hydrofoil wakes, can be dealt with effectively.

The problem of the potential flow around a hydrofoil can be visualised as shown in Fig. 3.1

3.1.2 Governing Equation

An inviscid irrotational flow is a potential flow. In potential flow, the velocity field \vec{q} can be associated with a scalar function, Φ , such that

$$\vec{q} = \nabla\Phi \quad (3.1)$$

where, the scalar function, Φ , is known as the velocity potential. Since the flow field has to satisfy the continuity equation

$$\nabla\vec{q} = 0 \quad (3.2)$$

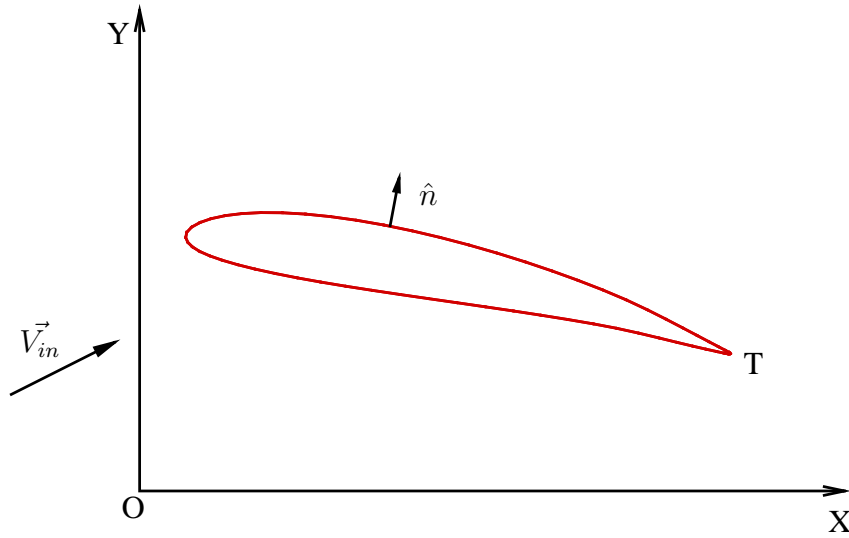


Figure 3.1: Potential Flow around a hydrofoil.

the velocity potential satisfies the Laplace's equation

$$\nabla^2 \Phi = 0 \quad (3.3)$$

which is the governing equation for potential flow problems.

3.1.3 Boundary Conditions

On the surface of the hydrofoil, as shown in Fig. 3.1, since the flow does not penetrate the foil, the velocity normal to the foil should be zero.

$$\vec{q} \cdot \hat{n} = 0 \quad (3.4)$$

This gives the kinematic boundary condition on the foil surface

$$\frac{\partial \Phi}{\partial n} = \hat{n} \cdot \nabla \Phi = 0 \quad (3.5)$$

The condition at infinity

$$\nabla \Phi \sim \vec{V}_{in} \quad (3.6)$$

In addition, the velocity potential also has to satisfy the Kutta condition at the trailing edge of the foil

$$\nabla \Phi = \text{finite} \quad (3.7)$$

The solution to Eqn. 3.3 corresponding to the above boundary conditions can be obtained from the fundamental solution of a point source in an infinite space, also known as Green's functions.

3.1.4 Green's Theorem

Consider a finite volume ν enclosed by a surface S as shown in Fig. 3.2. Suppose G and F are two harmonic functions defined inside ν .

$$\begin{aligned} \nabla^2 F &= 0, \text{ inside } \nu \\ \nabla^2 G &= 0, \text{ inside } \nu \end{aligned} \quad (3.8)$$

Then, Green's theorem says that the following equation holds true for F and G

$$\int \int_S \left[G \frac{\partial F}{\partial n} - F \frac{\partial G}{\partial n} \right] dS = 0 \quad (3.9)$$

where \hat{n} is the unit vector pointing out of the domain ν , normal to the surface S as shown in Fig. 3.2. This is Green's third identity.

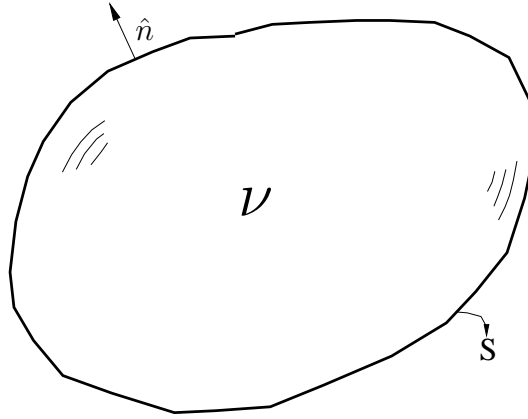


Figure 3.2: Volume ν enclosed by boundary S , adjusted from Kinnas [2006].

3.1.5 Green's formula for a three dimensional body

Consider a body B , enclosed by a surface S_B , in a three dimensional domain, enclosed by a surface S_c as shown in Fig. 3.3. Assume that ϕ is a harmonic function outside B .

$$\nabla^2 \phi = 0, \text{ outside } B \quad (3.10)$$

Also, consider a unit source at a point P outside B . The potential G associated with that unit source is given as

$$G = \frac{-1}{4\pi r} \quad (3.11)$$

where $r = |\vec{r}|$ and $\vec{r} = \vec{r}_F - \vec{r}_P$, with \vec{r}_F and \vec{r}_P being the position vectors corresponding to any field point F outside B and point P respectively, as shown in Fig. 3.3

Consider a sphere of radius R_P at point P enclosed by surface S_P and a surface S_C

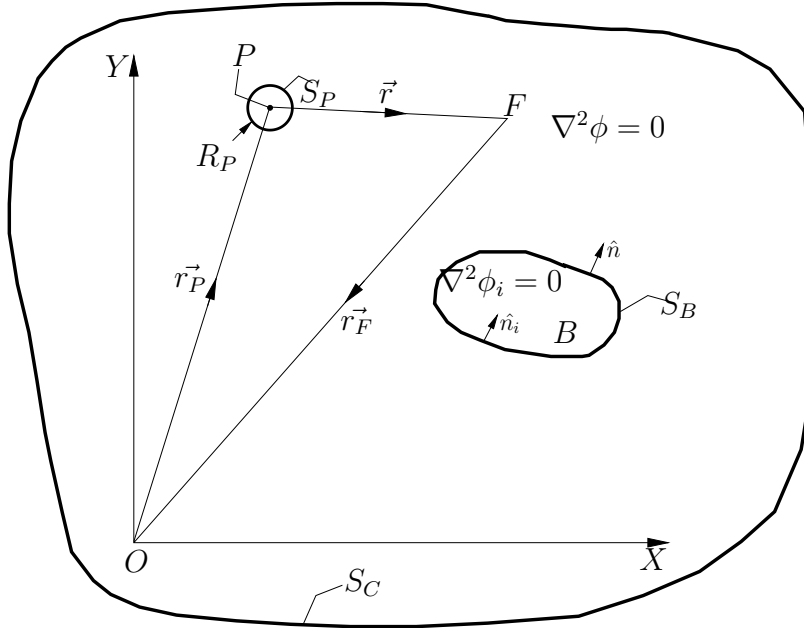


Figure 3.3: Body B and unit source P , adjusted from Kinnas [2006].

surrounding the body and the source. Applying Green's theorem inside the volume surrounded by S_C , S_B and S_P and considering the limits $S_P \rightarrow 0$ and $S_C \rightarrow \infty$, we obtain the following equation

$$4\pi\phi = \int \int_{S_B} \left[\phi \frac{\partial}{\partial n} \frac{1}{R} - \frac{\partial \phi}{\partial n} \frac{1}{R} \right] dS \quad (3.12)$$

The above equation shows that the value of ϕ at any point P outside B depends only on the values of ϕ and $\frac{\partial \phi}{\partial n}$ on the surface S_B of the body B . It can also be seen that the potential at P is a superposition of the potential at P due to sources and dipoles on the body surface S_B . The potential at P is ϕ_P outside B , $\frac{\phi_P}{2}$ on S_B and 0 inside S_B . Similarly, for a harmonic function ϕ_i inside the body, we obtain an integral that is 0 outside the body, $\frac{\phi_{iP}}{2}$ on the body and ϕ_{iP} inside the body. Adding the two integrals together, we obtain an integral equation for ϕ on a 3D body. This integral

equation forms the basis of 3D Boundary Element Methods.

$$2\pi(\phi + \phi_i) = \int_{S_B} \left[(\phi - \phi_i) \frac{\partial}{\partial n} \frac{1}{R} - \left(\frac{\partial \phi}{\partial n} - \frac{\partial \phi_i}{\partial n} \right) \frac{1}{R} \right] dS \quad (3.13)$$

3.1.6 Green's formula for hydrofoil

Consider a hydrofoil as shown in Fig. 3.1, subjected to an inflow $\vec{V}_i n$. Let Φ be the total potential of the flow field and Φ_{in} be the potential associated with the inflow. Then, we define the perturbation potential as

$$\phi = \Phi - \Phi_{in} \quad (3.14)$$

From Eqn. 3.13, taking $\phi_i = 0$ and applying the kinematic boundary condition on the hydrofoil,

$$\begin{aligned} \frac{\partial \phi}{\partial n} &= \frac{\partial \Phi}{\partial n} - \frac{\partial \Phi_{in}}{\partial n} \\ &= -\frac{\partial \Phi_{in}}{\partial n}, \text{ From Eqn. 3.5} \\ &= -\vec{V}_i n \cdot \hat{n} \end{aligned} \quad (3.15)$$

and applying the Kutta condition (Eqn. 3.7) on the trailing edge of the foil and noting the fact that there exists no cross flow across the hydrofoil wake surface, we end up with the integral equation for the perturbation potential on the hydrofoil

$$2\pi\phi = \int \int_{S_B} \left[\phi \frac{\partial}{\partial n} \frac{1}{R} - \frac{\partial \phi}{\partial n} \frac{1}{R} \right] + \int \int_{S_W} \Delta \phi_w \frac{\partial}{\partial n} \frac{1}{R} dS \quad (3.16)$$

Once the perturbation potential ϕ is determined on the hydrofoil surface, the velocity on the hydrofoil is determined as

$$\begin{aligned} \vec{q} &= \nabla \Phi \\ &= \nabla(\Phi_{in} + \phi) \\ &= \vec{V}_i n + \nabla \phi \end{aligned} \quad (3.17)$$

The pressure coefficient is defined as

$$C_P = \frac{P - P_o}{\frac{1}{2}\rho U_{in}^2} \quad (3.18)$$

where, P_o and U_{in} are far field pressure and inflow velocity magnitude or far field velocity magnitude. This can also be written as

$$C_P = 1 - \frac{|\vec{q}|^2}{|\vec{V}_{in}|^2} \quad (3.19)$$

from Bernoulli's equation.

3.1.7 Numerical Implementation

The numerical code, PROCPAV was developed based on the panel methods. This method discretizes the integral equation given in Eqn. 3.16 to obtain the perturbation potential on the hydrofoil. The hydrofoil and the wake surface are discretized using quadrilateral panels, as shown in Fig. 3.4.

Constant strength sources and dipoles are assumed to be distributed on the panel surfaces on the hydrofoil and constant strength dipoles are distributed on the wake surface. Then the above equation is written in a matrix form, where the left hand side matrix contains the unknown dipole strengths of the hydrofoil panels and the right hand side matrix contains the known inflow velocity to the hydrofoil panels. The matrix system can be written as

$$\mathbf{A}\phi = \mathbf{B}\frac{\partial\phi}{\partial\mathbf{n}} \quad (3.20)$$

$\mathbf{A} = [A_{ij}]$ is the matrix of the dipole influence coefficients on the hydrofoil and wake panels. $[A_{ij}]$ is the influence coefficient of the unit dipole on the j^{th} panel

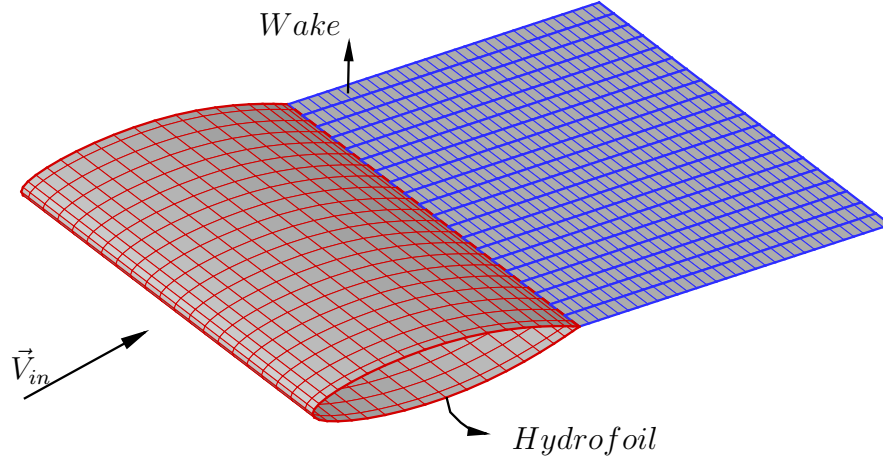


Figure 3.4: Discretized hydrofoil with the wake under an inflow velocity \vec{V}_{in} .

acting on the i^{th} control point. ϕ is the unknown dipole strength which is solved for in Eqn. 3.20. Similarly, $\mathbf{B} = [\mathbf{B}_{ij}]$ is the source influence coefficient matrix of the hydrofoil panels and $\frac{\partial \phi}{\partial \mathbf{n}}$ is the known source strength in terms of the known inflow velocity. The influence coefficients for the sources and dipoles are evaluated using the multipole expansion of the potentials as given by Newman [1985].

The Kutta condition at the trailing edge of the foil, can be enforced numerically by applying the Morino condition [Morino and Kuo [1974]], which requires the potential difference across the trailing edge to be equal to the potential jump across the wake surface. But in PROPCAV, an improved iterative pressure Kutta condition [Kinnas and Hsin [1992]] is applied, where the difference of potentials at the two sides of the trailing edge is modified, in order to achieve equal pressures at both sides of the trailing edge everywhere along the span of the rudder [Young and Kinnas [2001]].

3.2 Line Vortex/hydrofoil interactions using BEM

The boundary integral formulation for a hydrofoil makes it easier to evaluate the effect of a line vortex on a hydrofoil as compared to traditional CFD methods. The discretized form of the boundary integral equation can be transformed into a matrix system, where the left hand side matrix is the unknown and the right hand side matrix is a known quantity. The right hand side matrix is the matrix containing the potential induced by the sources, which is known from the inflow velocity to the hydrofoil.

Since the presence of a vortex in the vicinity of the hydrofoil modifies the inflow field to the hydrofoil, by changing the right hand side matrix to include the influence of the vortex in the source strengths will enable us to evaluate the effect of the vortex on the hydrofoil. The vortex induced velocity at the foil control points are determined and added to the known inflow velocity to solve the vortex/hydrofoil interaction problem. In order to determine the modified inflow field to the hydrofoil, the velocity induced by a line vortex should be determined first.

The velocity induced by a line vortex at any point in space, is derived in detail in Katz and Plotkin [2002]. For completeness, the derivation is summarised and the numerical implementation of the derivation is shown.

3.2.1 The Biot-Savart Law

Consider a vortex segment as shown in Fig. 3.5. This segment has a length dl and a circulation Γ around it. Let \vec{r}_1 and \vec{r}_0 be the position vectors of the vortex segment and the field point P , as shown in Fig. 3.5

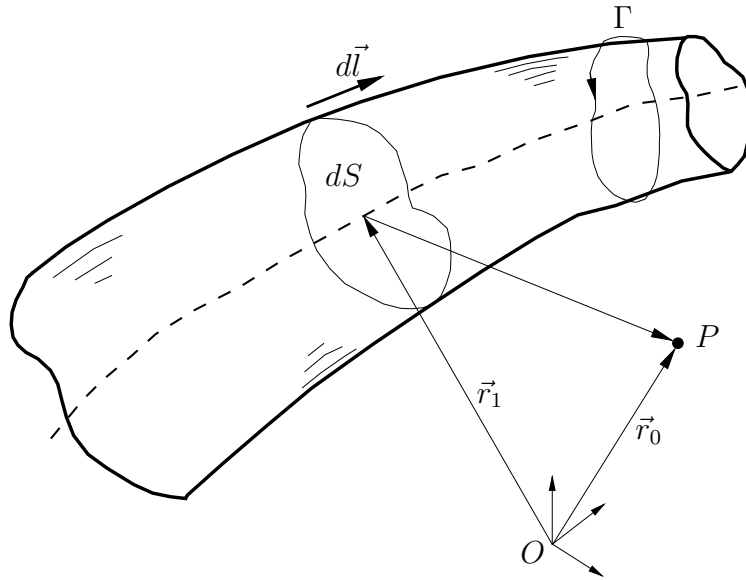


Figure 3.5: Velocity induced at point P by a vortex segment.

Then, Biot-Savart law states that the velocity field induced by the vortex is given as

$$\vec{q} = \frac{\Gamma}{4\pi} \int \frac{d\vec{l} \times (\vec{r}_0 - \vec{r}_1)}{|\vec{r}_0 - \vec{r}_1|^3} \quad (3.21)$$

This can also be written in a differential form as

$$\Delta\vec{q} = \frac{\Gamma}{4\pi} \frac{d\vec{l} \times (\vec{r}_0 - \vec{r}_1)}{|\vec{r}_0 - \vec{r}_1|^3} \quad (3.22)$$

3.2.2 Velocity induced by a line vortex in a 3D space

The velocity induced by a straight vortex segment can be derived based on the Biot-Savart law [Katz and Plotkin [2002]].

Consider a straight vortex segment as shown in Fig. 3.6.

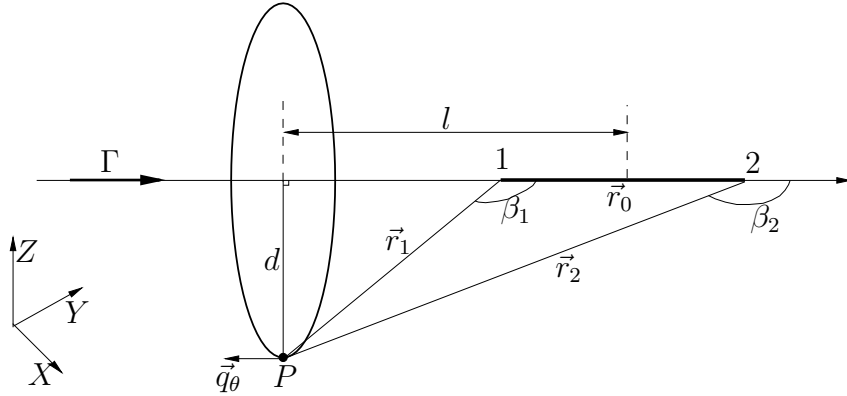


Figure 3.6: Velocity induced at point P by a segment 1-2 of a line vortex.

At point P , the velocity induced by the segment 1 – 2 is q_θ . This induced velocity will have only a tangential component q_θ as shown in Fig. 3.6. From Eqns. 3.21 and 3.22 and after some algebra, it can be shown that the tangential velocity induced is given as

$$\begin{aligned} (q_\theta)_{1,2} &= \frac{\Gamma}{4\pi d} \int_{\beta_1}^{\beta_2} \sin \beta d\beta \\ &= \frac{\Gamma}{4\pi d} (\cos \beta_1 - \cos \beta_2) \end{aligned} \quad (3.23)$$

It can be noted that there exists a singularity as the field point P approaches the line vortex, when the point P is on the line vortex. This can be avoided by assuming that the vortex segment has a core with a small core radius. The self induced velocity of a curved vortex filament with a core was given in Crimi [1965] and was later implemented numerically by Sadler [1971]. The following formulation is a summary of the numerical implementation presented in Sadler [1971].

Consider a curved vortex filament consisting of two curved vortex segments with core radius a_{i-1} and a_i , as shown in Fig. 3.7. Let these two vortex segments have

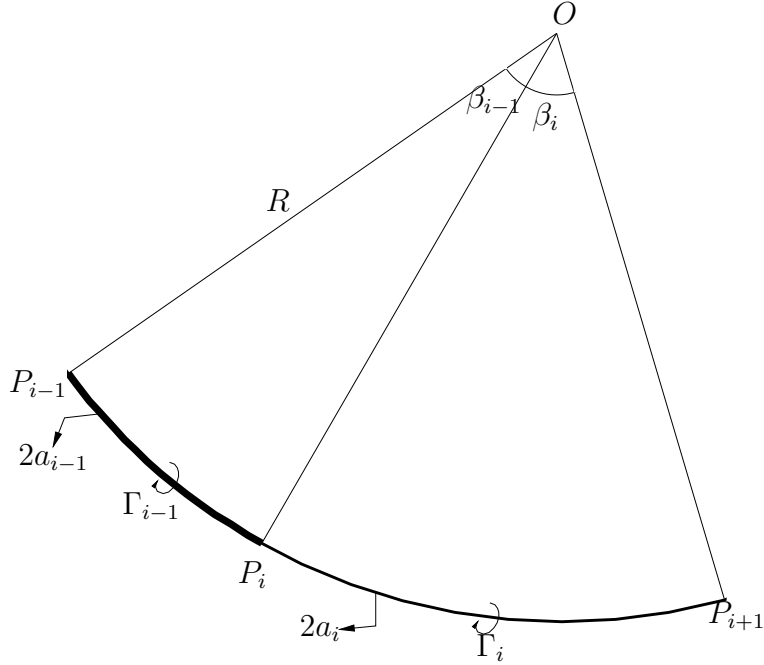


Figure 3.7: Vortex self-induced velocity model.

vertices P_{i-1}, P_i and P_i, P_{i+1} , and let the circulation around each segment be Γ_{i-1} and Γ_i . Let R be the radius of curvature of the segment P_{i-1}, P_{i+1} and O be the center. Let the two segments subtend an angle β_{i-1} and β_i at O respectively. Then the self-induced velocity of the segment P_{i-1}, P_{i+1} at P_i is given as

$$q_{self} = \frac{1}{8\pi R} \left(\Gamma_{i-1} \left[\log \left(\frac{8R}{a_{i-1}} \tan \frac{\beta_{i-1}}{4} \right) + \frac{1}{4} \right] + \Gamma_i \left[\log \left(\frac{8R}{a_i} \tan \frac{\beta_i}{4} \right) + \frac{1}{4} \right] \right) \quad (3.24)$$

If the point P_i lies on the extremity of the vortex segment, then Eqn. 3.24 can still be used to evaluate the self induced velocity at that point. Suppose that the vortex segment has vertices P_i, P_{i+2} and vortex segments P_i, P_{i+1} and P_{i+1}, P_{i+2} . Then the three vertices are used to evaluate the radius of curvature of the segment P_i, P_{i+2} and the corresponding subtended angles. Then Eqn. 3.24 is used to evaluate the

self induced velocity at P_i by using just the one term corresponding to the vortex segment P_i, P_{i+1} . Then the self induced velocity will be

$$q_{self} = \frac{1}{8\pi R} \left(\Gamma_i \left[\log \left(\frac{8R}{a_i} \tan \frac{\beta_i}{4} \right) + \frac{1}{4} \right] \right) \quad (3.25)$$

3.2.3 Numerical Implementation

For ease of numerical computation, Eqn. 3.23 can be modified to obtain the induced velocity in the three dimensional space. Let \vec{r}_1 and \vec{r}_2 be the vectors from the field point P to the vertices of the vortex segments 1 and 2 respectively as shown in Fig. 3.6. Let \vec{r}_0 be the vector connecting the vertices 1 and 2. Then, it can be seen that

$$\begin{aligned} d &= \frac{|\vec{r}_1 \times \vec{r}_2|}{|\vec{r}_0|} \\ \cos \beta_1 &= \frac{\vec{r}_0 \cdot \vec{r}_1}{|\vec{r}_0| |\vec{r}_1|} \\ \cos \beta_2 &= \frac{\vec{r}_0 \cdot \vec{r}_2}{|\vec{r}_0| |\vec{r}_2|} \end{aligned} \quad (3.26)$$

and the velocity $\vec{q}_{1,2}$ is normal to the plane created by the point P and the vertices 1 and 2, and is given by

$$\frac{\vec{r}_1 \times \vec{r}_2}{|\vec{r}_1 \times \vec{r}_2|}$$

Thus the induced velocity is given as

$$\vec{q}_{1,2} = \frac{\Gamma}{4\pi} \frac{\vec{r}_1 \times \vec{r}_2}{|\vec{r}_1 \times \vec{r}_2|^2} \vec{r}_0 \cdot \left(\frac{\vec{r}_1}{|\vec{r}_1|} - \frac{\vec{r}_2}{|\vec{r}_2|} \right) \quad (3.27)$$

The self induced velocity is determined using the following equations. Let $P_{i-1} = (x_{i-1}, y_{i-1}, z_{i-1})$, $P_i = (x_i, y_i, z_i)$ and $P_{i+1} = (x_{i+1}, y_{i+1}, z_{i+1})$ be the vertices on the curved vortex filament and we need to determine the self induced velocity of the curved vortex at P_i . Let the vortex segment P_{i-1}, P_{i+1} have a constant circulation

Γ around it and a constant core radius of a_i . Then the self induced velocity at P_i , $\vec{q}_i = (u_i, v_i, w_i)$ is given as

$$\begin{aligned} u_i &= n_x F \\ v_i &= n_y F \\ w_i &= n_z F \end{aligned} \tag{3.28}$$

where

$$\begin{aligned} n_x &= (y_{i-1} - y_i)(z_i - z_{i+1}) - (z_{i-1} - z_i)(y_i - y_{i+1}) \\ n_y &= (z_{i-1} - z_i)(x_i - x_{i+1}) - (x_{i-1} - x_i)(z_i - z_{i+1}) \\ n_z &= (x_{i-1} - x_i)(y_i - y_{i+1}) - (y_{i-1} - y_i)(x_i - x_{i+1}) \\ F &= [\Gamma(\log e_1 + 1/4) + \Gamma(\log e_2 + 1/4)] / b \\ b &= 8\pi R [n_x^2 + n_y^2 + n_z^2]^{1/2} \\ e_1 &= \frac{8Rf}{a_i} \\ e_2 &= \frac{8Rg}{a_i} \end{aligned} \tag{3.29}$$

The radius of curvature R is given as

$$\begin{aligned} R &= \frac{L_{i-1}L_i\delta_i}{[4L_{i-1}^2L_i^2 - (L_{i-1}^2 + L_i^2 - \delta_i^2)]^{2/3}} \\ L_i &= [(x_{i+1} - x_i)^2 + (y_{i+1} - y_i)^2 + (z_{i+1} - z_i)^2]^{1/2} \\ \delta_i &= [(x_{i+1} - x_{i-1})^2 + (y_{i+1} - y_{i-1})^2 + (z_{i+1} - z_{i-1})^2]^{1/2} \\ f &= \begin{cases} (2R - \sqrt{4R^2 - L_{i-1}^2}) / L_{i-1}, & \text{for } L_{i-1}^2 \leq \delta_i^2 + L_i^2 \\ (2R + \sqrt{4R^2 + L_{i-1}^2}) / L_{i-1}, & \text{for } L_{i-1}^2 \geq \delta_i^2 + L_i^2 \end{cases} \\ g &= \begin{cases} (2R - \sqrt{4R^2 - L_i^2}) / L_i, & \text{for } L_i^2 \leq \delta_i^2 + L_{i-1}^2 \\ (2R + \sqrt{4R^2 + L_i^2}) / L_i, & \text{for } L_i^2 \geq \delta_i^2 + L_{i-1}^2 \end{cases} \end{aligned} \tag{3.30}$$

Now, the induced velocity at any point in space, P due to a line vortex can be determined.

3.2.4 BEM formulation for line vortex/hydrofoil interaction

Let the velocity induced by a line vortex at the hydrofoil panel control points be \vec{U}_{vort} and as mentioned earlier, let the inflow velocity to the hydrofoil be \vec{U}_{in} . Then the 3D BEM formula for the hydrofoil can be modified from Eqn. 3.16 as shown

$$2\pi\phi = \int \int_{S_B} \left[\phi \frac{\partial}{\partial n} \frac{1}{R} - \left[(-\vec{V}_{in} + \vec{V}_{wk}) \cdot \vec{n} \right] \frac{1}{R} \right] + \int \int_{S_W} \Delta\phi_W \frac{\partial}{\partial n} \frac{1}{R} dS \quad (3.31)$$

Once, the perturbation potential is determined on the foil surface panels, the perturbation velocity on the foil surface is determined as

$$2\pi\nabla\phi = \int \int_{S_B} \left[\phi \nabla \frac{\partial}{\partial n} \frac{1}{R} - \frac{\partial\phi}{\partial n} \nabla \frac{1}{R} \right] + \int \int_{S_W} (\Delta\phi_W) \nabla \frac{\partial}{\partial n} \frac{1}{R} dS \quad (3.32)$$

After the perturbation velocity $\vec{q}_{pert} = \nabla\phi$ on the foil surface is determined, the total velocity on the foil surface is determined as

$$\vec{q} = \vec{q}_{pert} + \vec{V}_{in} \quad (3.33)$$

Then the pressure coefficient on the foil surface is determined as

$$C_P = 1 - \frac{|\vec{q}|^2}{|\vec{V}_{in}|^2} \quad (3.34)$$

Once the problem for the hydrofoil under the influence of a line vortex is solved, the total velocity at the line vortex is evaluated. This includes the inflow velocity and the velocity induced by the hydrofoil and its wake, \vec{V}_{rud} .

$$\vec{V}_{tot} = \vec{V}_{in} + \vec{V}_{rud} \quad (3.35)$$

Then the vortex locations are convected in time ΔT to get the new vortex locations as

$$\vec{X}_{new} = \vec{X}_{old} + \vec{V}_{tot}\Delta T \quad (3.36)$$

3.3 Propeller flows as lifting line flows

The lifting line method approximates the propeller blade and its trailing wake to line vortices with a circulation around them. The propeller blade can be considered as a lifting surface with some distribution of bound and free vortex sheet strength. In the limiting case of vanishing chord length of the lifting surface, the propeller blade reduces to a concentrated radial vortex line with circulation $\Gamma(r)$, for each blade. Thus we can approximate the whole system of a rotating propeller to a set of concentrated radial vortex lines with circulation $\Gamma(r)$, rotating with angular velocity ω about a common axis (which is taken as the x-axis in this case). Ideally, the lifting lines start at a hub radius r_h and extend to the maximum propeller radius R . The lifting line system with the lifting line and its wake is show in Fig. 3.8.

Thus, there are Z lifting lines, symmetrically placed about the axis of rotation, representing the individual blades of a Z bladed propeller. We can assume that the lifting line experiences an inflow, $\vec{V}_{in}(r) = (V_a(r), V_t(r))$, where $V_a(r)$ is the axial inflow and $V_t(r)$ is the tangential inflow. Though a radial inflow component, $V_r(r)$, exists, the approximation of a propeller to a lifting line system makes it difficult to capture this effect on the lifting line. Also let us assume that the lifting line has a circulation distribution $\Gamma(r)$ on it. An important part of solving the problem for a lifting line is determining the strength and the position of the free vorticity, $\gamma_f(r)$. The strength

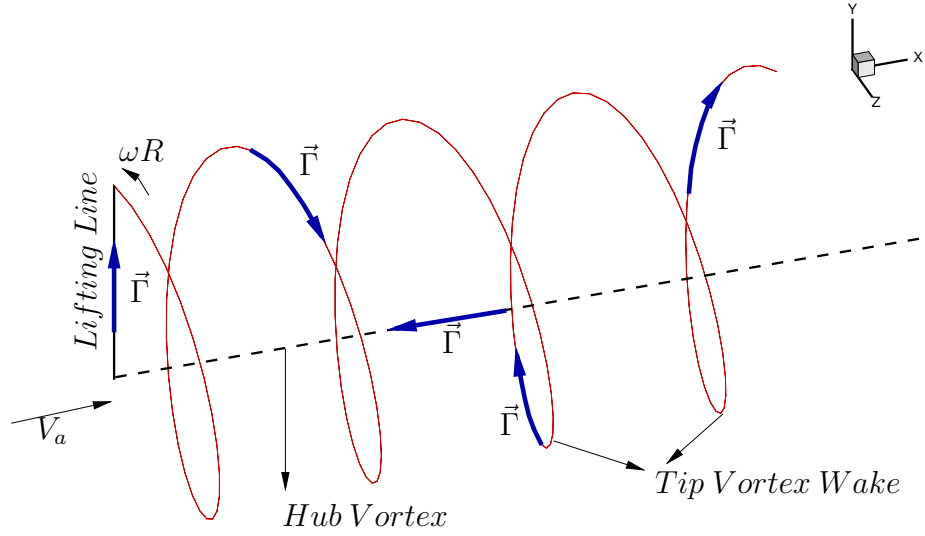


Figure 3.8: Lifting Line with the tip vortex wake.

can be determined from Kelvin's theorem as

$$\gamma_f(r) = -\frac{\partial \Gamma(r)}{\partial r} \quad (3.37)$$

The free vortex filament of the wake is assumed to follow the streamlines of the undisturbed flow so that each free vortex filament follows a helical path of the pitch given as follows:

$$P(r) = 2\pi r \tan \beta(r) \quad (3.38)$$

where $\beta(r)$ is the pitch angle at radius r

$$\beta(r) = \tan^{-1} \frac{V_a(r)}{\omega r + V_t(r)} \quad (3.39)$$

where ω is the rotational velocity of the lifting line. The presence of the wake of the lifting line alters the flow field in the vicinity of the lifting line and its wake. Let this total flow field be denoted as \vec{V}_{tot} . This flow field consists of the inflow to the lifting line system and the velocity induced by the lifting line and its wake,

$\vec{V}_{wk} = (u_{wk}, v_{wk}, w_{wk})$. Thus, the total flow field is given as:

$$\vec{V}_{tot} = \vec{V}_{in} + \vec{V}_{wk} \quad (3.40)$$

Hence, for any calculations involving the lifting line and its wake, it is important to align the free vortex wake with the total flow.

$$\vec{\Gamma} \times \vec{V}_{tot} = 0 \quad (3.41)$$

3.4 Lifting line wake alignment

To solve the problem of a lifting line, it is important to align the free vortex wake with the flow, so that the force free condition on the free vortex wake is satisfied as shown in Eqn. 3.41. A simple technique of the lifting line wake alignment is employed for satisfying the force free condition. This problem is solved for a single lifting line system with zero hub radius. The lifting line and the wake systems are shown in Fig. 3.8. The lifting line is assumed to have constant circulation along the radial distance. The tip vortex is shed from the tip of the lifting line as shown in Fig. 3.8. In order to simplify the problem, the wake is considered to have two components. The initial part or the transition wake that will be aligned with the flow. The pitch of this wake might not be constant, depending on the velocity \vec{V}_{tot} and could vary with the flow at the wake locations. The second part or the ultimate wake is assumed to be of a constant pitch and is assumed to extend for a longer length. The circulation is closed by a similar lifting line at the end of this wake, but with a circulation opposite to that of the actual lifting line. Then both the lifting lines are joined to complete the circulation. The lifting line, the wake and the closing vortex components are all assumed to have the same circulation.

Let the coordinates of the transition wake to be aligned be $\vec{X} = (x, y, z)$ Initially, the lifting line is assumed to be under the influence of a constant axial inflow, V_a and a constant tangential inflow, ωR . Thus the initial shed vortex from the tip of the lifting line is a helix with a constant pitch given as

$$P = 2\pi R \tan \beta \quad (3.42)$$

and a constant pitch angle

$$\tan \beta = \frac{V_a}{R\omega} \quad (3.43)$$

Assume an angular coordinate θ , to define the helical wake. Thus the initial constant pitch helical wake coordinates are given as:

$$\begin{aligned} x &= R\theta \tan \beta \\ y &= R \cos(\theta + \delta_k) \\ z &= R \sin(\theta + \delta_k) \end{aligned} \quad (3.44)$$

δ_k is the angle of the lifting line for which the wake is being evaluated.

The transition and the ultimate wake are discretized into elements by the discretized angular coordinate $\Delta\theta$. Let us denote the i^{th} point of the helical wake at the t^{th} iteration step by the coordinates $\vec{X}_i^t = (x_i^t, y_i^t, z_i^t)$. Then, the i^{th} vortex element of the helical wake has the vertices \vec{X}_i^t and \vec{X}_{i+1}^t , i.e, (x_i^t, y_i^t, z_i^t) and $(x_{i+1}^t, y_{i+1}^t, z_{i+1}^t)$. The the initial coordinates of the discretized constant pitch helical wake is given as

$$\begin{aligned} x_i^t &= R(i-1)\Delta\theta \tan \beta \\ y_i^t &= R \cos [(i-1)\Delta\theta + \delta_k] \\ z_i^t &= R \sin [(i-1)\Delta\theta + \delta_k] \end{aligned} \quad (3.45)$$

If we denote the time step in which each vortex segment is shed from the lifting line tip to form the constant pitch helical wake by Δt , then this time step can be written as

$$\Delta t = \frac{\Delta\theta}{\omega} \quad (3.46)$$

Then the initial coordinates of the transition wake are given as

$$\begin{aligned} x_i^0 &= x_{i-1}^0 + V_a \Delta t \\ y_i^0 &= R \cos [(i-1)\Delta\theta] = y_{i-1}^0 - \omega z_{i-1}^0 \Delta t \\ z_i^0 &= R \sin [(i-1)\Delta\theta] = z_{i-1}^0 + \omega y_{i-1}^0 \Delta t \end{aligned} \quad (3.47)$$

The ultimate wake is also created in a similar way.

Once the helical wake with the constant pitch angle is created, the alignment process is done as follows. The wake vortex elements are assumed to be straight line segments of constant circulation. Using Eqn. 3.27, the induced velocity \vec{V}_{wk} at each wake element vertex is determined. This induced velocity is composed of the velocity induced by the lifting line, the transition wake, the ultimate wake and the vortex segments, including the self induced velocity of the vortex segments completing the circulation. This induced velocity is added to the inflow velocity, \vec{V}_{in} , to get the total velocity field at the wake element vertices, $\vec{V}_{tot} = (u_{tot}, v_{tot}, w_{tot})$. Once the total velocity is determined, the new location of the wake is determined by convecting each i^{th} point of the wake at iteration step t with the velocity of the $(i-1)^{th}$ point at iteration step $t-1$ in time Δt . This can be done because the tip of the lifting line is fixed, and at all times the wake is shed from this point only. This process can be shown in Fig. 3.9. Thus the wake coordinates at iteration step t are given as

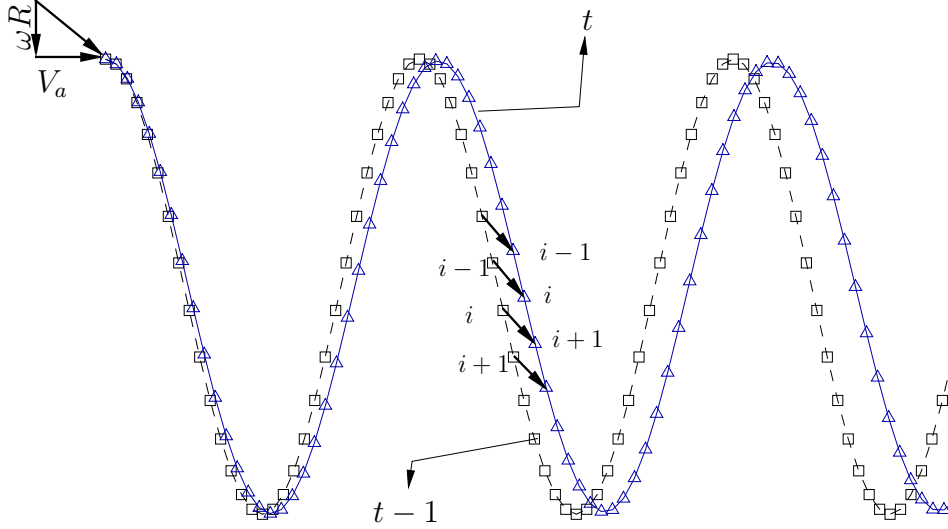


Figure 3.9: Lifting line tip vortex wake alignment process.

$$\begin{aligned}
 x_i^t &= x_{i-1}^{t-1} + (u_{i-1}^{t-1})_{tot} \Delta t \\
 y_i^t &= y_{i-1}^{t-1} + (v_{i-1}^{t-1})_{tot} \Delta t \\
 z_i^t &= z_{i-1}^{t-1} + (w_{i-1}^{t-1})_{tot} \Delta t
 \end{aligned} \tag{3.48}$$

However, this scheme could not converge to the aligned wake solution. Rather than demonstrating the expected slip stream contraction, this scheme resulted in a wake that expanded with the iteration steps.

This scheme requires a very small time step size, Δt , and hence a very small angular coordinate, $\Delta \theta$. This increases the computational time as the number of wake elements increases, thus requiring the vortex induced velocity to be evaluated for more number of elements. A higher order time stepping scheme can be used to increase accuracy. But this would again increase the computational time because the vortex

induced velocities are to be evaluated at each of the fractional time step, depending on the order of the time stepping scheme. This can be avoided by convecting the wake points as follows. Equation 3.48 displays that the wake points are convected along a vector in the direction of the total velocity, \vec{V}_{tot} . Thus, the discretization causes the wake points to follow a straight path rather than the actual curved path of the slip stream. This is avoided by the scheme given below. In this scheme, the wake points are first convected along the slipstream of the wake and then moved with the induced velocities in time Δt to get the new wake locations.

Thus, the coordinates of the new wake position which is aligned with the total flow is given as

$$\begin{aligned}
x_i^t &= x_{i-1}^{t-1} + (u_{i-1}^{t-1})_{tot} \Delta t \\
y_i^t &= y_{i-1}^{t-1} \cos \Delta\theta - z_{i-1}^{t-1} \sin \Delta\theta + (v_{i-1}^{t-1})_{wk} \Delta t \\
z_i^t &= z_{i-1}^{t-1} \cos \Delta\theta + y_{i-1}^{t-1} \sin \Delta\theta + (w_{i-1}^{t-1})_{wk} \Delta t
\end{aligned} \tag{3.49}$$

It can also be proved that Eqn. 3.48 is an approximation to Eqn. 3.49. for the limiting case of $\Delta\theta \rightarrow 0$. The proof is given below.

At iteration step $(t - 1)$, let the radius of the $(i - 1)^{th}$ point be R_{i-1} and the angular coordinate be θ_{i-1} . Then,

$$\begin{aligned}
y_{i-1}^{t-1} &= R_{i-1}^{t-1} \cos \theta_{i-1} \\
z_{i-1}^{t-1} &= R_{i-1}^{t-1} \sin \theta_{i-1}
\end{aligned} \tag{3.50}$$

From Eqn. 3.49, the y and the z coordinates at iteration step t for the i^{th} wake element are obtained by first convecting the point about a cylinder with radius R_{i-1}^{t-1}

and then convecting it with the wake induced velocities, $(\vec{V}_{i-1}^{t-1})_{wk}$. Thus,

$$\begin{aligned} y_i^t &= R_{i-1}^{t-1} \cos \theta_{i-1} + \Delta\theta + (v_{i-1}^{t-1})_{wk} \Delta t \\ z_i^t &= R_{i-1}^{t-1} \sin \theta_{i-1} + \Delta\theta + (w_{i-1}^{t-1})_{wk} \Delta t \end{aligned} \quad (3.51)$$

Using standard *sine* and *cosine* expansions, we get

$$\begin{aligned} y_i^t &= R_{i-1}^{t-1} \cos \theta_{i-1} \cos \Delta\theta - R_{i-1}^{t-1} \sin \theta_{i-1} \sin \Delta\theta + (v_{i-1}^{t-1})_{wk} \Delta t \\ z_i^t &= R_{i-1}^{t-1} \sin \theta_{i-1} \cos \Delta\theta + R_{i-1}^{t-1} \cos \theta_{i-1} \sin \Delta\theta + (w_{i-1}^{t-1})_{wk} \Delta t \end{aligned} \quad (3.52)$$

From Eqns. 3.50 and 3.52, we obtain the coordinates of the wake at the next iteration step, which are similar to Eqn. 3.49

$$\begin{aligned} y_i^t &= y_{i-1}^{t-1} \cos \Delta\theta - z_{i-1}^{t-1} \sin \Delta\theta + (v_{i-1}^{t-1})_{wk} \Delta t \\ z_i^t &= z_{i-1}^{t-1} \cos \Delta\theta + y_{i-1}^{t-1} \sin \Delta\theta + (w_{i-1}^{t-1})_{wk} \Delta t \end{aligned} \quad (3.53)$$

In the limit, $\Delta\theta \rightarrow 0$, $\cos \Delta\theta \rightarrow 1$ and $\sin \Delta\theta \rightarrow \Delta\theta = \omega \Delta t$. Thus Eqn. 3.52 can be written as

$$\begin{aligned} y_i^t &= y_{i-1}^{t-1} - z_{i-1}^{t-1} \omega \Delta t + (v_{i-1}^{t-1})_{wk} \Delta t \\ &= y_{i-1}^{t-1} + (v_{i-1}^{t-1})_{tot} \Delta t \\ z_i^t &= z_{i-1}^{t-1} + y_{i-1}^{t-1} \omega \Delta t + (w_{i-1}^{t-1})_{wk} \Delta t \\ &= z_{i-1}^{t-1} + (w_{i-1}^{t-1})_{tot} \Delta t \end{aligned} \quad (3.54)$$

where, the velocities $(v_i^t)_{tot}$ and $(w_i^t)_{tot}$ are obtained using a transformation of the inflow tangential velocity in the $y - z$ plane and its addition to the velocity induced by the wake in the $y - z$ plane. The direction of the velocities in the $y - z$ plane is shown in Fig. 3.10 The total velocities in the $y - z$ plane can also be obtained as

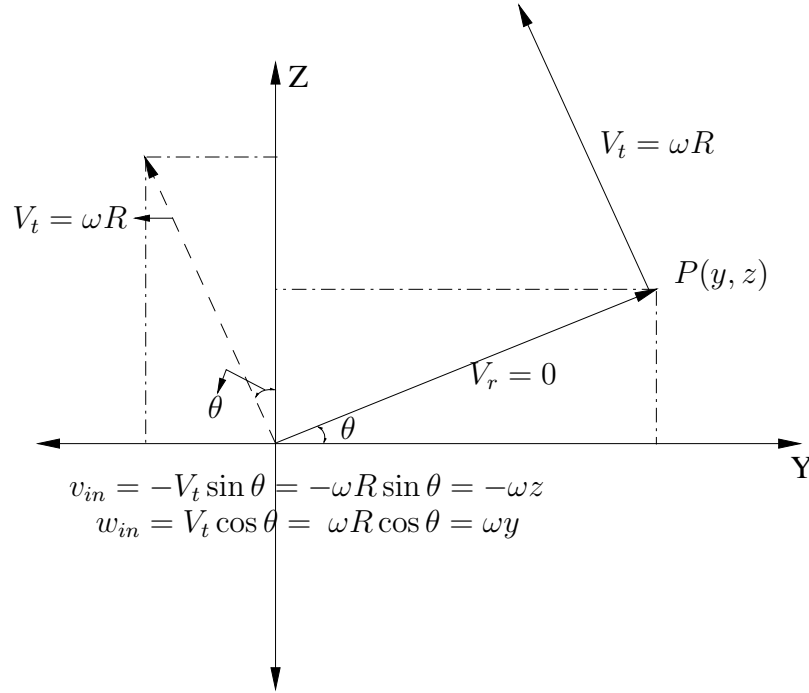


Figure 3.10: Angular velocity transformation in $y - z$ plane.

$$\begin{aligned}
 (v_i^t)_{tot} &= (v_i^t)_{wk} - \omega z_i^t \\
 (w_i^t)_{tot} &= (w_i^t)_{wk} + \omega y_i^t
 \end{aligned}
 \tag{3.55}$$

Thus we end up with Eqn. 3.48. Comparing Eqn. 3.54 with Eqn. 3.48, the additional term is the vortex induced velocity which causes the wake to change its position. Thus we can get the coordinates of the updated wake position. Thus, this scheme includes the effect of discretization, which would otherwise have been lost in the scheme given by Eqn. 3.48, and hence, requiring more computational complexity. This process is continued till the L^2 norm of the error $|\vec{\Delta r}|$ between \vec{X}_i^t and \vec{X}_i^{t-1} reaches a specified value.

The following parameters are determined at each vertex of the wake element. The

error at iteration step t , compared to the wake location at iteration step $t - 1$ is computed as

$$|\Delta \vec{X}_{err}|_i^t = |\vec{X}_i^t - \vec{X}_i^{t-1}| \quad (3.56)$$

The angle between the velocity vector $(\vec{V}_i^t)_{tot}$ and the direction vector of the wake at that point $\Delta \vec{r}_i^t$ is determined as

$$\alpha_i^t = \sin^{-1} \frac{|\vec{V}_i^t \times \Delta \vec{r}_i^t|}{|\vec{V}_i^t| |\Delta \vec{r}_i^t|} \quad (3.57)$$

The L^2 norm of the error $|\Delta \vec{X}_{err}|_i^t$ is determined as

$$L^2(|\Delta \vec{X}_{err}|^t) = \sqrt{\sum_i (|\Delta \vec{X}_{err}|_i^t)^2} \quad (3.58)$$

In order to obtain the converged wake geometry, a convergence criteria is imposed on the L^2 norm of the error (Eqn. 3.58). Once the convergence criteria is satisfied, the angle α_i at each tip vortex segment tends to 0, thus satisfying the force free wake condition (Eqn. 3.41). Thus, the aligned tip vortex geometry of the lifting line is obtained.

3.5 Lifting line tip vortex/hydrofoil interactions

The 3D BEM formulation for the line vortex/hydrofoil interaction is coupled with the wake alignment procedure to evaluate the effect of the lifting line tip vortex wake on the rudder. The lifting line system with the rudder is shown in Fig. 3.11.

The Lifting line tip vortex wake/rudder problem is coupled and solved as following:

1. Initially, the tip vortex wake is assumed to be a helical wake with a constant pitch. The coordinates of the tip vortex wake, \vec{X}_i^0 are created. The inflow ve-

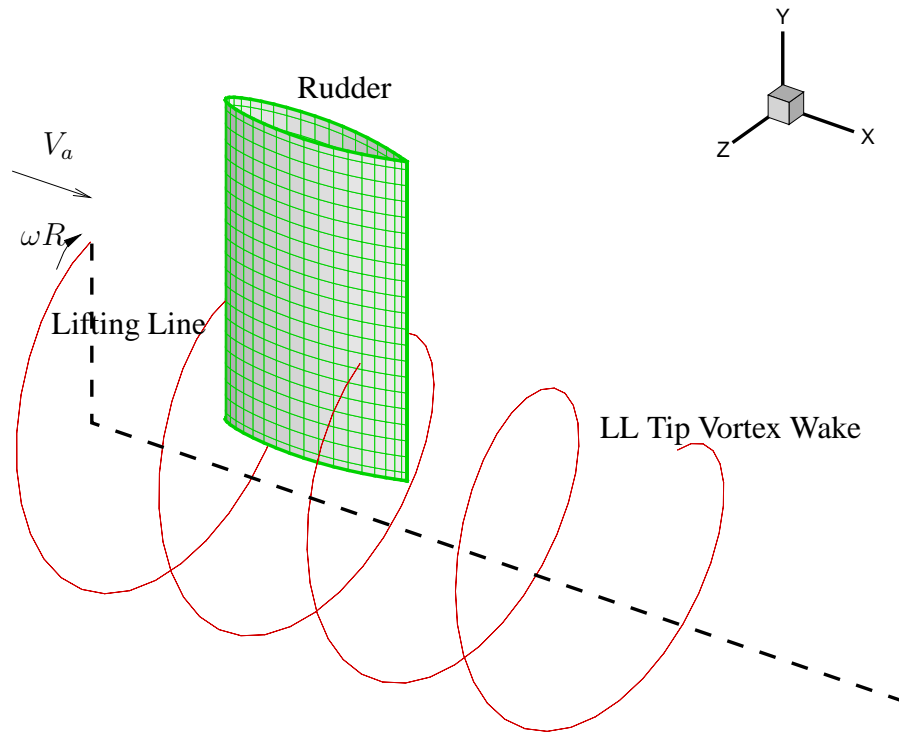


Figure 3.11: Lifting line tip vortex/rudder system.

locity to Lifting line and the rudder is assumed to be a constant axial velocity, V_a and the Lifting line rotates with a constant angular velocity ω .

2. The hydrofoil surface is discretized into panels and the velocity induced by the wake on the panel control points, \vec{V}_{wk} is obtained.
3. The problem of the hydrofoil under an inflow $\vec{V}_{in} + \vec{V}_{wk}$ is solved using 3D BEM formulation as shown in Eqn. 3.31
4. Then the velocity induced by the hydrofoil and its wake, \vec{V}_{rud} at the tip vortex wake vertices \vec{X}_i is determined.

5. The tip vortex wake is aligned to its new vertices $\vec{X}_i^{t+1} = (x_i^{t+1}, y_i^{t+1}, z_i^{t+1})$ using the total velocity $(\vec{V}_{tot})_i^t$ at the vertices $\vec{X}_i^t = (x_i^t, y_i^t, z_i^t)$, where,

$$(\vec{V}_{tot})_i^t = (\vec{V}_{in} + \vec{V}_{wk} + \vec{V}_{rud})_i^t \quad (3.59)$$

using Eqn. 3.49.

6. The error $|\Delta \vec{X}_{err}|_i^{t+1}$ and its L^2 norm is determined. If the L^2 norm of the error satisfies the set convergence criteria, then the aligned wake is obtained, the problem for the hydrofoil is solved, the pressure distribution on the hydrofoil is determined and the complete solution is obtained. If the convergence criterion is not satisfied, then the processes from step 2 is repeated.
7. Once the solution at a particular lifting line angle is obtained, the lifting line is rotated by δ_k to its new position and the above steps repeated. However, the initial geometry of the tip vortex wake \vec{X}_i^0 is obtained by rotating the aligned tip vortex geometry from the previous lifting line location by δ_k . This speeds up the convergence process and the tip vortex wake is aligned faster.

Chapter 4

Vortex/Hydrofoil Interactions Using FLUENT

The most important aspect of understanding and solving propeller tip vortex rudder interactions is to understand and track the evolution of this tip vortex through space and time. CFD tools can help us to model the interaction between the tip vortex and rudder and can also help us track the evolution of the tip vortex. But the complexity and the size of the domain makes the CFD modeling quite complex and difficult. The size of the domain requires a large grid to completely capture the fluid dynamics taking place in the domain. Also, the size of the tip vortex compared to the rudder span or chord is extremely small. This requires a dense grid in order to fully capture the flow dynamics of the vortex.

In this section, a commercial CFD tool, FLUENT, is used to model and understand the vortex dynamics. The first section deals with the 2D modeling of a Rankine vortex in a uniform flow, and the various issues involved in the modeling process. In the next section, the 2D vortex model is extended to a 3D space in the presence of a foil, and the pressure distributions on the foil as the vortex passes over the foil are obtained.

4.1 2D Vortex in uniform flow

A study of the dynamics of a two dimensional vortex in a uniform flow will give an insight into the modeling nuances of a three dimensional vortex in the presence of a hydrofoil. The ease of modeling a 2D vortex makes it a viable problem to study the various modeling issues, such as the grid size, time step size, the viscous model to be used and the correct order of the solution to be used. A Rankine vortex has the following tangential velocity distribution:

$$V_t = \begin{cases} \frac{\Gamma}{2\pi r} & \text{for } r \geq r_0 \\ \frac{\Gamma}{2\pi r_0^2} r & \text{for } r \leq r_0 \end{cases}$$

where r_0 is the radius of the vortex core and r is the radial distance from the center of the vortex core to the field point. The tangential velocity distribution is as shown in Fig. 4.1.

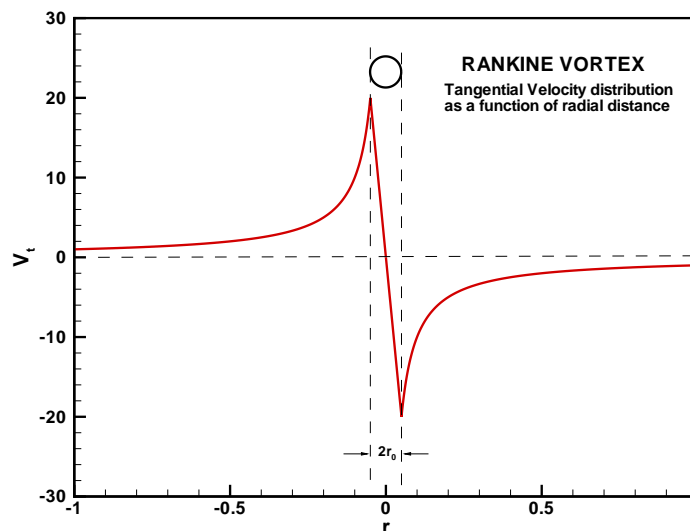


Figure 4.1: Tangential velocity distribution for a Rankine vortex.

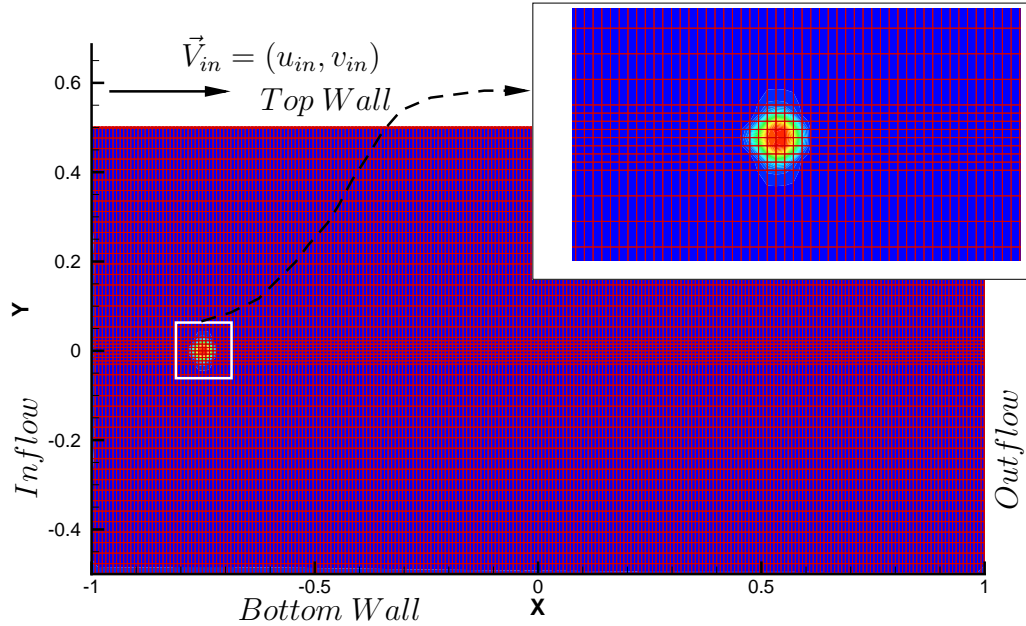


Figure 4.2: The domain and the grid for a 2D vortex in uniform flow for 5 grid points across the vortex core.

The domain of the problem is a simple rectangular domain with quadrilateral cells as shown in Fig. 4.2. The grid size is decided based on the number of grid points available within the vortex core, to effectively capture the vorticity of the initial vortex. The grid size shown in Fig. 4.2 is based upon five grid points within the vortex core.

FLUENT solves the RANS equations over the grid specified. A user defined initialisation function is used to initialize the vortex in the uniform flow in the grid. For all the solutions of the 2D runs, a Rankine vortex with the following characteristics is used. All distances are non dimensionalised using a reference length $D = 1.0 m$, the velocities by a reference velocity $V_a = 1.0 m/s$ and time by $\frac{D}{V_a}$. The vortex strength is non dimensionalized as $\Gamma^* = \frac{\Gamma}{V_a D}$. The non dimensional variables parameters for the problem are

- Vortex core radius $r_o^* = r_o/D = 0.04$
- Circulation constant $\Gamma^* = 2\pi$
- The vortex is initialised at $(x, y) = (-0.25, 0)$ as shown in Fig. 4.2

The details of the FLUENT solver that is used to solve the problem of the 2D vortex in a uniform flow are as given below:

1. A 2 dimensional, cell based implicit solver is used.
2. The solver is unsteady and 2nd order implicit in time.
3. A laminar viscous model is used.
4. The fluid is water with kinematic viscosity = $10^{-6} \text{ m}^2/\text{s}$.
5. Reynolds number = 5×10^6 .
6. Boundary conditions for the grid shown in Fig. 4.2 are
 - Left face, Inflow velocity, $u_{in}^* = u_{in}/V_a = 5.0$, $v_{in}^* = v_{in}/V_a = 0.0$.
 - Right face, Outflow condition.
 - Top face, Wall with slip condition, i.e specified shear stress = 0 Pa in both x and y directions.
 - Bottom face, Wall with slip condition, i.e, specified shear stress = 0 Pa in both x and y directions.
7. A user defined initialization function is used to initialize the vortex in a uniform flow.

8. The discretization scheme is:

- ‘Standard’ discretization scheme for pressure.
- ‘Second order upwind’ scheme for momentum.

9. The ‘SIMPLE’ Pressure-Velocity coupling scheme is used.

10. The time step size used for the unsteady scheme is $\Delta t = 0.001 \text{ sec}$.

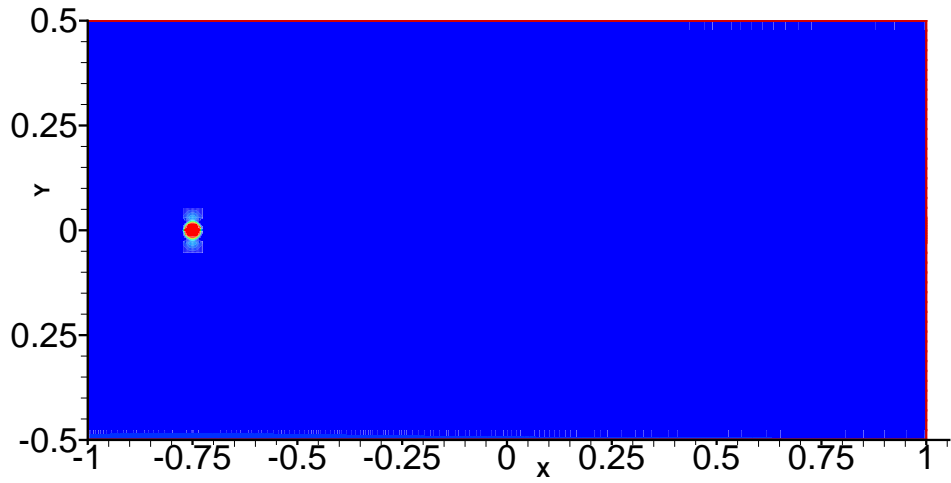
11. The convergence criteria for the solution is set as:

- Continuity = 10^{-5} .
- X velocity = 10^{-5} .
- Y velocity = 10^{-5} .

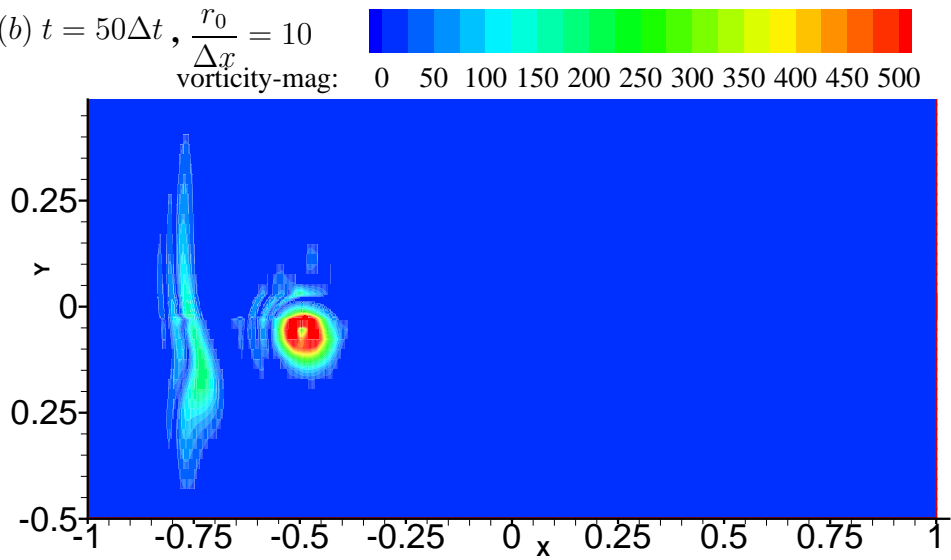
Let Δx and Δy be the grid sizes in x and y directions. As shown in Fig. 4.2, the grid in the vicinity of the initial location of the vortex consists of square cells of equal Δx and Δy . The results of the movement of a 2D vortex in a uniform flow are presented in Fig. 4.3. The grid size is based on $\frac{\Delta x}{r_0} = \frac{\Delta y}{r_0} = 10$, implying 10 grid points across the vortex core.

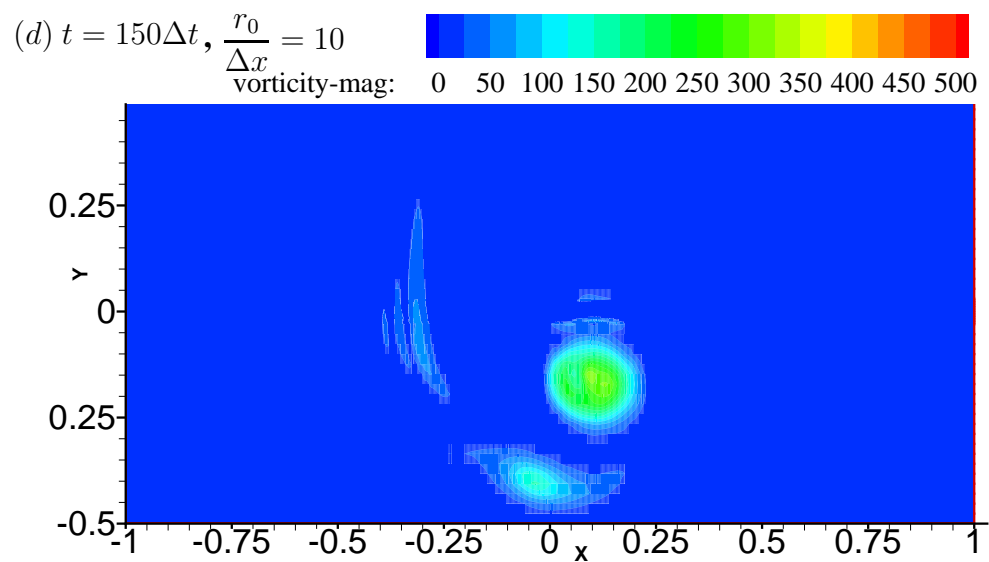
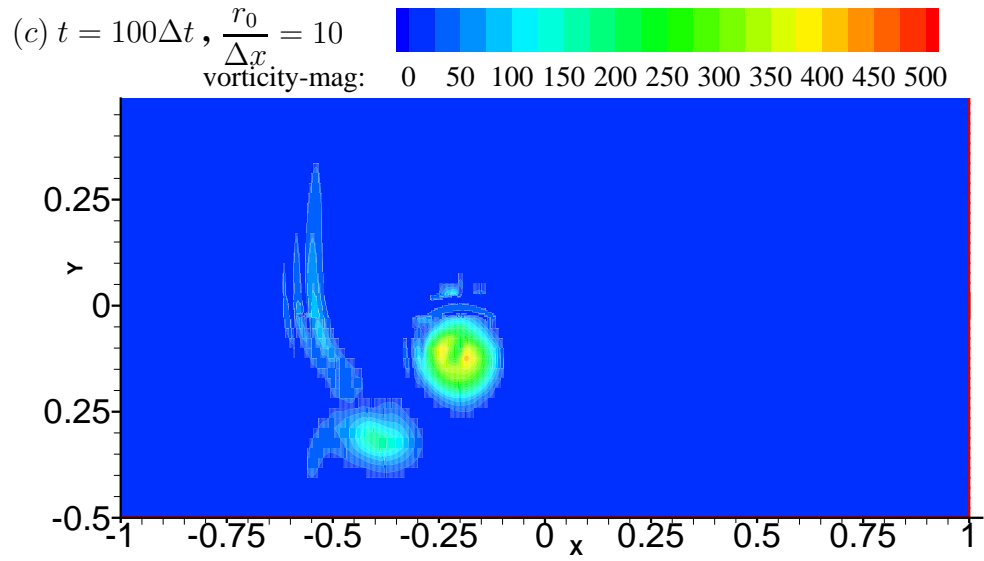
The vorticity contour plots are a good representation of the location of the vortex in space at different times. The vorticity contour plots are shown for every $t = 50\Delta t = 0.05 \text{ sec}$. The vortex travels a distance of $X = u_{in}t = 0.5 \text{ m}$ in time t .

(a) $t = 0, \frac{r_0}{\Delta x} = 10$



(b) $t = 50\Delta t, \frac{r_0}{\Delta x} = 10$





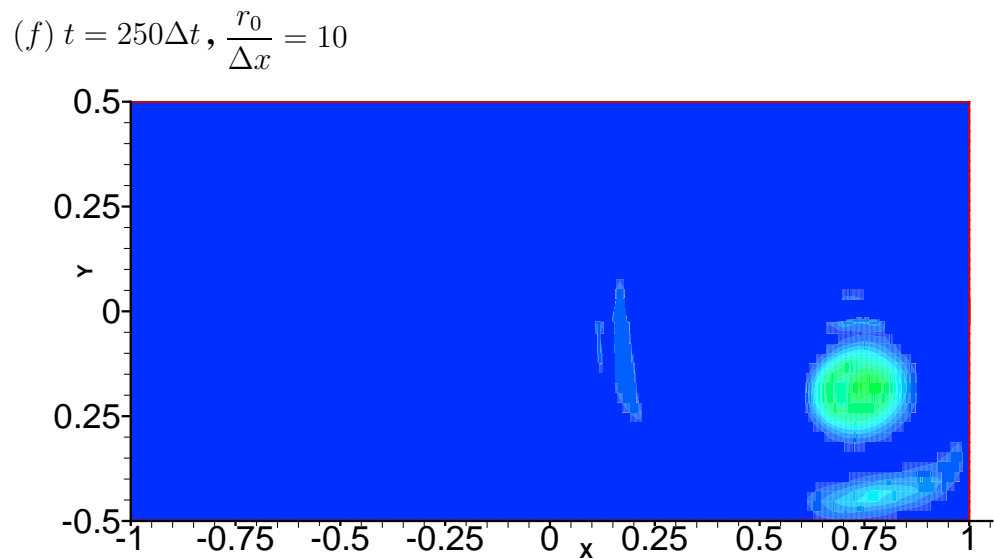
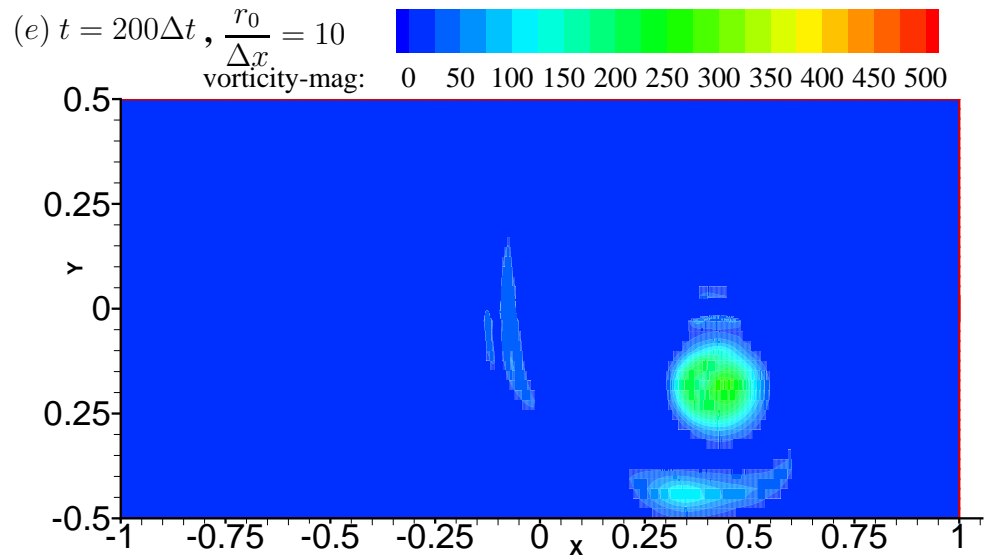


Figure 4.3: Vortex positions through vorticity contours shown at times (a) $t = 0$, (b) $t = 50\Delta t$, (c) $t = 100\Delta t$, (d) $t = 150\Delta t$, (e) $t = 200\Delta t$ and (f) $t = 250\Delta t$. $\Delta t = 0.001$ sec and $u_{in} = 5$ m/s.

The vorticity contours shown in the 2D space in Fig. 4.3 are a good measure of the location of the 2D vortex in space at a certain time t . As compared to the initial vortex at $t = 0$, the subsequent vortices show a vortex core spreading and the dissipation of vorticity, which is undesired. It can be seen from Figs. 1.1 and 1.2 that the tip vortex is a tightly bound vortex with little or no dissipation, even when the vortex has travelled the length of the rudder, at the trailing edge. This makes CFD models undesirable to study such phenomenon. From Fig. 4.3 it can also be noticed that the vortex in a uniform flow experiences a normal shift to the streamwise direction. This is due to the Kutta-Joukowski law, which states that a circulation in a uniform flow induces a lift force on the vortex which acts normal to the flow direction. Also, a secondary vortex can be seen along with the initial vortex. This happens because the vortex is initialised quite close to the inflow boundary, where the boundary condition creates a new vorticity.

Several studies were done in order to gain a better understanding of the vortex model to be used to solve the vortex hydrofoil interactions. The following runs were done to understand the impact of the spatial discretization on the vortex strength through time. Different grids were used based on $\frac{r_0}{\Delta x} = 2$, $\frac{r_0}{\Delta x} = 5$, $\frac{r_0}{\Delta x} = 10$ and $\frac{r_0}{\Delta x} = 20$, corresponding to 2, 5, 10 and 20 grid points across the vortex core. All the parameters are same for all the above runs and results are shown for every $t = 50\Delta t = 0.05$.

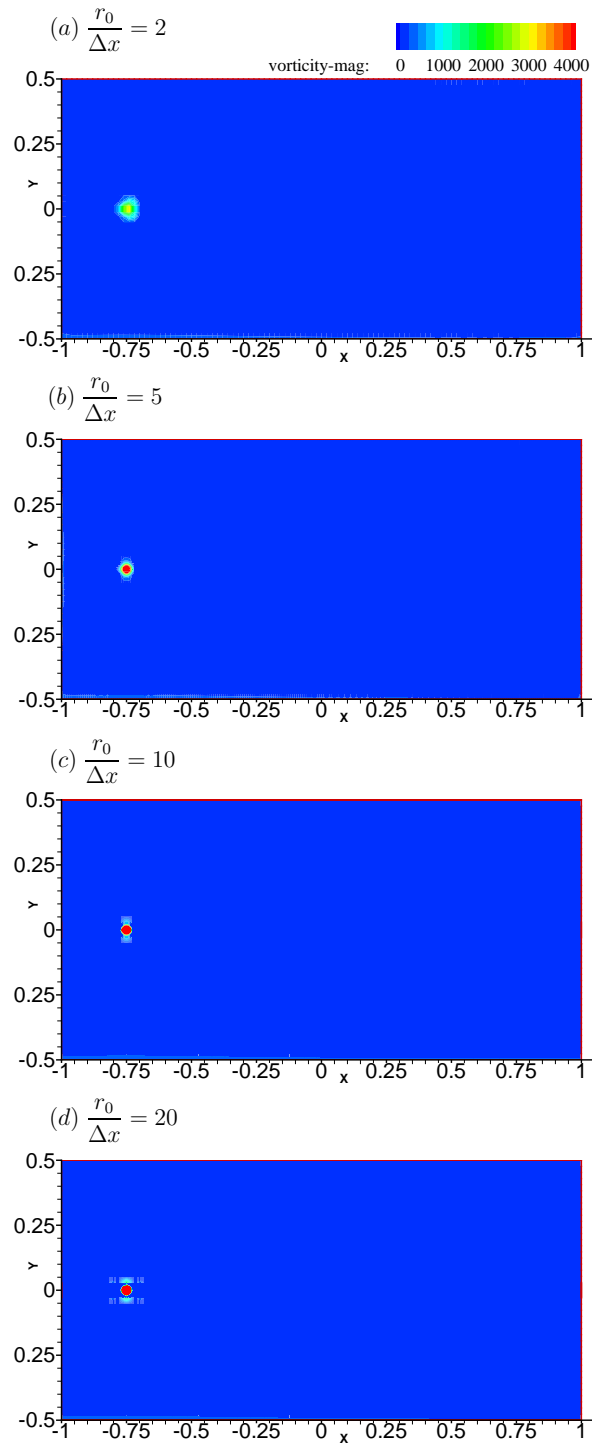


Figure 4.4: Vorticity contours shown for (a) $\frac{r_0}{\Delta x} = 2$, (b) $\frac{r_0}{\Delta x} = 5$, (c) $\frac{r_0}{\Delta x} = 10$ and (d) $\frac{r_0}{\Delta x} = 20$ at $t = 0$. $r_o^* = 0.02$, $u_{in} = 5.0 \text{ m/s}$ and $\Delta t = 0.001 \text{ sec}$.

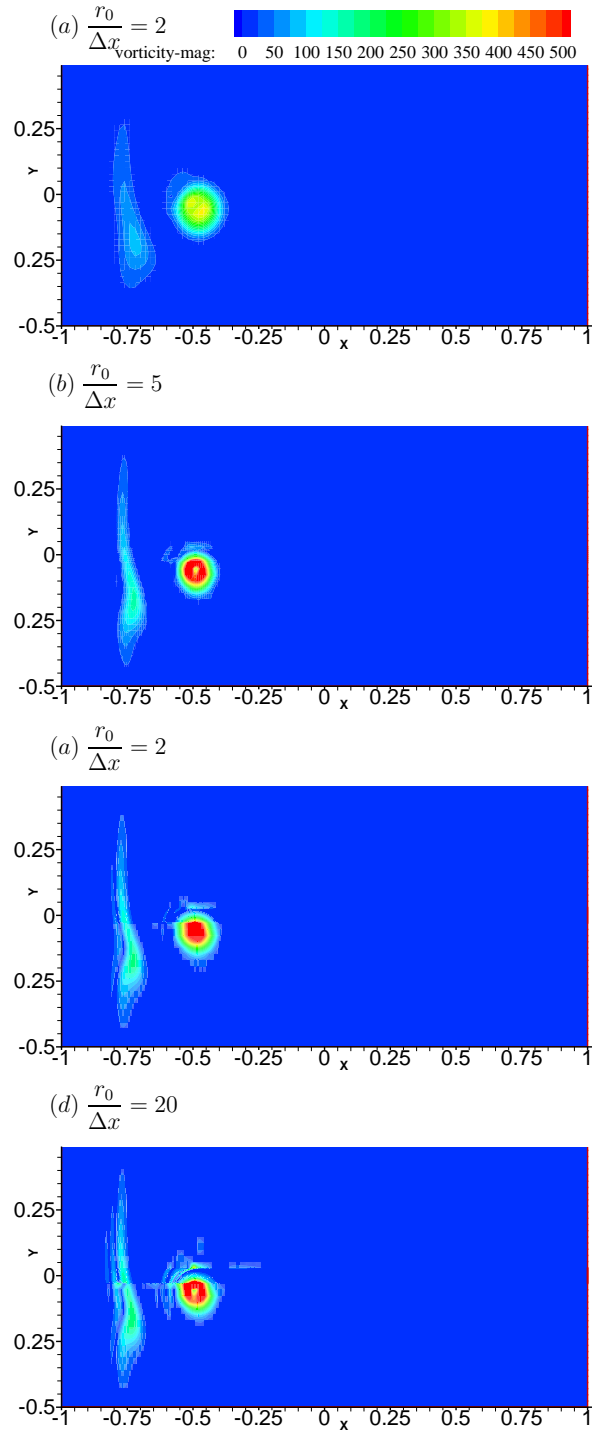


Figure 4.5: Vorticity contours shown for (a) $\frac{r_0}{\Delta x} = 2$, (b) $\frac{r_0}{\Delta x} = 5$, (c) $\frac{r_0}{\Delta x} = 10$ and (d) $\frac{r_0}{\Delta x} = 20$ at $t = 50\Delta t$. $r_o^* = 0.02$, $u_{in} = 5.0 \text{ m/s}$ and $\Delta t = 0.001 \text{ sec}$.

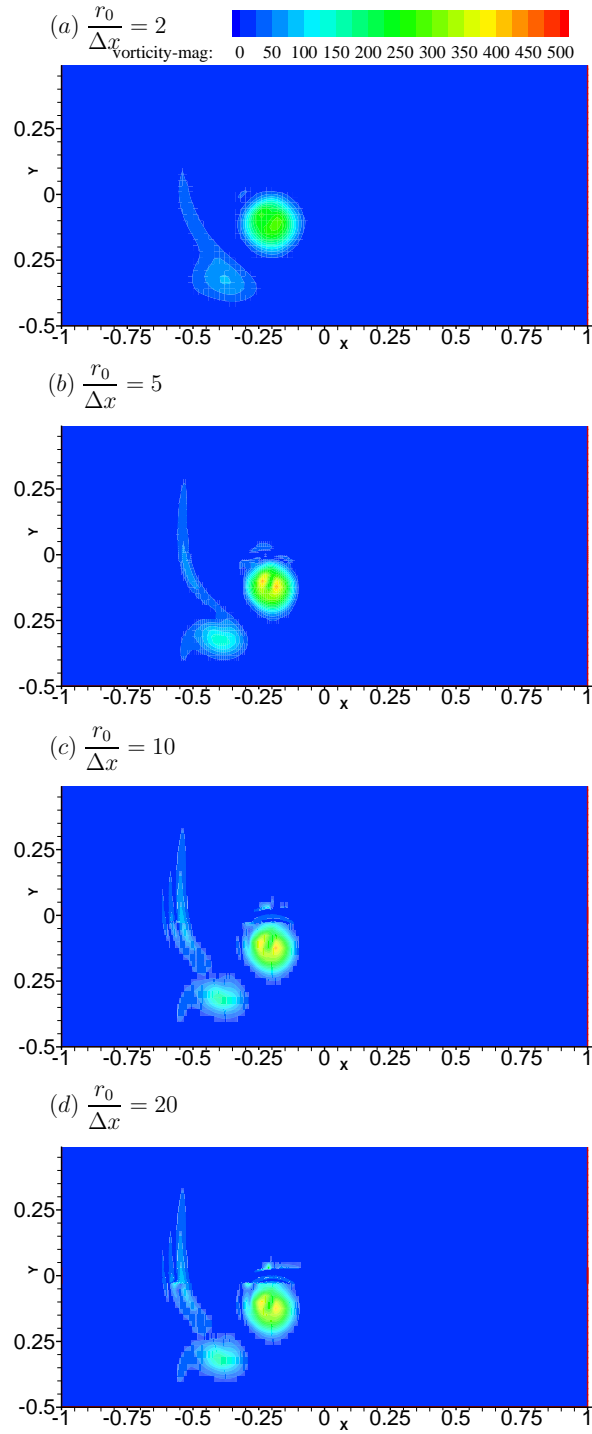


Figure 4.6: Vorticity contours shown for (a) $\frac{r_0}{\Delta x} = 2$, (b) $\frac{r_0}{\Delta x} = 5$, (c) $\frac{r_0}{\Delta x} = 10$ and (d) $\frac{r_0}{\Delta x} = 20$ at $t = 100\Delta t$. $r_o^* = 0.02$, $u_{in} = 5.0 \text{ m/s}$ and $\Delta t = 0.001 \text{ sec}$.

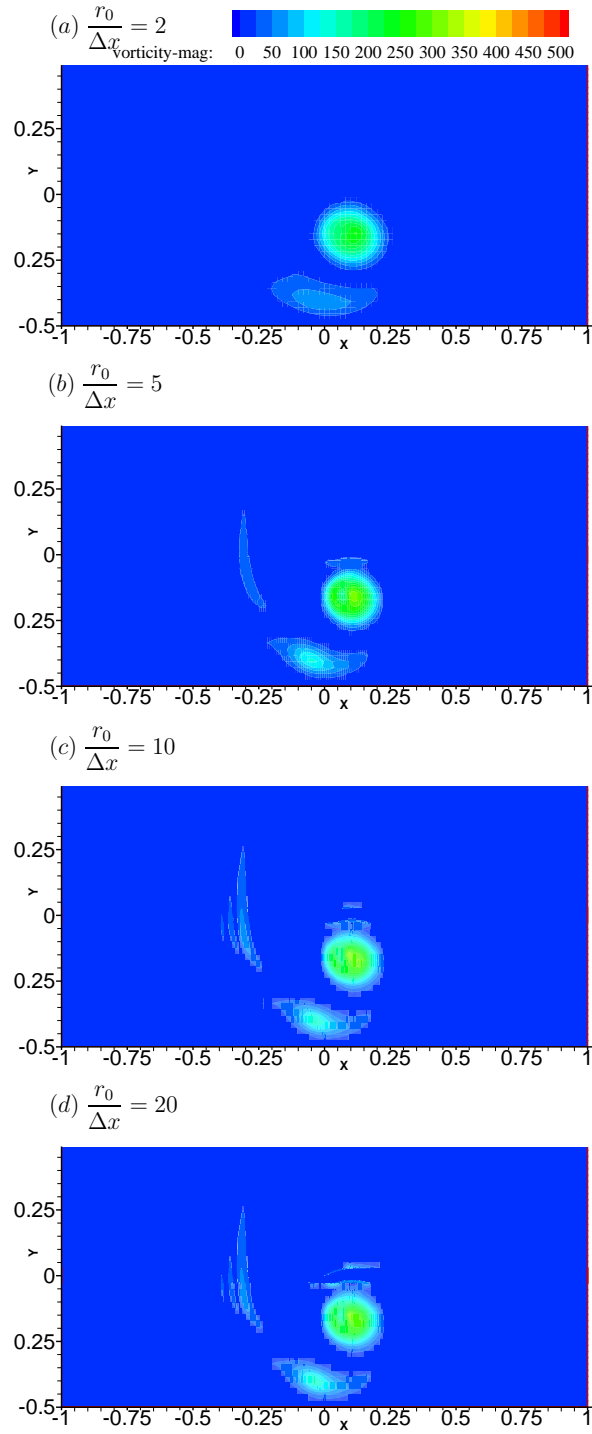


Figure 4.7: Vorticity contours shown for (a) $\frac{r_0}{\Delta x} = 2$, (b) $\frac{r_0}{\Delta x} = 5$, (c) $\frac{r_0}{\Delta x} = 10$ and (d) $\frac{r_0}{\Delta x} = 20$ at $t = 100\Delta t$. $r_o^* = 0.02$, $u_{in} = 5.0 \text{ m/s}$ and $\Delta t = 0.001 \text{ sec}$.

From Fig. 4.7, the effect of the spatial discretization can be seen. These results show that the number of points required to initially define the vortex core plays an important role in the conservation of vorticity as the vortex convects downstream. The numerical scheme already has a numerical dissipation associated with it, which results in information being lost, which in this case is the strength of the vortex as it convects. Apart from the numerical dissipation, the spatial discretization also has an effect on the dissipation of vorticity as seen from Fig. 4.7.

The cases for $\frac{r_0}{\Delta x} = 2$ and 5 show more dissipation when compared to $\frac{r_0}{\Delta x} = 10$ and 20, where the vorticity magnitudes are almost the same, as is evident from the contour plots. Using these results, it was decided to use $\frac{r_0}{\Delta x} = 10$ to model the vortex core in a three dimensional field in the presence of a foil.

The order of the unsteady time stepping scheme also plays an important role in controlling the numerical dissipation present in the solver. The vorticity magnitudes are compared for a first and a second order implicit unsteady scheme. The vortex core for both cases has a radius of $r_o^* = 0.02$, the inflow velocity $u_{in} = 5 \text{ m/s}$, the number of points along the vortex core $\frac{r_o}{\Delta x} = 10$ and the time step size $\Delta t = 0.001 \text{ sec}$.

From Fig. 4.8, it can be seen that the first order implicit scheme has an additional numerical dissipation, other than the inherent numerical dissipation present in the solver. It can be seen that the second order implicit scheme conserves vorticity better than the first order implicit scheme. Hence, the second order implicit scheme is used to model the three dimensional vortex hydrofoil interactions.

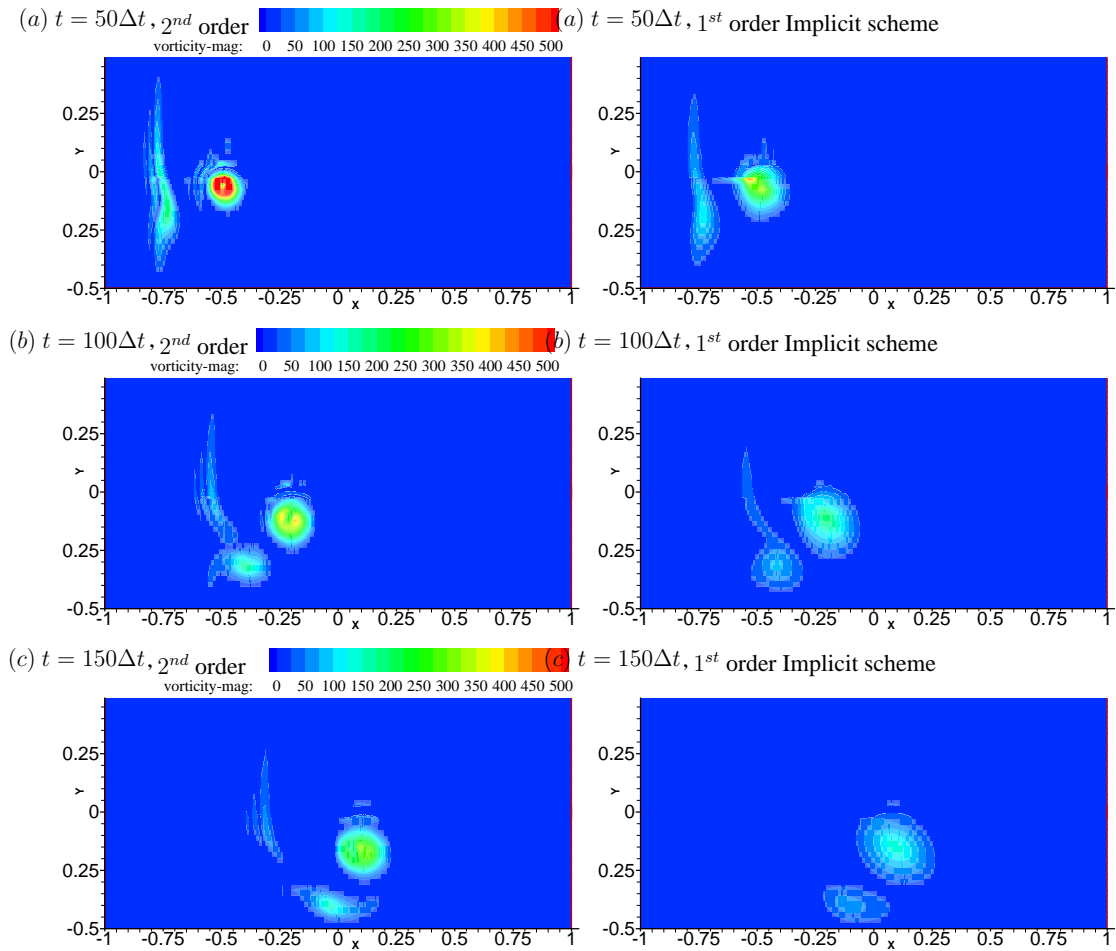


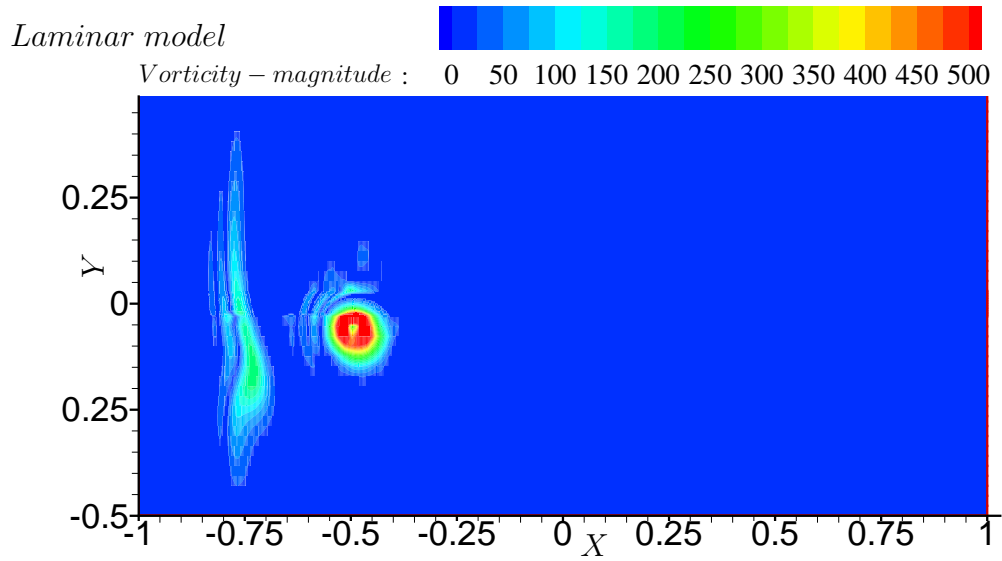
Figure 4.8: Comparison of vorticity magnitudes at (a) $t = 50\Delta t$, (b) $t = 100\Delta t$ and (c) $t = 150\Delta t$ between 1^{st} and 2^{nd} order implicit unsteady scheme.

It is important to understand the effect of turbulence modeling on the dissipation of vorticity as the vortex convects downstream. A study was done to compare the vorticity magnitudes as the vortex convects downstream between a laminar model and a $k - \epsilon$ turbulence model. The details of the FLUENT run are as before for both the runs. For the $k - \epsilon$ model, the additional details of the run are

- Turbulence kinetic energy = $0.0361 \text{ m}^2/\text{s}^2$
- Turbulence dissipation rate = $0.00161 \text{ m}^2/\text{s}^3$

The vorticity contours are shown at every $t = 50\Delta t$, where $\Delta t = 0.001\text{sec}$ in Figs. 4.9 to 4.11.

As expected, the turbulence model shows more dissipation in the vorticity magnitude as compared to the laminar model. This happens because the turbulence models have an inherent dissipation term which tends to dissipate the vorticity.



k – ϵ model

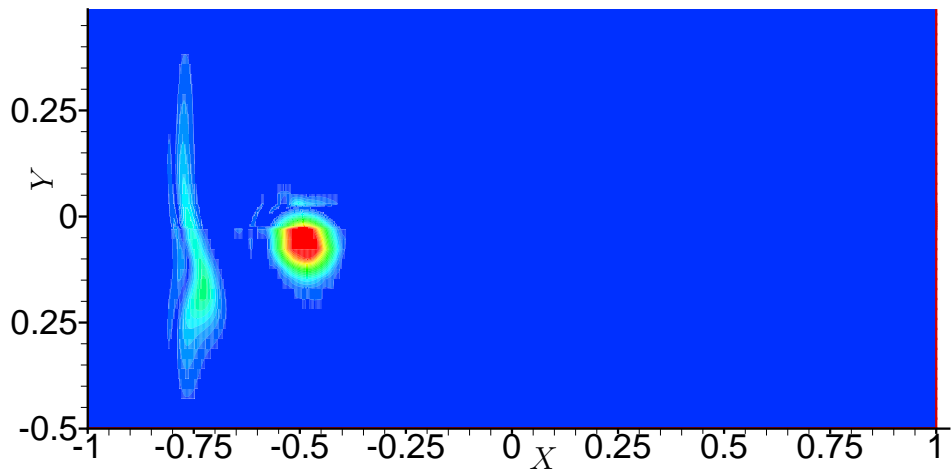


Figure 4.9: Vorticity contours shown at $t = 50\Delta t$ for *Laminar* and *k – ϵ* models. $\Delta t = 0.001\text{sec}$.

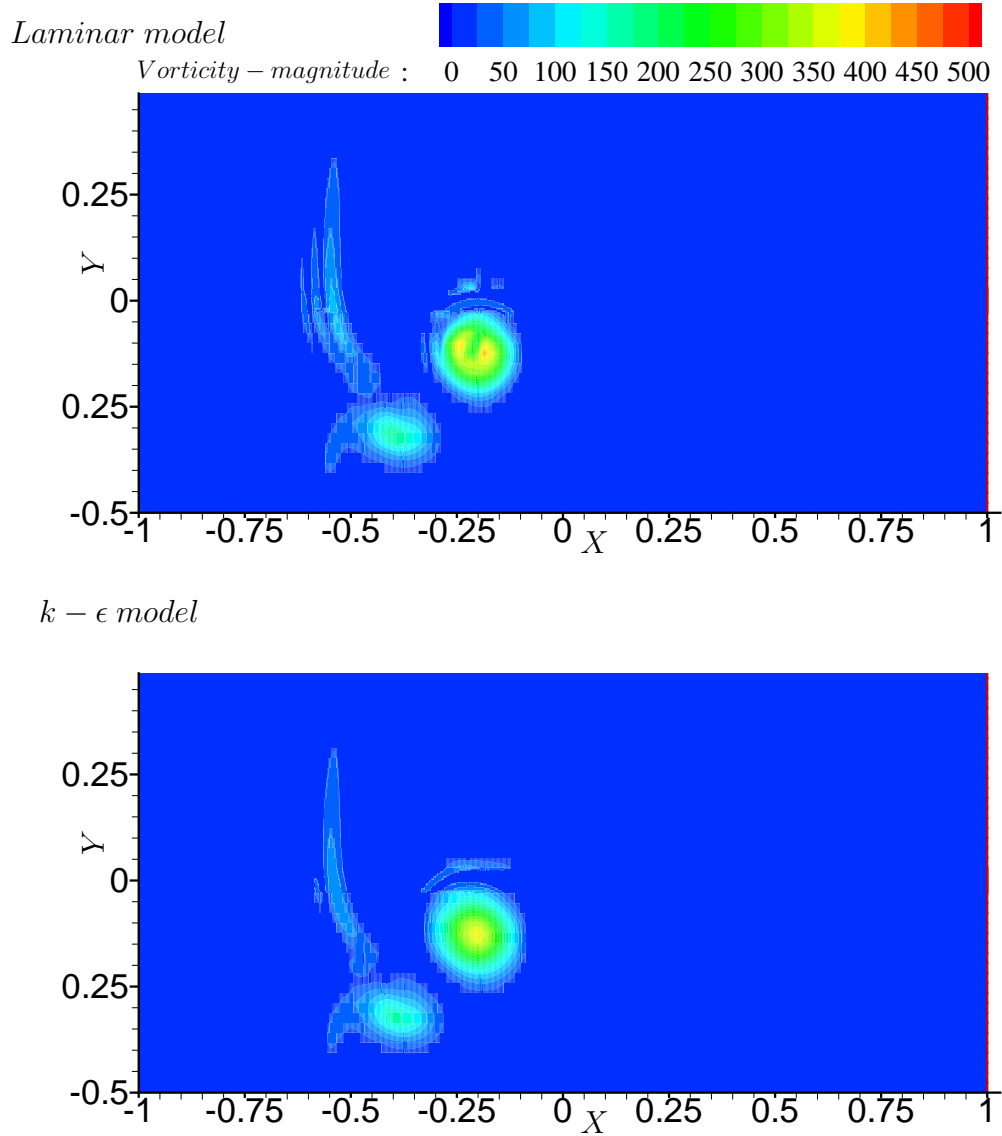


Figure 4.10: Vorticity contours shown at $t = 100\Delta t$ for *Laminar* and *k – ε* models. $\Delta t = 0.001\text{sec}$.

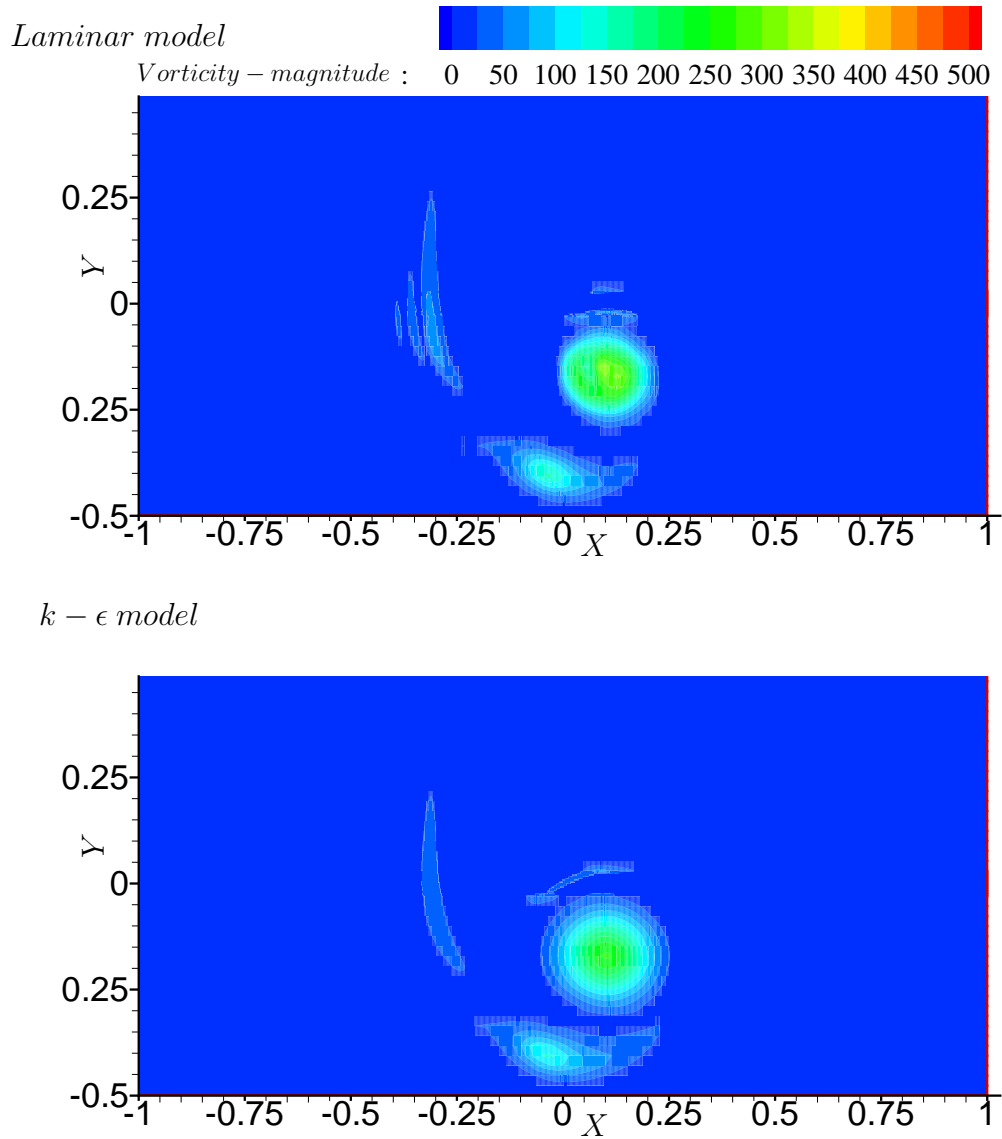


Figure 4.11: Vorticity contours shown at $t = 150\Delta t$ for *Laminar* and *k – ε* models. $\Delta t = 0.001\text{sec}$.

4.2 3D Vortex/hydrofoil interactions in a uniform flow

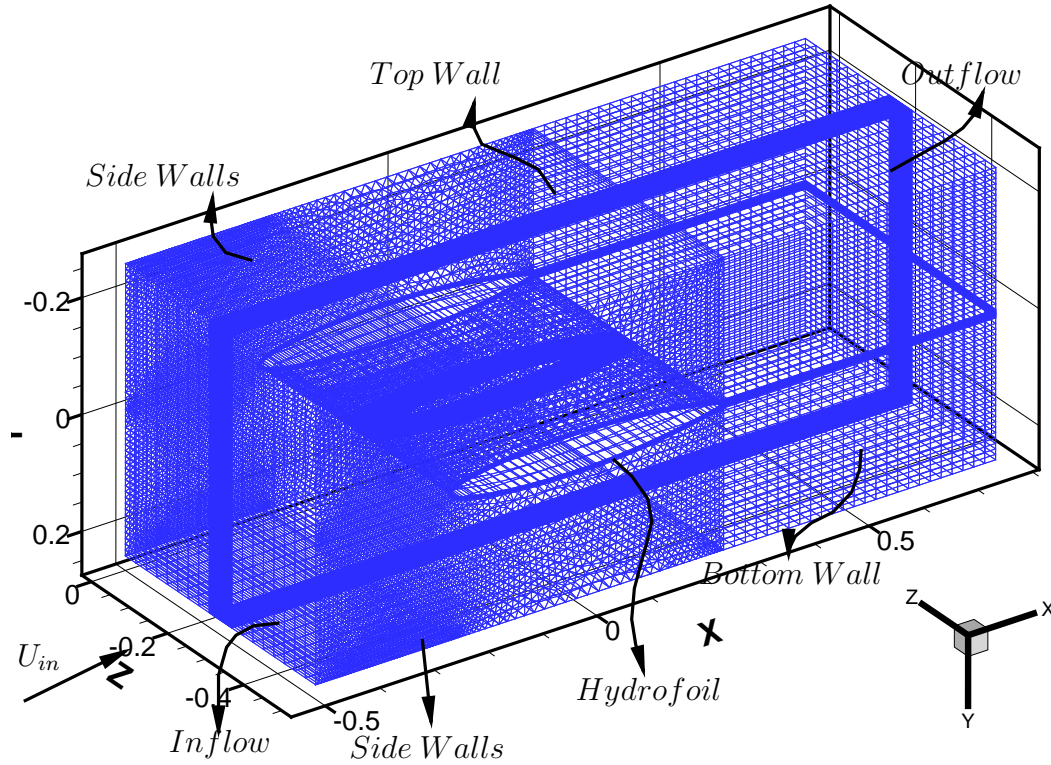


Figure 4.12: Domain for 3d vortex/hydrofoil interactions.

The domain for a 3D vortex hydrofoil model is as shown in Fig. 4.12. The grid in the $x - y$ plane, through the mid of the domain at $z = -0.25$ and the grid in the $x - z$ plane at $y = 0.05$ is shown in Fig. 4.13

The grid size was determined based on $\frac{r_0}{\Delta x} = 10$. In order to reduce computational time, a denser grid was clustered around the region where the vortex is being initialised and in the path of the region. The main priority in this model was to capture the pressure distributions on the hydrofoil as the vortex approaches the hydrofoil and passes over it.

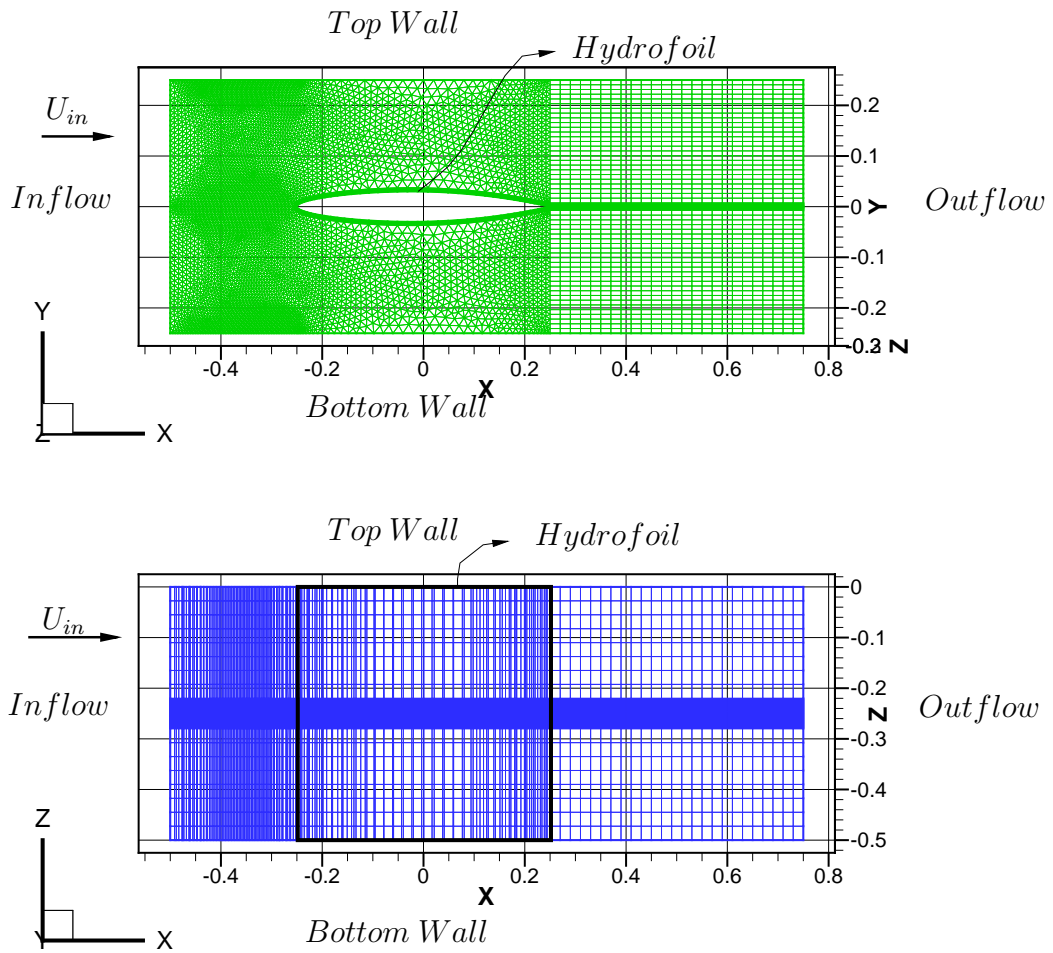


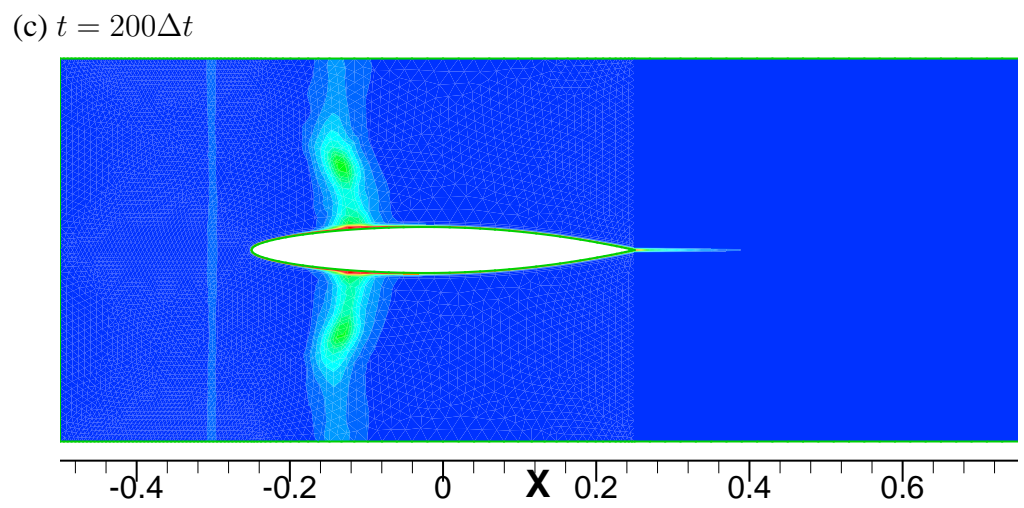
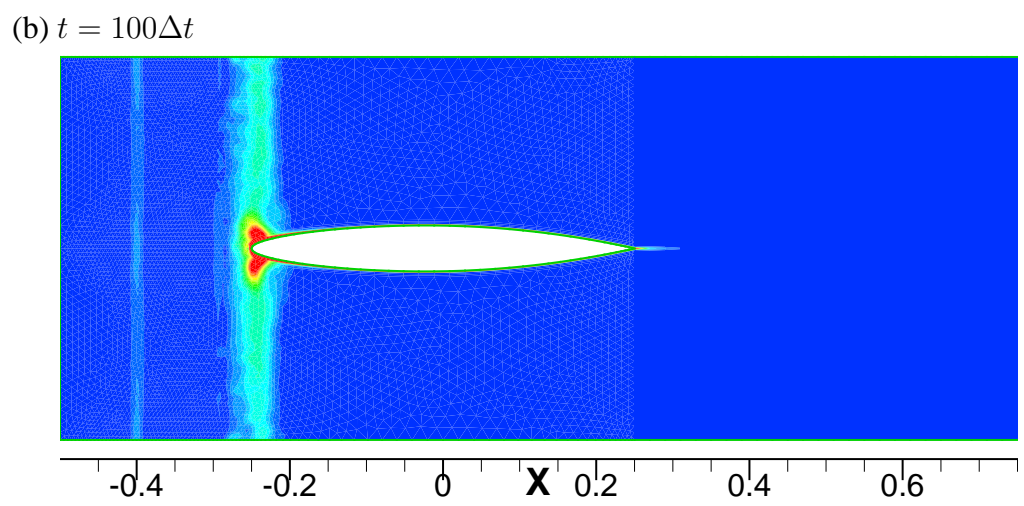
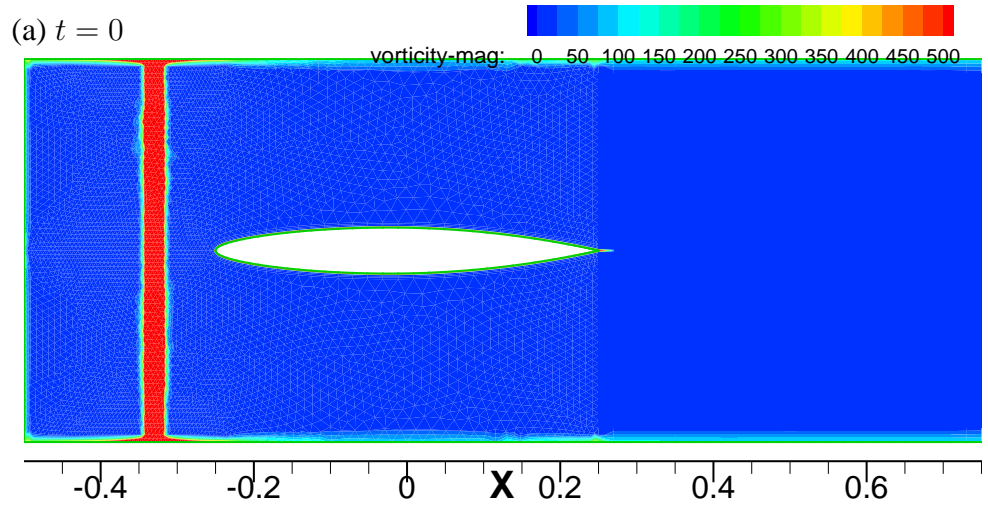
Figure 4.13: The 3D grid in the (a) $x - y$ plane at $z = -0.25$ and (b) $x - z$ plane at $y = 0.05$.

The run conditions of FLUENT are as given below. As in the case of the 2D problem, all the variables were non dimensionalized by reference variables, as mentioned earlier.

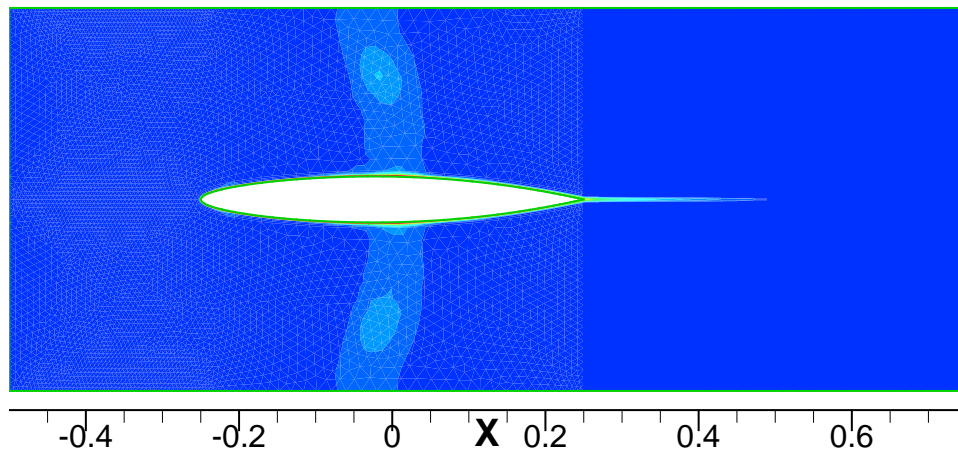
1. The number of cells in the domain = 1.8 million.
2. A three dimensional, cell based implicit solver is used.
3. The solver is unsteady and 2nd order implicit in time.
4. A laminar viscous model is used.
5. Reynolds number = 10^6 .
6. The fluid used is water with viscosity = $10^{-6} \text{ m}^2/\text{s}$.
7. Boundary conditions for the grid shown in Fig. 4.12 are:
 - Inflow velocity, $u_{in} = 1.0 \text{ m/s}$, $v_{in} = 0.0 \text{ m/s}$ and $w_{in} = 0.0 \text{ m/s}$.
 - Right face, Outflow condition.
 - The top, bottom and side faces are ‘Wall’ boundary conditions with slip condition, i.e, specified shear stress = 0 Pa , in x, y and z directions is applied.
 - On the hydrofoil surface, ‘Wall’ boundary condition with no slip condition, i.e, velocity on the foil surface = 0 m/s is applied.
8. A user defined initialization function is used to initialize the vortex in a uniform flow.
9. The discretization scheme used is:

- ‘Standard’ discretization scheme for pressure.
 - ‘Second order upwind’ scheme for momentum.
10. The ‘SIMPLE’ Pressure-Velocity coupling scheme is used.
 11. The time step size used for the unsteady scheme is $\Delta t = 0.001 \text{ sec}$.
 12. The convergence criteria for the solution is set as:
 - Continuity = 10^{-5} .
 - X velocity = 10^{-5} .
 - Y velocity = 10^{-5} .
 - Z velocity = 10^{-5} .

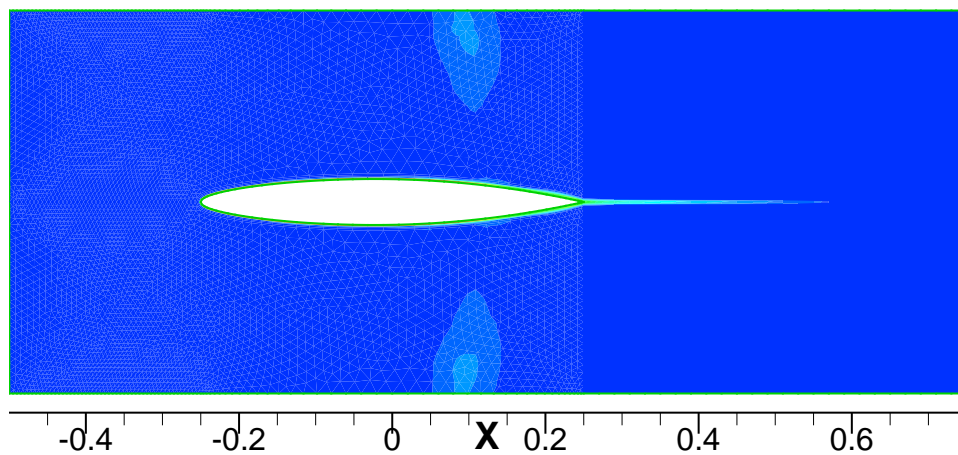
The vortex locations is showed in Fig. 4.14 through the contour plots of vorticity in the $x - y$ plane, passing through the middle of the vortex core at various time steps.



(d) $t = 300\Delta t$



(e) $t = 400\Delta t$



(f) $t = 500\Delta t$

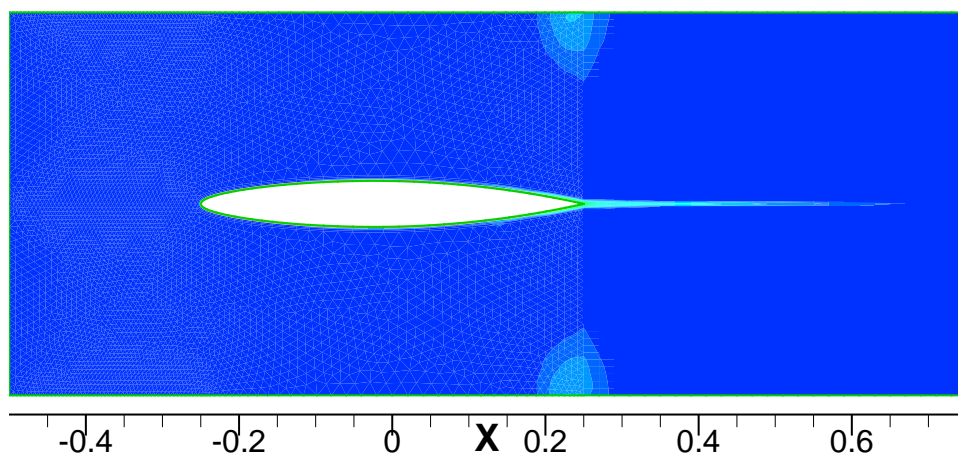
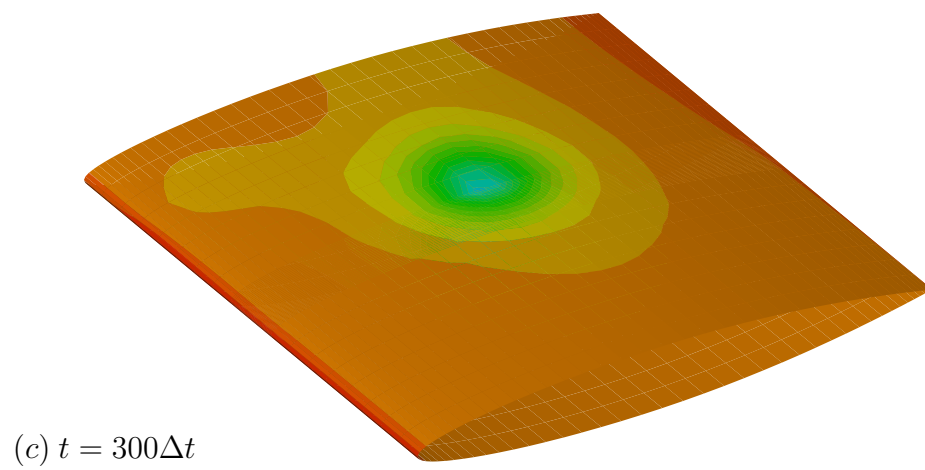
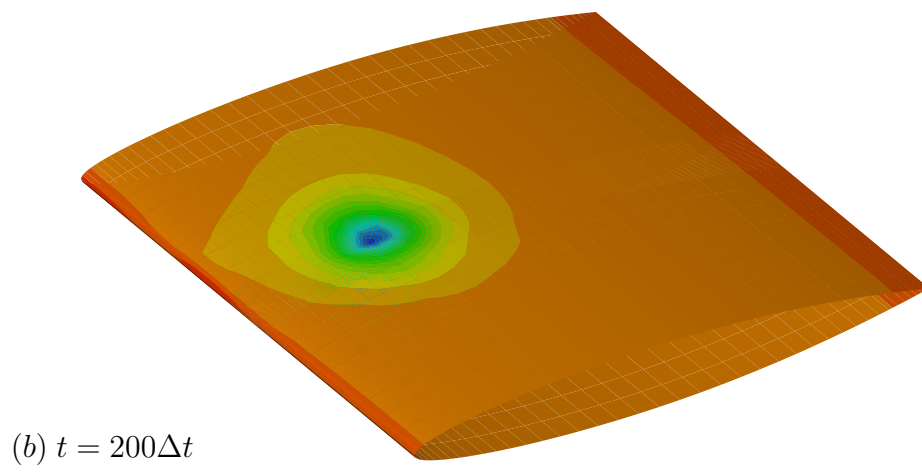
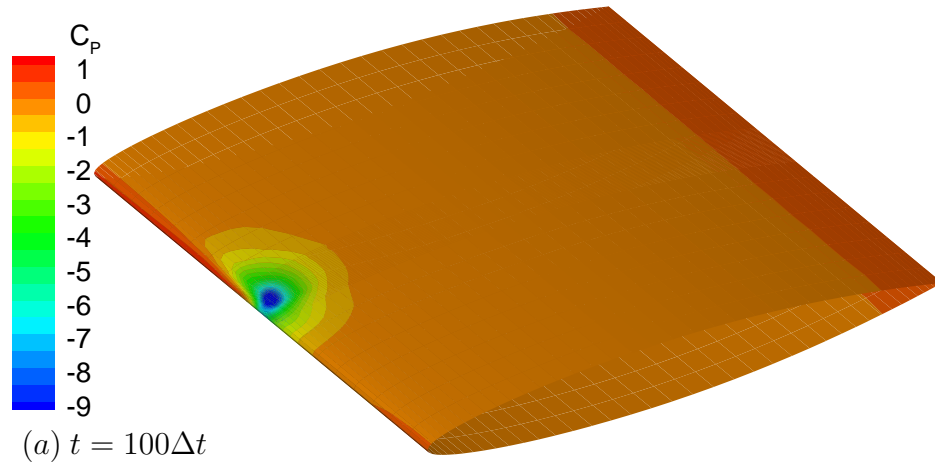


Figure 4.14: Vorticity contours shown in the $x - y$ plane at (a) $t = 0$, (b) $t = 100\Delta t$, (c) $t = 200\Delta t$, (d) $t = 300\Delta t$,⁶⁵ and (e) $t = 400\Delta t$. $\Delta t = 0.001$ sec and $u_{in} = 1.0$ m/s.



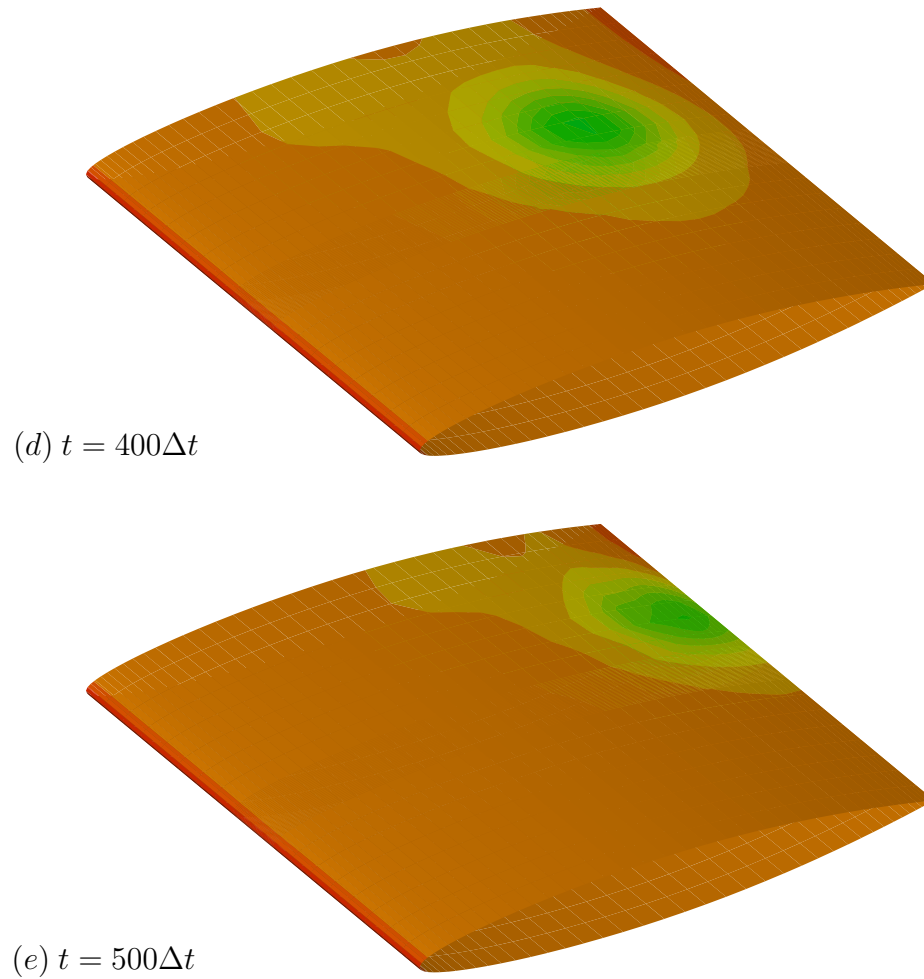


Figure 4.15: Contours of C_P on the foil surface shown at times (a) $t = 100\Delta t$, (b) $t = 200\Delta t$, (c) $t = 300\Delta t$, (d) $t = 400\Delta t$ and (e) $t = 500\Delta t$.

The contours of the pressure distribution C_P are shown on the foil surface in Fig. 4.15 at the time steps shown in Fig. 4.14

In Fig. 4.15, it can be seen that the presence of a vortex induces very low pressures on the hydrofoil surface. The location on the low pressures on the foil surface corresponds to the location of the vortex over the hydrofoil. As seen in Fig. 4.14,

the vortex core diameter increases to compensate for the viscous dissipation in vorticity in order to conserve circulation. This increase in core diameter also causes an increased area of the hydrofoil to experience low pressures. This could lead to the prediction of cavitation over a large area of the hydrofoil due to the vortex. In reality, the tip vortices impinging on the rudder have a very small diameter when compared to the rudder span or chord. Also, these vortices do not dissipate much and they retain the same core size as the tip vortices travel over the rudder. Accurately modeling these small tip vortices requires a denser grid, compared to the grid of Fig. 4.12, thus increasing the total grid size and the computational time.

The 3D vortex/hydrofoil interaction problem is also solved for a cambered foil. The details of the solution are similar to those of the symmetric hydrofoil. The domain used for the model is similar to that shown in Fig. 4.12 for a symmetric foil.

The grid is also shown in the $x - y$ and the $x - z$ plane in Fig. 4.16.

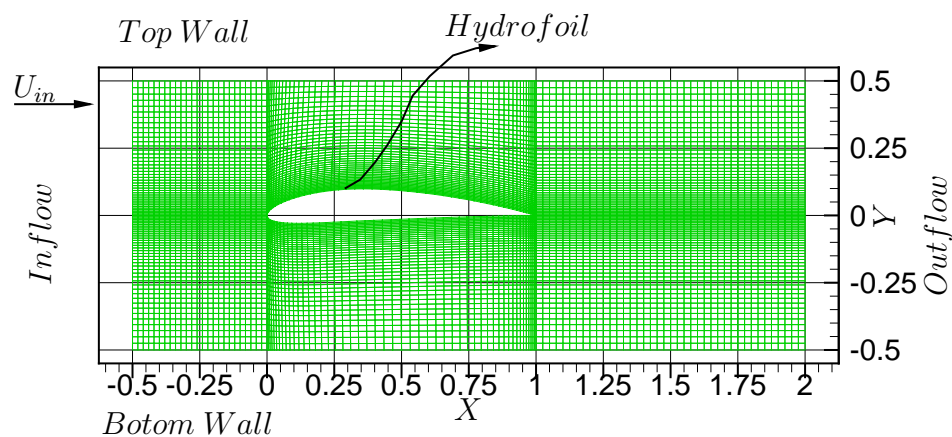


Figure 4.16: The grid for a vortex/cambered foil interaction shown in the $x - y$ plane.

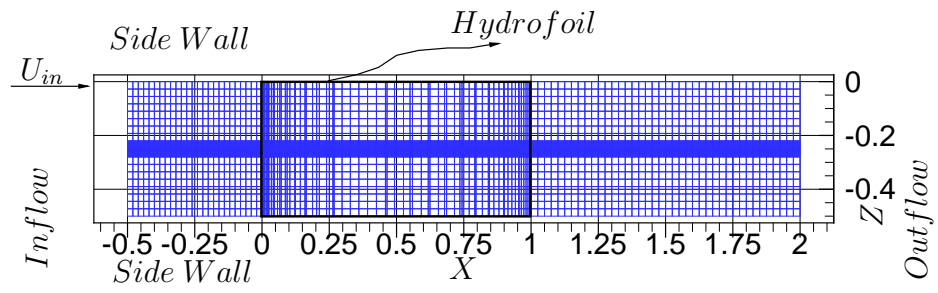
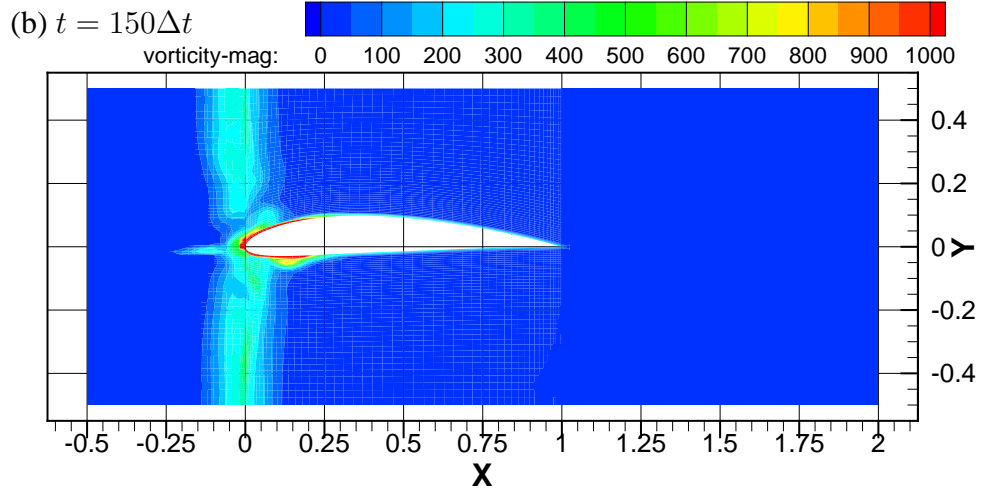
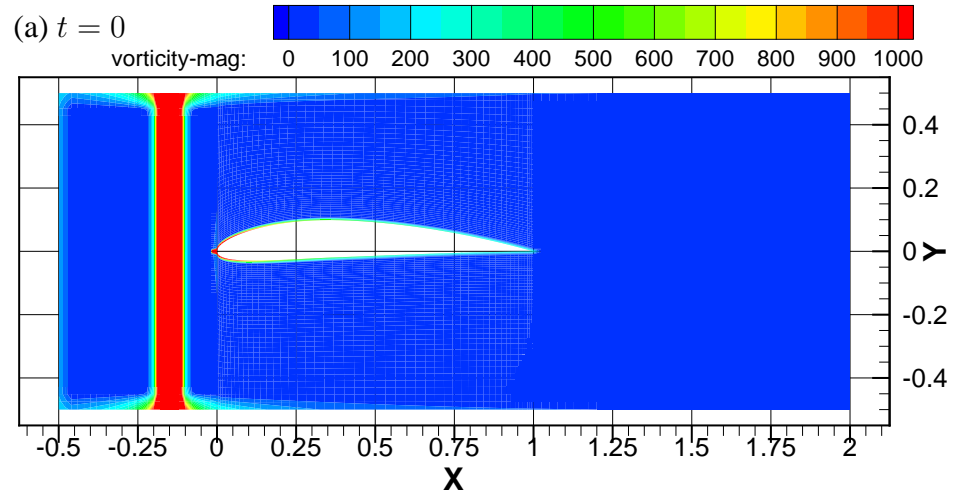
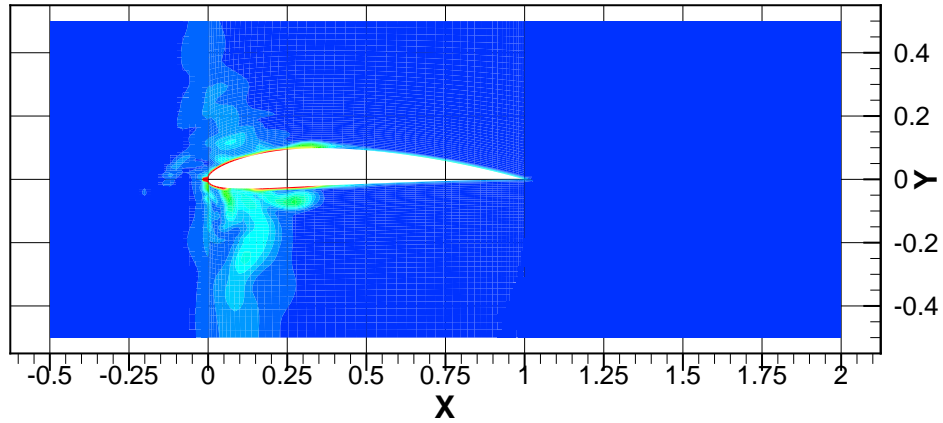


Figure 4.17: The grid for a vortex/cambered foil interaction shown in the $x-z$ plane.

Fig. 4.18 shows the vortex locations at different times through vorticity contour plots in the $x - y$ plane passing through the middle of the vortex core.



(c) $t = 300\Delta t$



(d) $t = 450\Delta t$

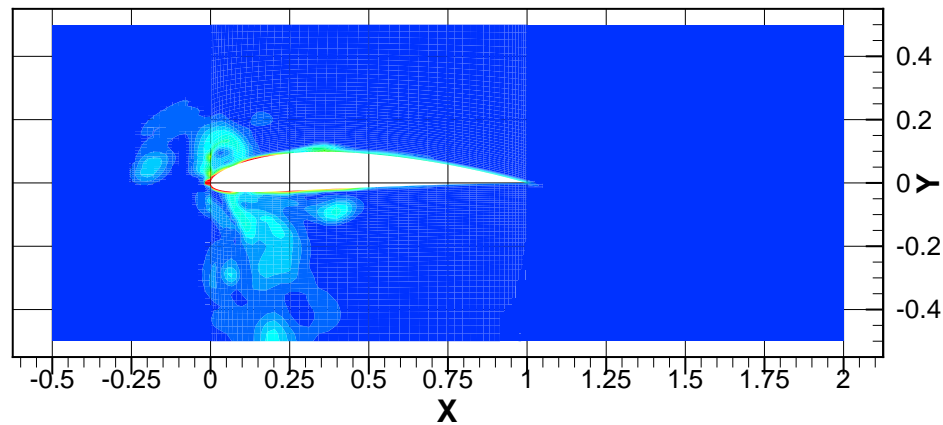
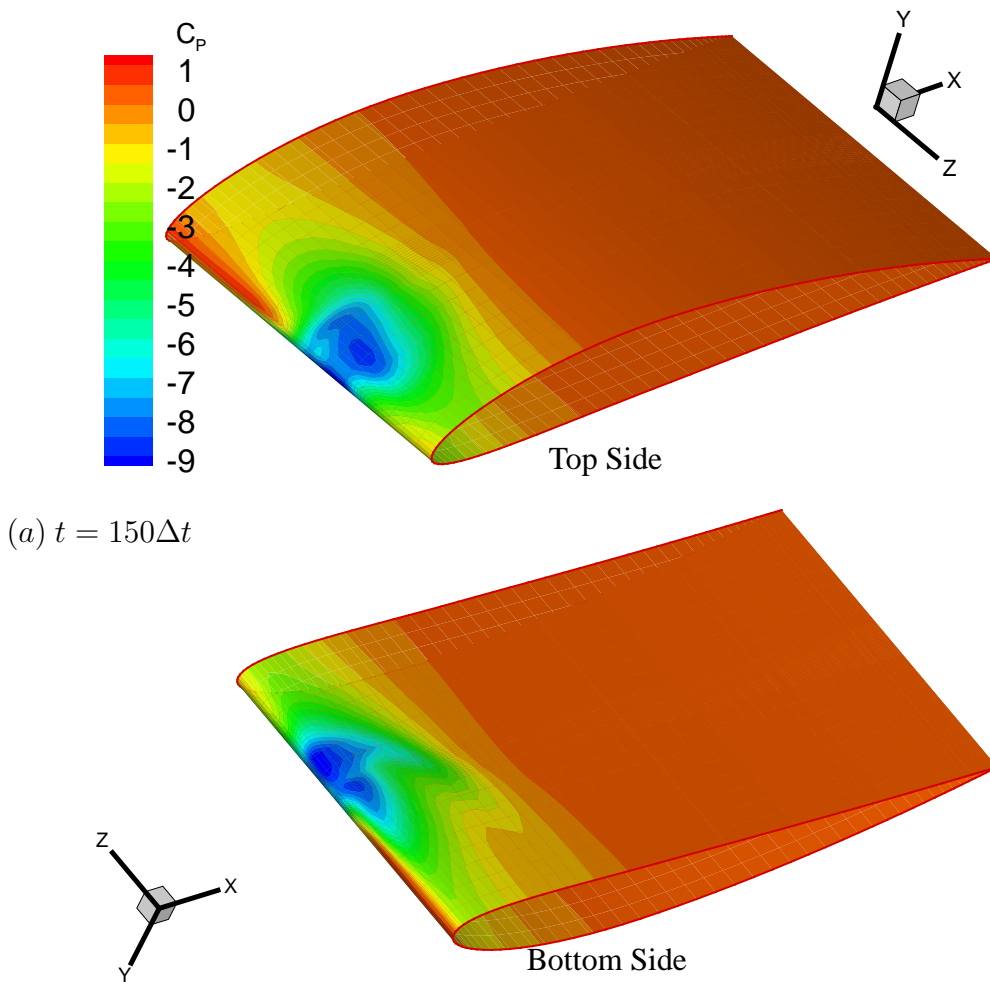


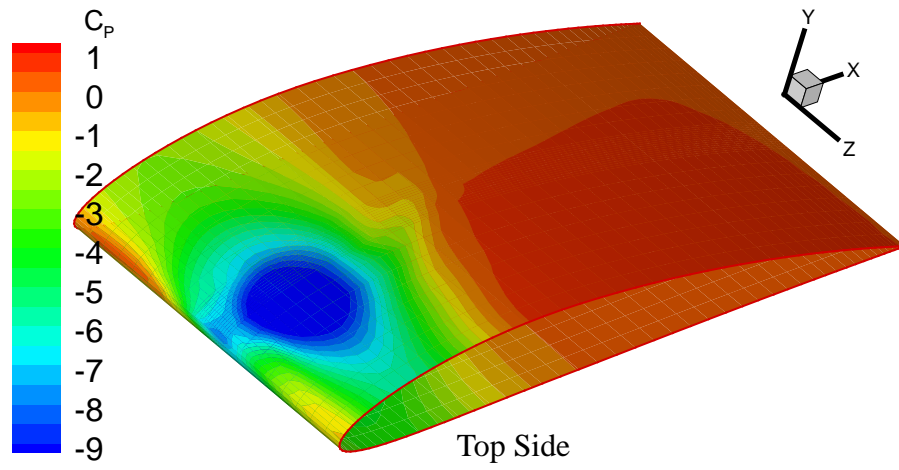
Figure 4.18: Vorticity magnitude in x-y plane for (a) $t = 0$, (b) $t = 150\Delta t$, (c) $t = 300\Delta t$ and (d) $t = 450\Delta t$. $\Delta t = 0.001$ and $U_{in} = 1.0$.

From Fig. 4.18, it can be seen that the vortex dissipates more rapidly than in the case of the symmetric hydrofoil. Even before the vortex reaches the mid chord region, it has dissipated. However at $t = 150\Delta t$, it can be seen that the vortex has split into two parts and the lower part of the vortex seems to move faster than the upper part. This happens because the total velocity in the field around a cambered hydrofoil,

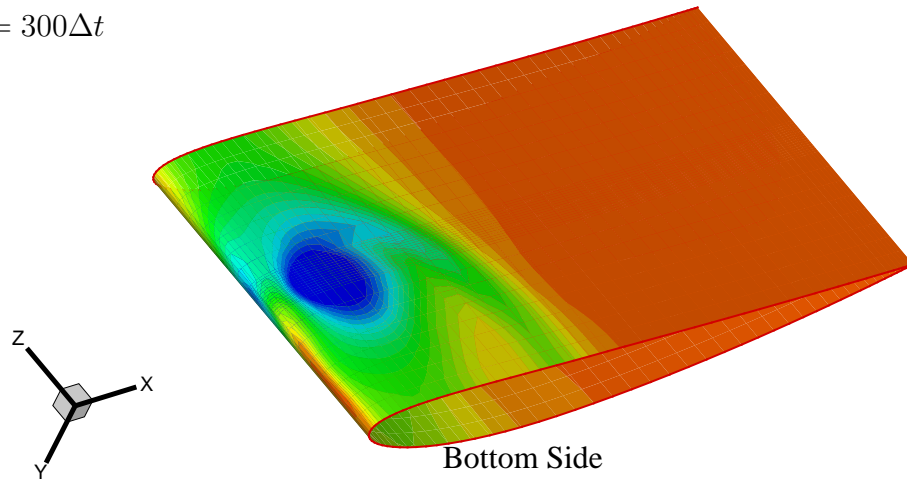
when the foil is at 0° angle of attack induces a lift force. This causes the velocity below the cambered foil to be higher than the velocity on the upper side of the foil and thus the lower part of the vortex moves faster than the upper part of the vortex.

The pressure contours on the cambered foil surface at the various vortex locations at different times are shown in Fig. 4.19.





(b) $t = 300\Delta t$



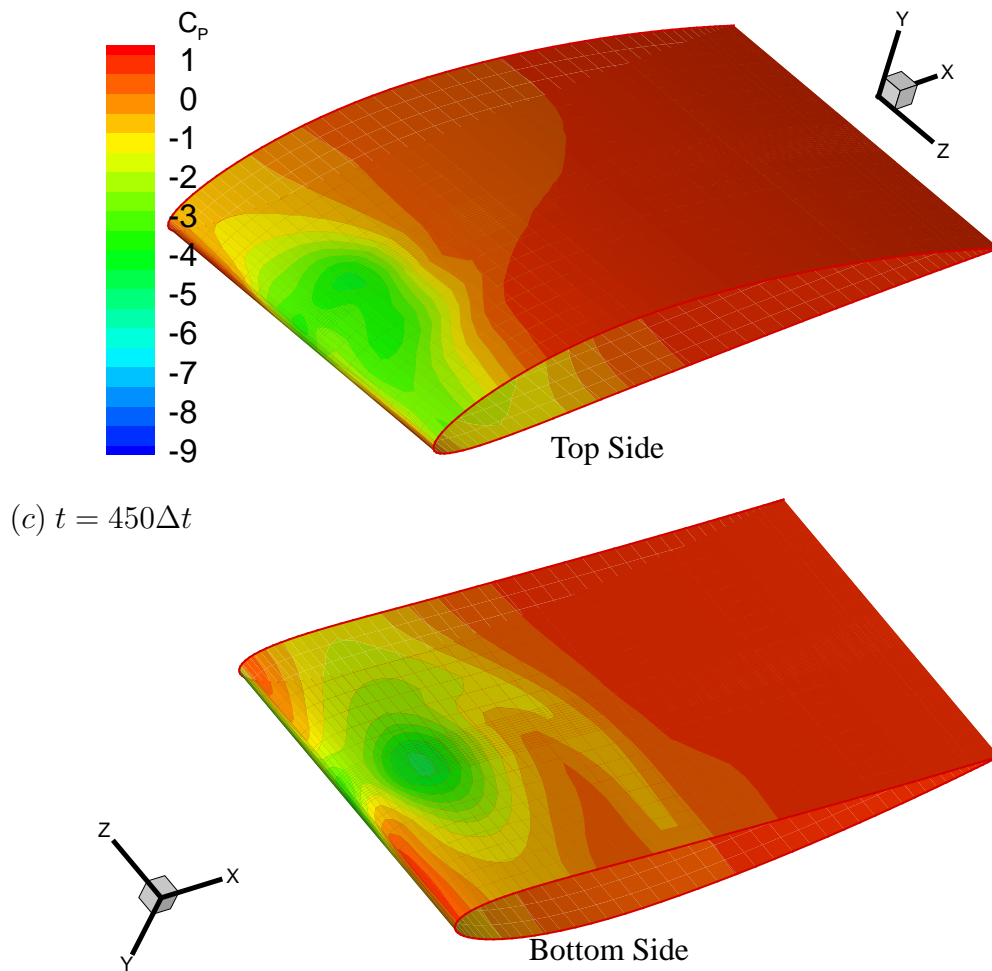


Figure 4.19: Contours of C_P over the foil surface at (a) $t = 150\Delta t$, (b) $t = 300\Delta t$ and (c) $t = 450\Delta t$.

The pressure distributions on the cambered foil again show low pressures in the vicinity of the hydrofoil, as is shown in Fig. 4.19. Also, it can be seen that the pressure distributions correspond to the vortex locations.

Chapter 5

Vortex/Hydrofoil Interactions Using PROPCAV

In the previous chapter, the results were shown for 3D vortex/hydrofoil interactions using a commercial CFD solver, FLUENT. Using a CFD model for vortex dynamics and vortex/hydrofoil interactions has several drawbacks. The necessity for meshing the entire domain of the problem makes it cumbersome to work with. Complex flow domains and need for fine grid sizes could affect the computational time for the flow solver. Also, various studies are needed to study the numerical dissipation and effort is required to control this dissipation.

Thus, a BEM based solver would effectively help to solve this problem. Issues such as grid size and meshing the domain do not arise because BEM requires only the boundary of the domain to be meshed. Also, once we solve for the unknown potential over the boundary, it is easy to evaluate the properties in the field as just summation of the solved values on the domain. Since BEM formulation is based on the assumption that the flow is inviscid and a line vortex representation is used, it would not be required to deal with issues such as vorticity dissipation.

Our main goal here is to model, study and understand the effect of tip vortices on a rudder. Several observations and experiments have shown that in reality these

vortices do not dissipate much and manage to maintain the core geometry through the extent of time when these vortices travel over the rudder. Hence, a BEM based formulation is used to model line vortex/hydrofoil interactions.

In the first section, the results are shown for a line vortex/hydrofoil interaction including the pressure distribution on the hydrofoil. In the next section, convergence studies done, with respect to the hydrofoil discretizations are presented.

5.1 Line Vortex/Hydrofoil interactions using PROPCAV, a BEM solver

It is easier to solve the vortex/hydrofoil interaction problem using a BEM solver as the effect of the vortex on the hydrofoil is seen in terms of the change in the inflow to the hydrofoil. This only changes the right hand side of the matrix system, i.e the source strengths and then solves for the potential on the hydrofoil. Once the potential and the velocities on the foil surface are known, the total velocity at the vortex locations is evaluated to convect the vortex in time. This total velocity includes the uniform inflow and the velocity induced by the hydrofoil and its wake.

The domain for the vortex/hydrofoil interaction model is shown in Fig. 5.1. The hydrofoil is shown with the line vortex at the initial position and after some time. A numerical limit is defined around the hydrofoil in order to prevent the vortex penetrating the hydrofoil. This happens because the velocities induced in the field by the hydrofoil very close to the foil panels are not accurate. This arises due to the constant distribution of sources and dipoles on the foil panels. The numerical limit L_T is a specified distance vertical to the hydrofoil panels as shown in Fig. 5.2.

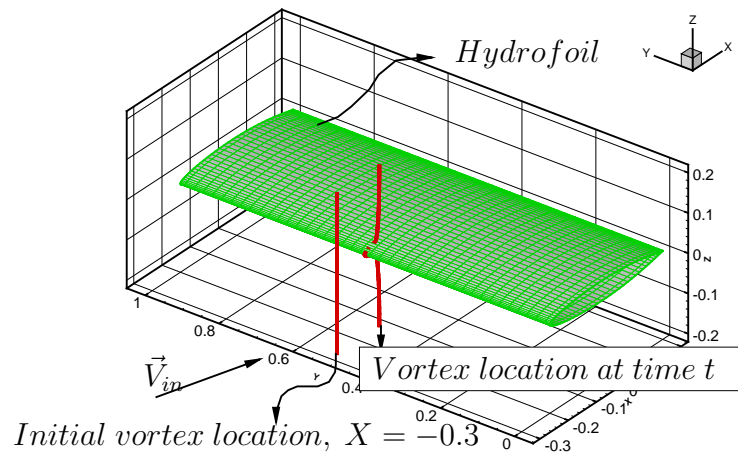


Figure 5.1: The domain for vortex/hydrofoil interaction model.

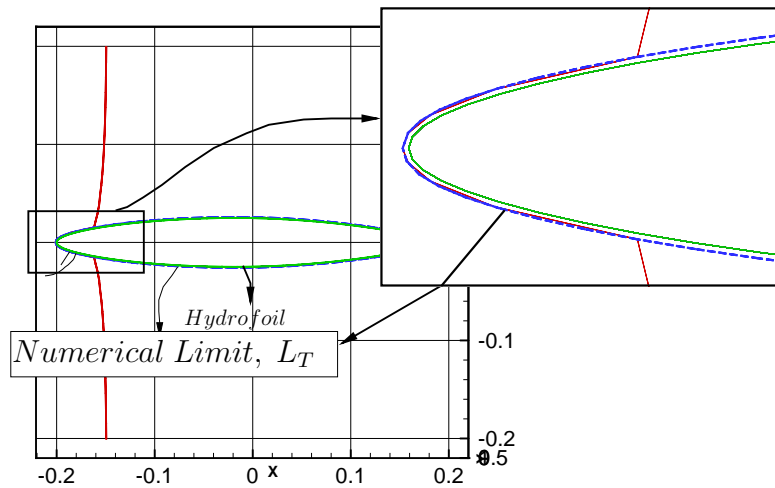


Figure 5.2: The numerical limit L_T defined around the hydrofoil.

The vortex movement towards the hydrofoil is shown in Fig. 5.3. The parameters for the results shown are as follows.

The hydrofoil is a *NACA66* hydrofoil section with the following dimensions. All the parameters shown are non dimensional. The distances are non dimensionalized using the span of the hydrofoil, $D = 1.0 \text{ m}$ and the velocities are non dimensionalized using the inflow velocity, $V_a = 1.0 \text{ m/s}$. The vortex strength is non dimensionalized as $\Gamma^* = \frac{\Gamma}{V_a D}$ and time as $t^* = \frac{t}{D/V_a}$.

- Chord length of the foil, $C^* = C/D = 0.4$
- Maximum thickness of the foil, $t_o^* = t_o/D = 0.05$
- foil discretization = 80×40 (chord \times span)
- Foil span length = $D^* = D/D = 1.0$
- Inflow velocity, $V_a^* = V_a/V_a = 1.0$

The line vortex is discretized into 80 vortex elements. The vortex strength, $\Gamma^* = 0.05$ and the numerical limit specified is $L_T^* = L_T/D = 0.001$. The non dimensional time step size, $\Delta T = 0.01$. The location of the line vortex through time is shown in Fig. 5.3.

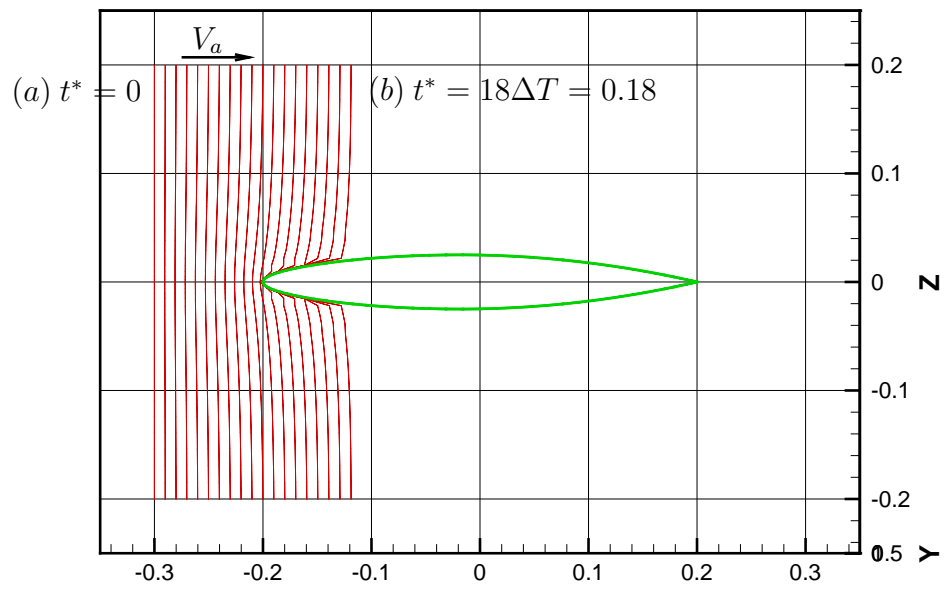


Figure 5.3: Vortex movement towards the hydrofoil at different times.

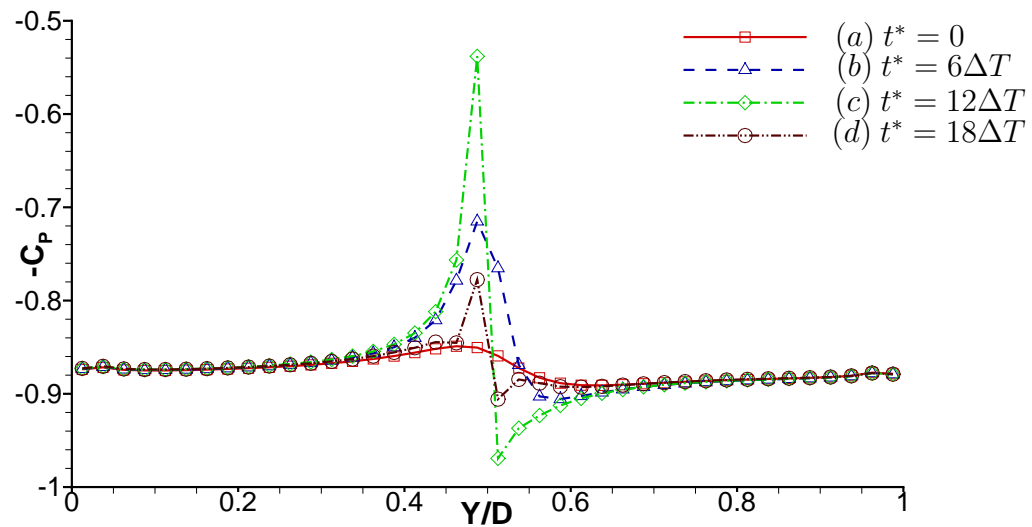


Figure 5.4: $-C_P$ along the leading edge of the foil at (a) $t^* = 0$, (b) $t^* = 6\Delta T$, (c) $t^* = 12\Delta T$ and (d) $t^* = 18\Delta T$. $\Delta T = 0.01$.

The distribution of C_P along the leading edge is shown in Fig. 5.4. From Fig. 5.4, it can be seen that the pressures on the foil surface drop as the vortex approaches the foil. The pressure is the lowest for $t^* = 12\Delta T$, as at that time, the vortex is the closest to the leading edge as seen in Fig. 5.3, when compared to $t^* = 18\Delta T$, where the least pressures on the foil surface occur in the areas in the vicinity of the vortex as shown in Fig. 5.4. The pressure contours on the hydrofoil due to the line vortex is shown in Fig. 5.5. The contour plots are shown with the corresponding vortex locations. It can be seen that the low pressures correspond to the areas on the hydrofoil in the vicinity of the vortex.

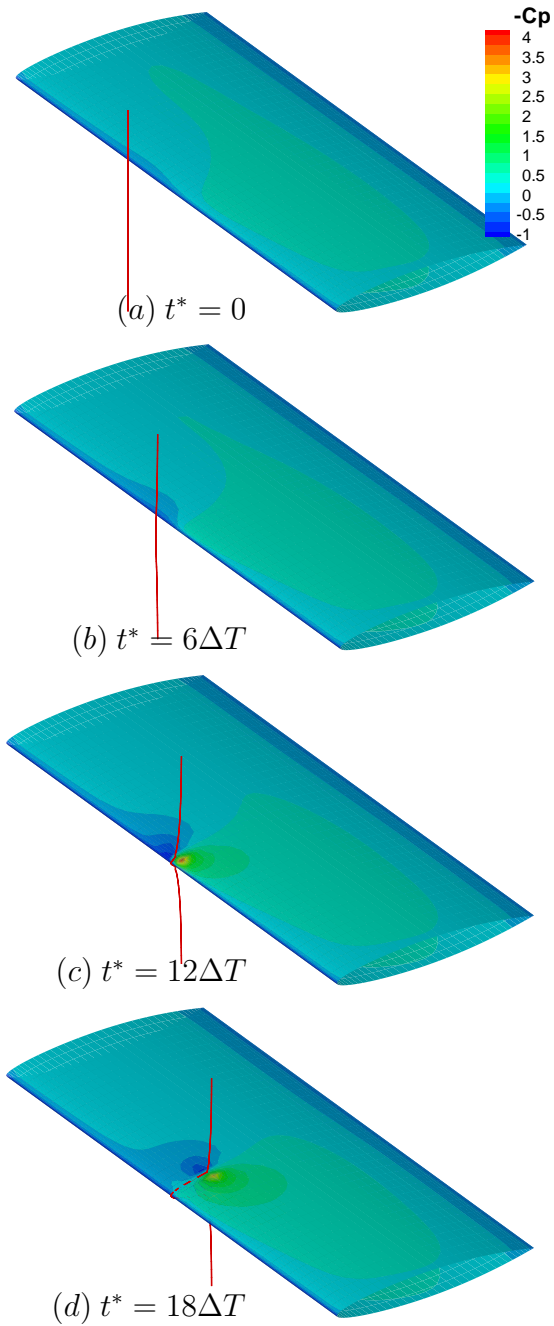


Figure 5.5: Contours of C_P at (a) $t^* = 0$, (b) $t^* = 6\Delta T$, (c) $t^* = 12\Delta T$ and (d) $t^* = 18\Delta T$. $\Delta T = 0.01$.

5.2 Convergence studies

It is important to understand the effect of the numerical limit L_T around the hydrofoil on the vortex/hydrofoil solution. The solution for vortex/hydrofoil interactions is obtained for different limits, from $L_T^* = 0.001$ to $L_T^* = 0.01$. Figure 5.6 shows the different vortex locations around the hydrofoil corresponding to the different numerical limits specified.

In Fig. 5.7, the pressure distribution along the leading edge of the foil is shown for different values of L_T at $t^* = 12\Delta T$ and $t^* = 18\Delta T$. As expected, low pressure values are noticed for the lower values of L_T . This happens because smaller values of L_T induce higher velocities due to the vortex on the foil control points. This increases the inflow to the hydrofoil and thus causes lower pressures.

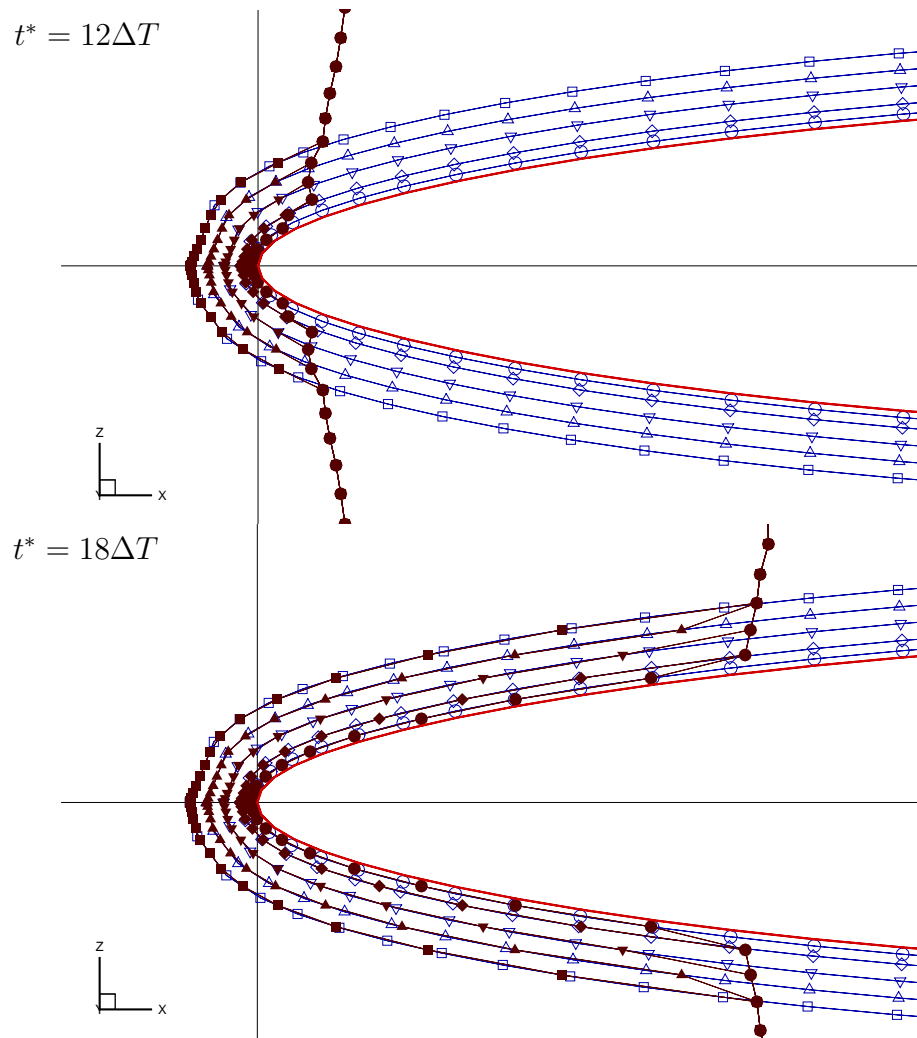


Figure 5.6: Vortex position around the hydrofoil for different limits at $t^* = 12\Delta T$ and $t^* = 18\Delta T$. $\Gamma^* = 0.05$ and $V_a^* = 1.0$.

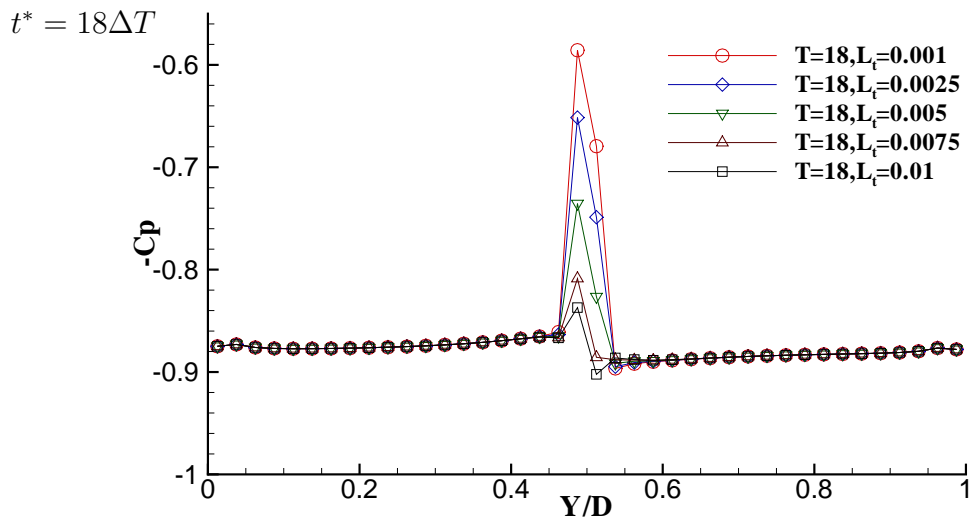
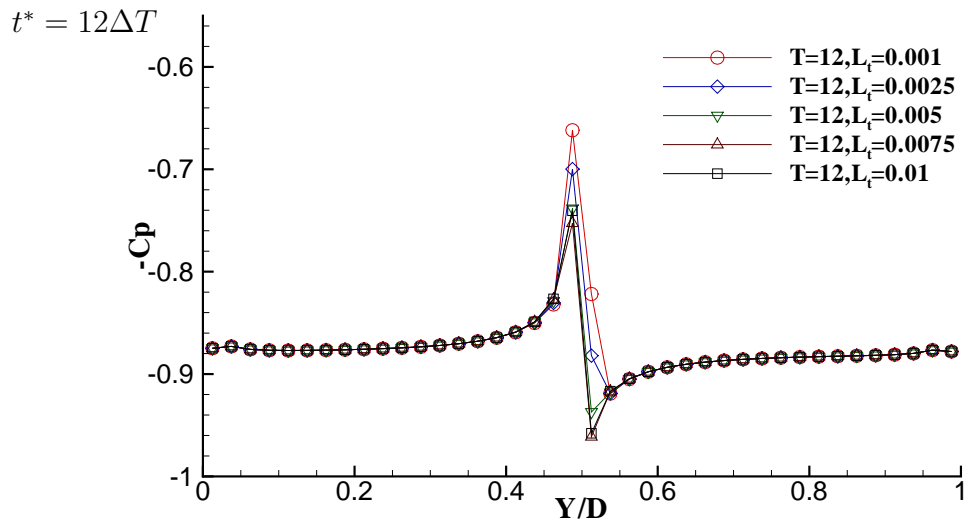


Figure 5.7: The pressure distribution on the leading edge at $t^* = 12\Delta T$ and $t^* = 18\Delta T$ for different values of the numerical limit L_T .

Convergence studies were next done for various hydrofoil surface discretizations. The hydrofoil surface was discretized into $N \times M$ panels, where N is the number of panels in the chordwise direction and M is the number of panels in the spanwise direction. Figure 5.8 shows the convergence of the pressure distribution on the leading edge of the foil at $t^* = 12\Delta T$ for different spanwise discretizations, $M = 10$ to $M = 80$. The chordwise number of panels are fixed at $N = 80$.

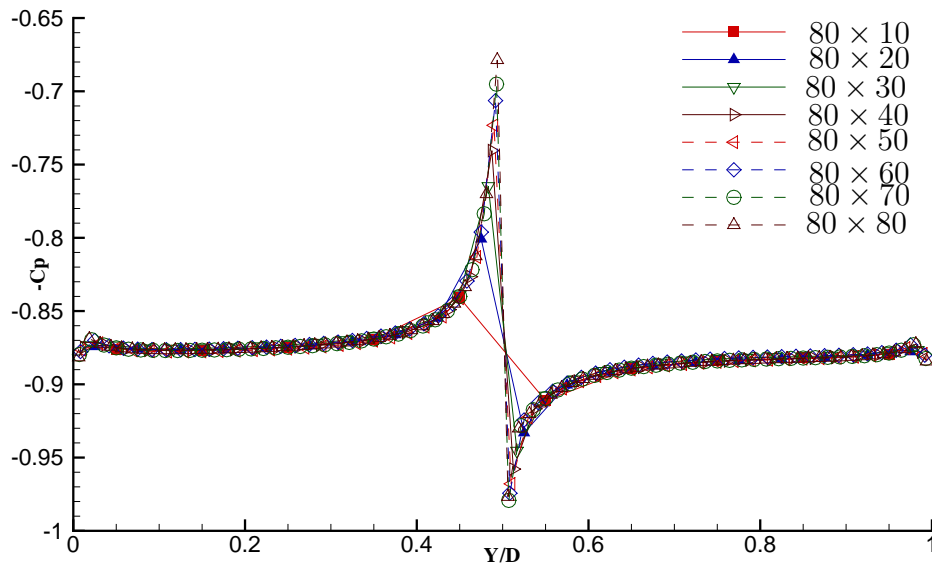
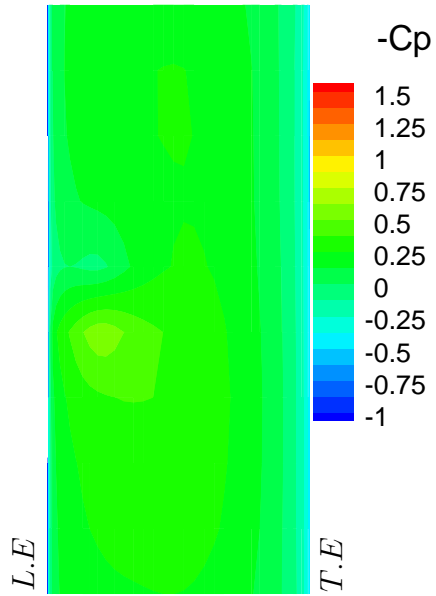


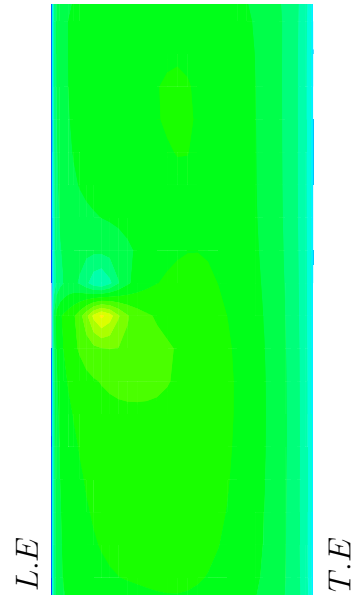
Figure 5.8: Convergence of leading edge pressure for the foil discretization shown in figure legend at $t^* = 12\Delta T$.

The convergence of the pressure distribution on the hydrofoil surface is also shown in the contour plots of $-C_P$ for different M and $N = 80$, shown in Fig. 5.9 at time $t^* = 18\Delta T$.

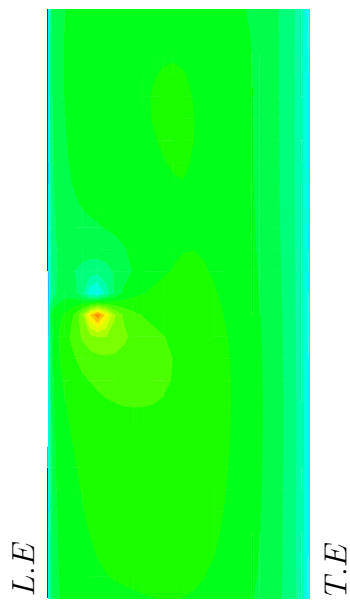
(a) 80×10



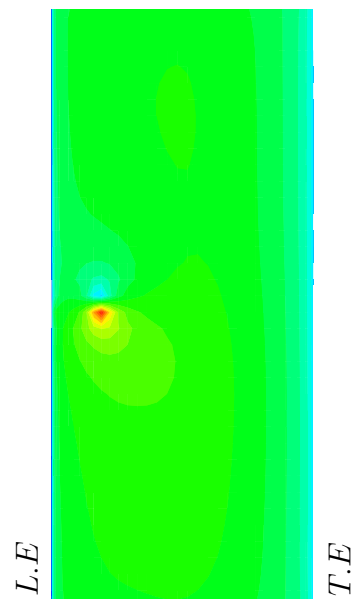
(b) 80×20



(c) 80×30



(d) 80×40



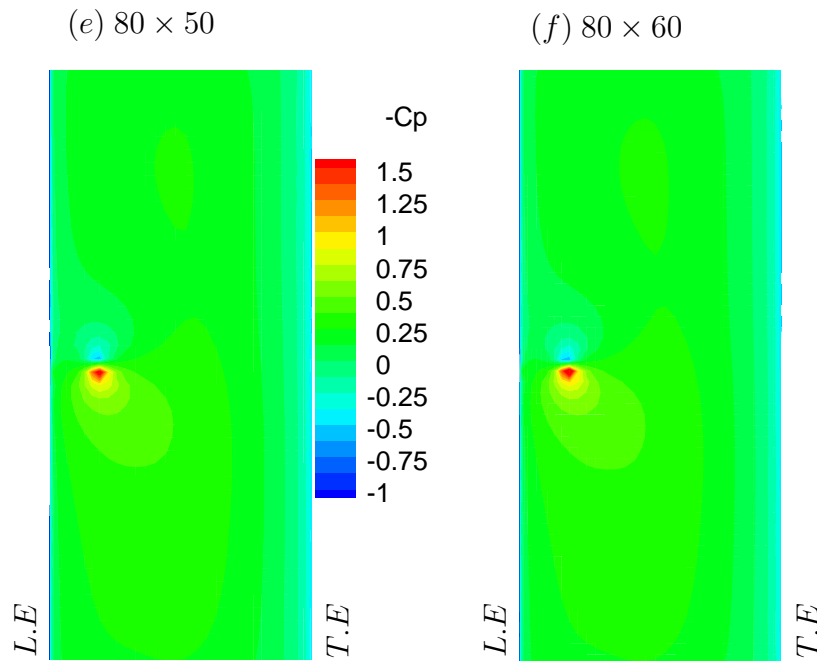


Figure 5.9: Pressure contours shown on the foil at $t^* = 18\Delta T$ for different spanwise discretizations of the foil: (a) 80×10 , (b) 80×20 , (c) 80×30 , (d) 80×40 , (e) 80×50 and (f) 80×60 .

The convergence of the pressure distribution on the foil is shown through contour plots of $-C_P$ for different N and $M = 40$, as seen in Fig. 5.10 at time $t^* = 18\Delta T$. The vortex has a circulation $\Gamma^* = 0.05$ around it and the inflow velocity is $V_a^* = 1.0$.

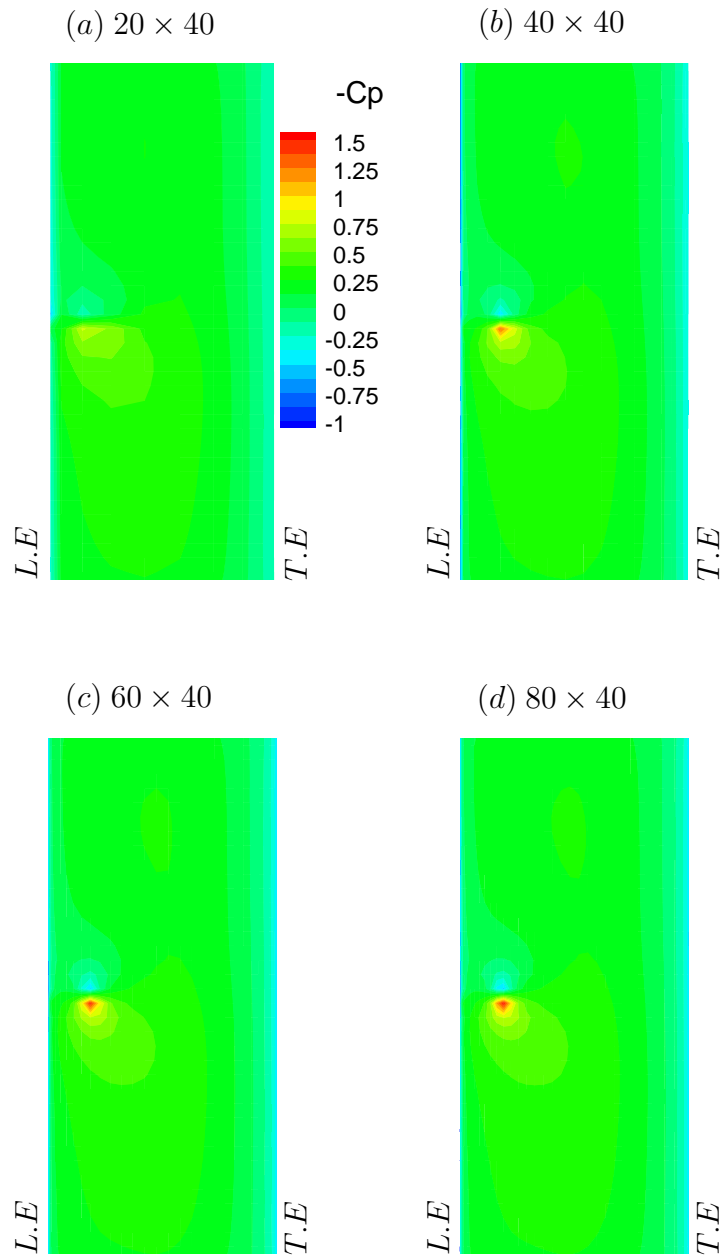


Figure 5.10: Pressure contours shown on the foil at $t^* = 18\Delta T$ for different chordwise discretizations of the foil: (a) 20×40 , (b) 40×40 , (c) 60×40 and (d) 80×40 .

Chapter 6

Lifting Line Wake alignment

In this chapter, a tip vortex is modelled using a lifting line model for propeller flows. The limiting case of zero thickness of the propeller blade foil section and vanishing chord length of the blade is a lifting line. A lifting line has a circulation distribution around it and this makes it easy to model flows related to propellers as the propeller blade is now approximated by a line vortex.

The alignment process is first applied to a closed vortex ring with a constant circulation around it. The results for a vortex ring are shown in the first section. In the second section, convergence studies for the vortex ring are presented. The results of the alignment procedure applied to the tip vortex wake of a lifting line is presented in the third section. In the last section, convergence studies related to the alignment process are presented.

6.1 Alignment results for a vortex ring

A vortex ring is a closed line vortex loop with a constant radius of curvature. For this study, the vortex ring has a constant value of circulation around it. The vortex ring system in a three dimensional space is shown in Fig. 6.1.

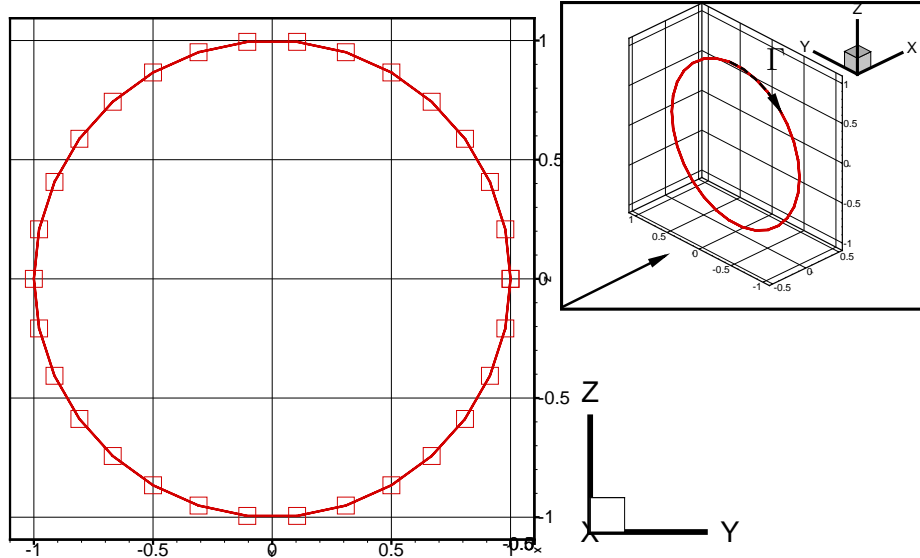


Figure 6.1: Discretized vortex ring with the direction of motion.

The axis of the ring is oriented in the x direction as shown in Fig. 6.1. The vortex ring is discretized using line vortex elements. The discretization is based on the angle subtended at the centre of the vortex ring by the vortex elements. Let the angular coordinate defining the vortex ring be θ and the discretized coordinate be $\Delta\theta$. Then the number of vortex elements, N on the vortex ring is given as

$$N = \frac{2\pi}{\Delta\theta} \quad (6.1)$$

The velocity induced by the vortex ring on itself is obtained by adding the velocity induced by the line vortex elements at each vertex of the vortex elements. Since the vortex ring has a constant circulation around it, the velocity induced at each vertex on the ring should be the same. This total induced velocity is in the axial direction of the vortex ring. Thus in the absence of any flow around the ring, the vortex ring convects in the axial direction with its own self induced velocity.

Here, the vortex ring is subjected to an axial velocity and hence, the vortex ring

moves with a total velocity which is the sum of the axial inflow and the self induced velocity of the vortex ring. An angular velocity $w = \pi \text{ rad/s}$ is defined and the corresponding time step is defined as $\Delta T = \frac{\Delta\theta}{\omega}$. The discretized angular coordinate is $\Delta\theta = 12^\circ$ and the vortex ring is discretized into $N = 30$ line vortex elements. The vortex ring experiences an axial inflow of $V_a = 1.0 \text{ m/s}$. The convection of the ring is shown in Fig. 6.2.

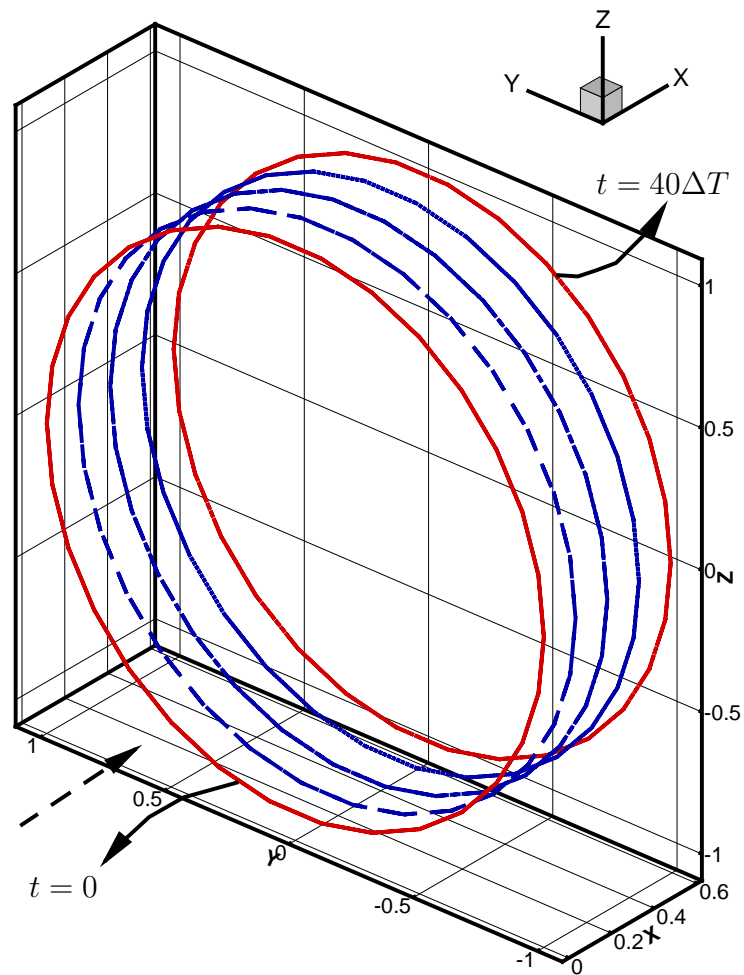
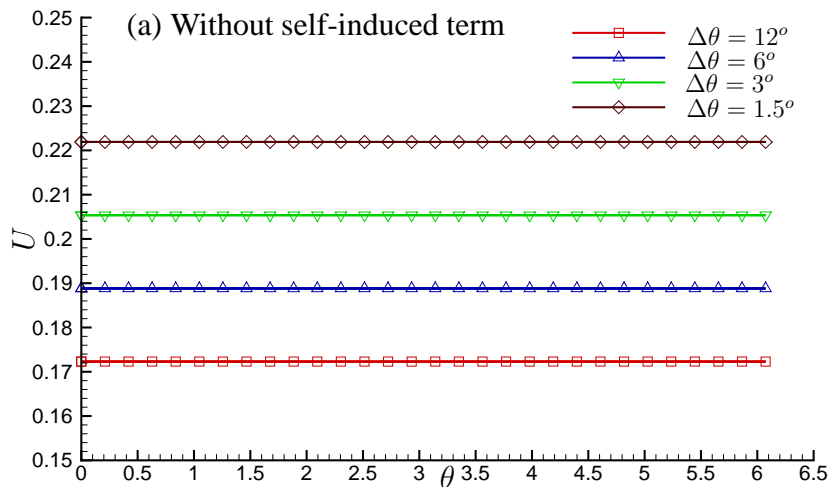


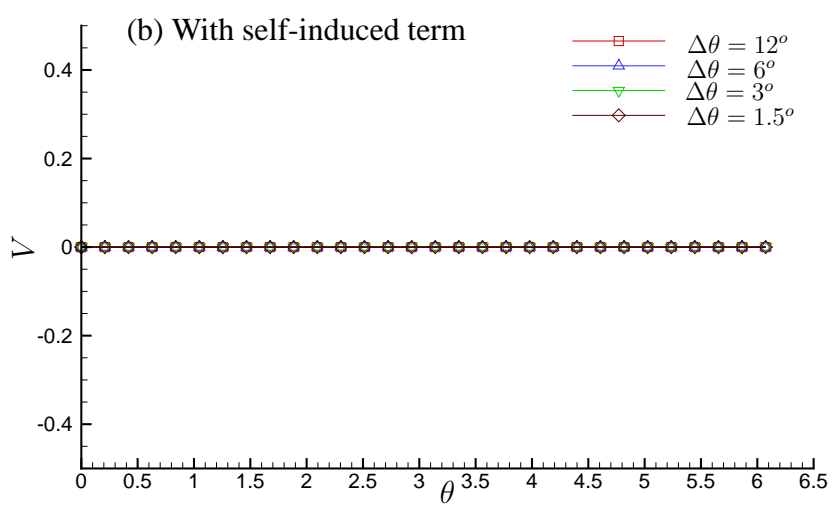
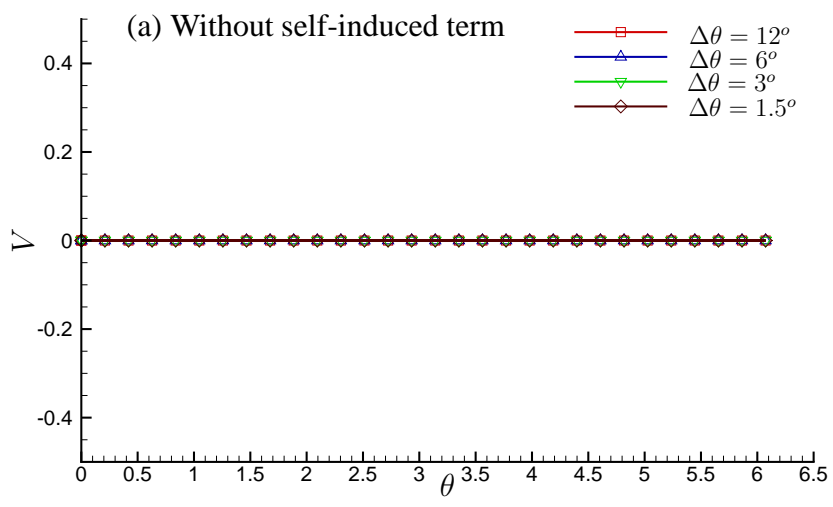
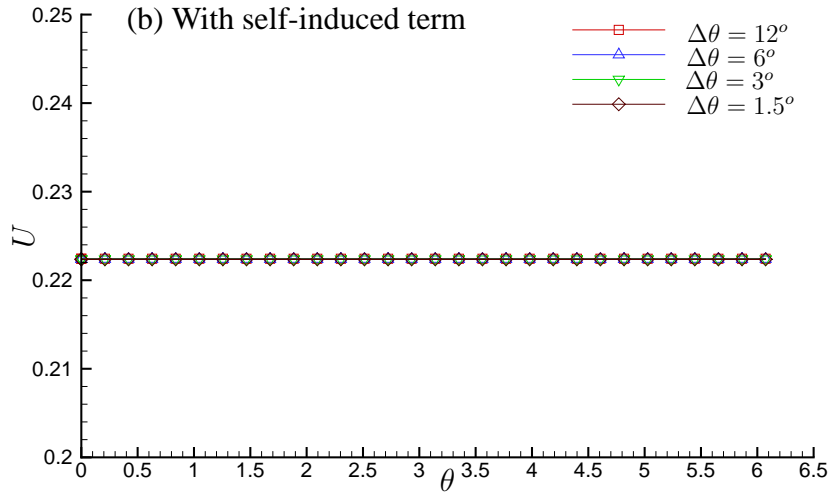
Figure 6.2: Convection of the vortex ring in the axial direction. The location of the ring is shown for every $10\Delta T$ from $t = 0$ to $t = 40\Delta T$.

6.2 Convergence studies on a vortex ring

At each of vertex of the vortex elements that make the vortex ring, the velocity is evaluated by summing up the velocity induced by all the line vortex elements in the ring using Eqn. 3.27. But Eqn. 3.27 cannot be used to evaluate the velocity induced by the two line vortex elements on either side of a vertex due to the singularity that arises when the field point is on the line vortex. The induced velocity on a vertex due to the line vortex elements on either side of it is evaluated using Eqn. 3.28.

Studies were done to evaluate the importance of including the self induced velocity on the vertices of the vortex ring by the line vortex elements supporting that vertex. In Fig. 6.3, the axial (X) velocity and the y and z velocities are shown for the different number of vortex elements on the vortex ring. Results are shown for $\Delta\theta = 12^\circ$, 6° , 3° , and 1.5° .





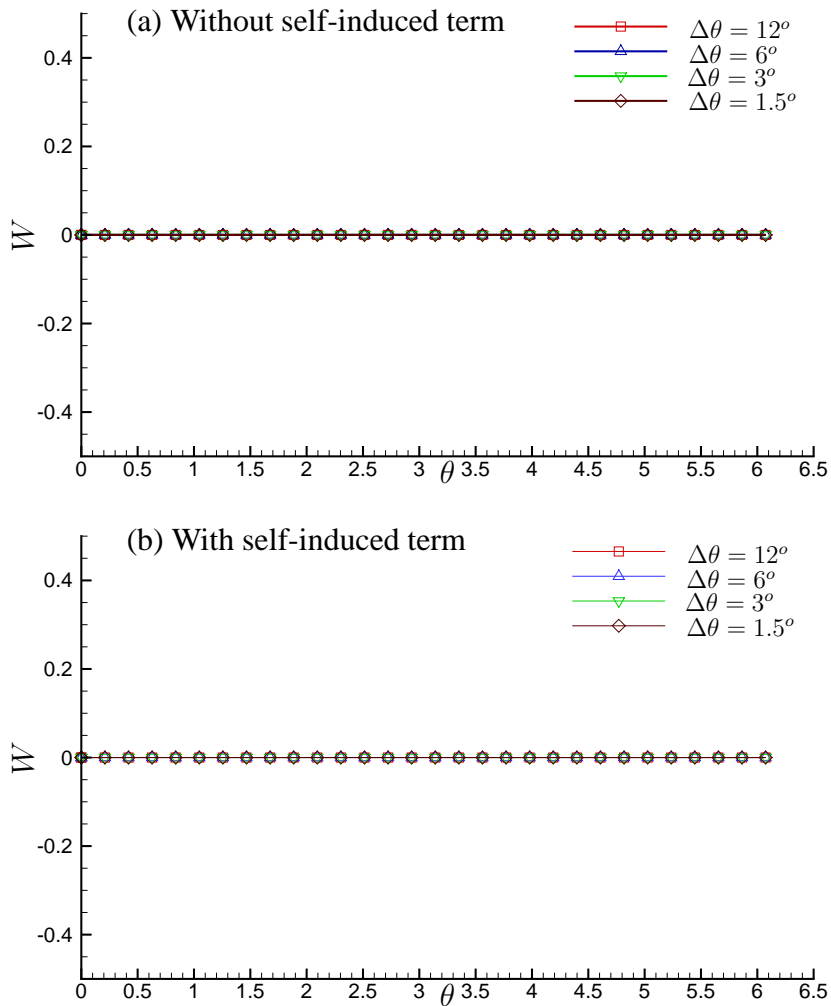


Figure 6.3: Induced velocity on the vortex ring (a) without and (b) with the self induced velocity of the vortex elements.

Thus, it can be seen from Fig. 6.3 that the induced axial velocity does not converge with the number of vortex elements on the vortex ring, N for the case where the self induced velocity of the vortex elements are not included. On the other hand, the convergence of the axial velocity with respect to N can be seen when the self induced velocity of the vortex elements is included. Also, as expected, the V and W velocities are zero for both cases.

6.3 Alignment Results for Lifting Line Tip Vortex

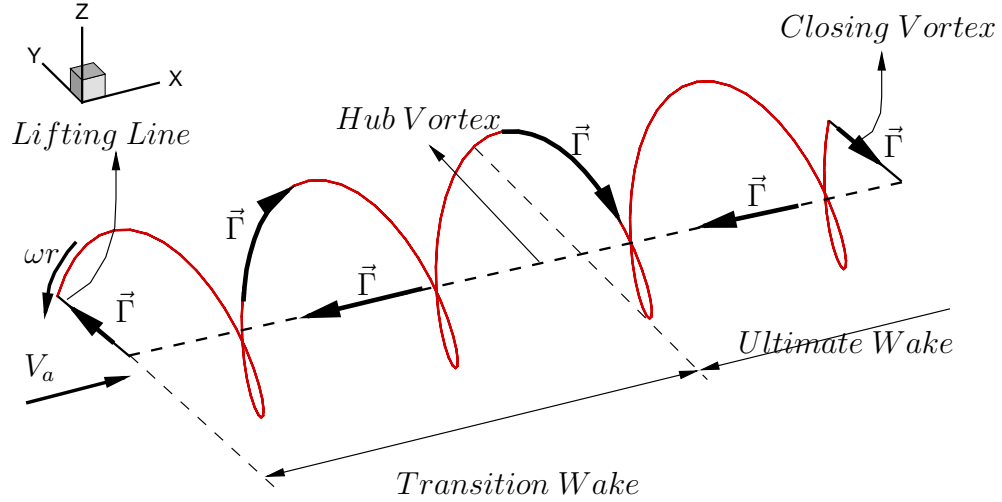


Figure 6.4: Lifting line system with the tip vortex wake.

The alignment technique, as given in Eqn. 3.49 is applied to the tip vortex wake of a lifting line. The lifting line system with the transition wake, which is aligned, the ultimate wake which is a constant pitch wake and the vortex closing segments is shown in Fig. 6.4.

Using Eqns. 3.27 and 3.28, the total velocity induced by the lifting line, the transition wake, the ultimate wake, the hub vortex and the closing lifting line, \vec{V}_{wk} is evaluated at each vertex of the transition wake. The inflow velocity \vec{V}_{in} is added to \vec{V}_{wk} to get the total velocity \vec{V}_{tot} with which the tip vortex wake is aligned. The tip vortex wake is aligned using Eqn. 3.49. The alignment results are shown below.

All the velocities are made non-dimensional by the axial inflow velocity $V_a = 1.0 \text{ m/s}$ and the distances and the coordinates are made non-dimensional by the radius of the lifting line, $R = 1.0 \text{ m}$. The vortex strength, Γ is non dimension-

alised as $\Gamma^* = \frac{\Gamma}{V_a R}$. All the parameters of the alignment process presented in the subsequent texts are non-dimensional.

The lifting line has a radius $R^* = 1.0$. The inflow velocity components are $V_a^* = 1.0$ and $V_t^* = \omega^* R = \pi$, with the angular velocity $\omega^* = \frac{\omega R}{V_a}$ and $\omega = \pi \text{ rad/s}$ corresponds to an advance coefficient, $J = \frac{V_a}{nD} = 1.0$, where $D = 2R$ and $\omega = 2\pi n$. The results are shown in Fig. 6.5 for a tip vortex wake with 4 transition wake revolutions and 20 ultimate wake revolutions. The discretized angular coordinate $\Delta\theta = 12^\circ$ and the number of vortex elements along the transition wake, $N = 4 \frac{360^\circ}{12^\circ} = 120$. The time step for the alignment procedure $\Delta T^* = \frac{\Delta\theta}{\omega^*}$. The lifting line vortex strength and the strength of the tip vortex wake is $\Gamma^* = 0.1$. Figure 6.5 shows the results for the alignment process. The initial wake and the aligned wake geometry is shown in the $x - y$ plane.

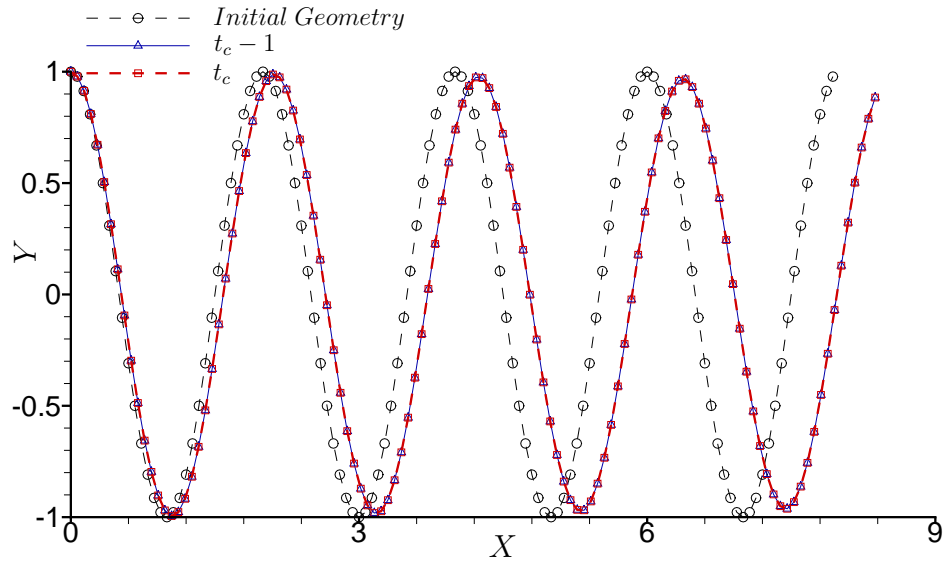


Figure 6.5: Initial wake geometry, aligned wake geometry at iteration step t_c and wake geometry at $t_c - 1$ is shown for $\Gamma^* = 0.1$.

Since the presence of a propeller accelerates the flow, the slipstream of the propeller contracts to account for the change in the control volume of the fluid. With relation to a lifting line system, this can be noticed as the contraction of the lifting line wake. In Fig. 6.5, this can be seen as the reduction in the radius of the aligned tip vortex wake.

Since the wake is aligned with the total flow field, the vector plot of the velocities along the wake should show the tangency between the velocity vectors and the directional vector of the wake elements at its vertices. The velocity vectors along the wake are shown in Fig. 6.6.

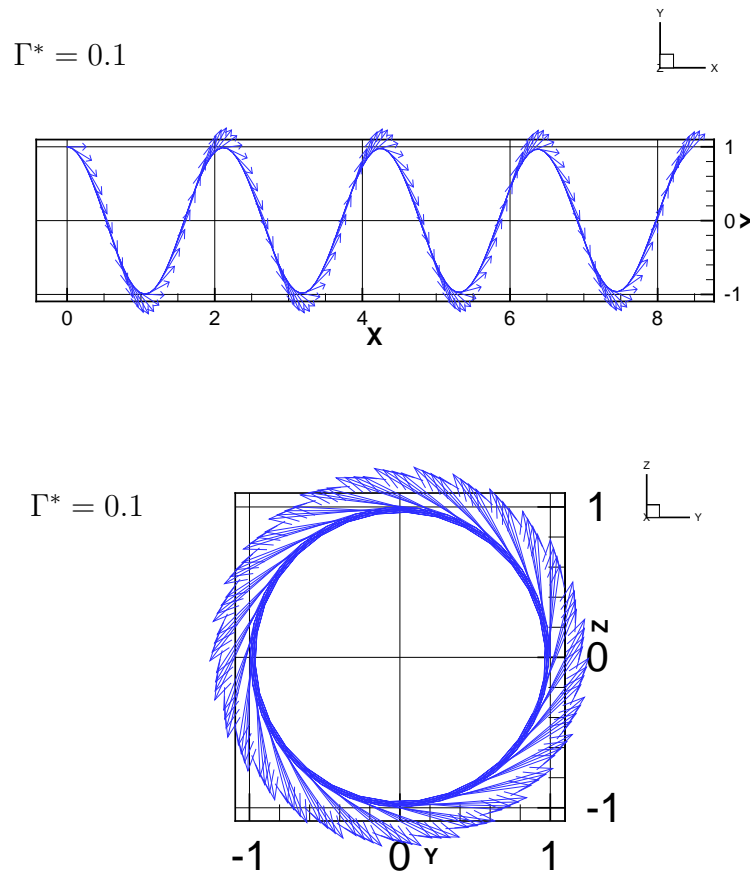


Figure 6.6: Velocity vectors along the aligned wake for $\Gamma^* = 0.1$ and $\Delta\theta = 12^\circ$.

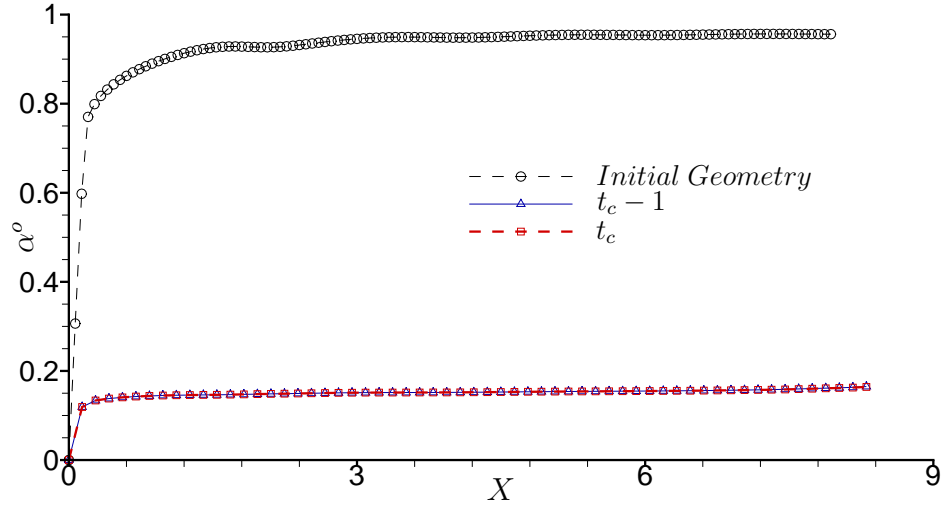


Figure 6.7: Angle α in degrees between the velocity vector \vec{V}_{tot} and the directional vector \vec{dr} along the aligned wake at the initial step, the converged iteration step t_c and $t_c - 1$ for $\Gamma^* = 0.1$ and $\Delta\theta = 12^\circ$.

The angle α between the velocity vectors and the vortex element directional vectors, in degrees, is shown in Fig. 6.7. For a converged wake geometry, α should be close to 0° to satisfy the force free condition on the tip vortex wake as given in Eqn. 3.41.

Figure 6.8 shows the error ΔX_{err} at the wake geometry. The L^2 norm of the error ΔX_{err} is shown along the iteration steps of the alignment process in Fig. 6.9. The convergence criteria for the alignment of the tip vortex wake is set as $L^2(\Delta X_{err}) \leq 1^{-4}$). It can be seen in Fig. 6.9 that the L^2 norm of the error ΔX_{err} has reached the convergence criteria and the iteration process stops. At this step, the tip vortex wake has been aligned. The proof of the alignment of the tip vortex wake with total velocity field can also be seen in Figs. 6.6 and 6.7.

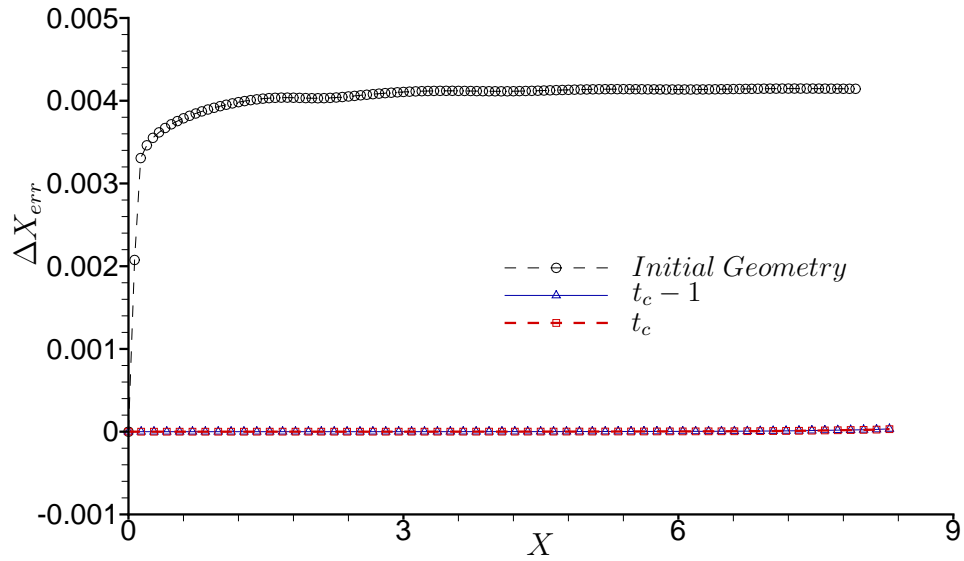


Figure 6.8: The error ΔX_{err} along the wake after the initial iteration step, the converged iteration step t_c and $t_c - 1$ for $\Gamma^* = 0.1$ and $\Delta\theta = 12^\circ$.

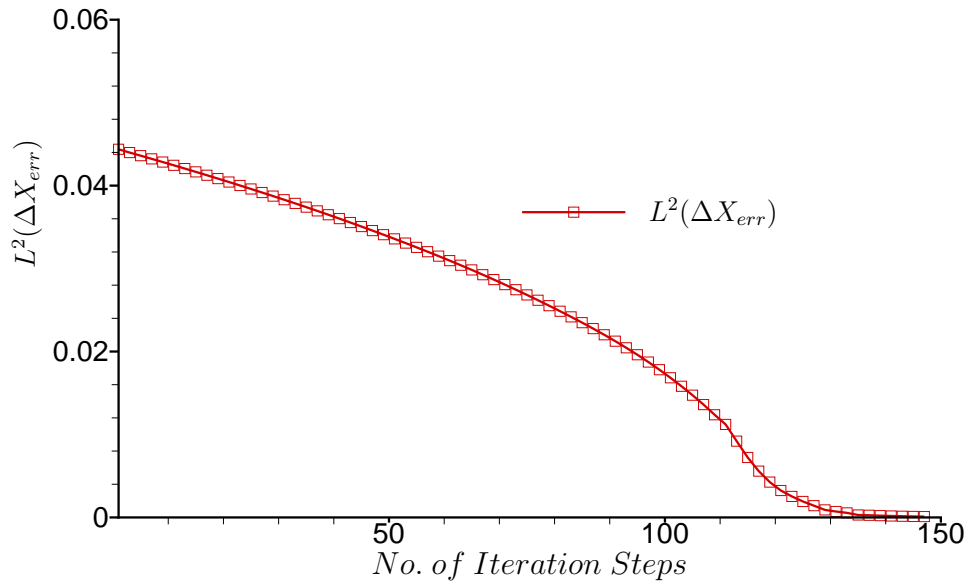


Figure 6.9: L^2 norm of the error ΔX_{err} at the iteration steps I for $\Gamma^* = 0.1$ and $\Delta\theta = 12^\circ$.

6.4 Convergence tests for helical wake

In this section, various convergence studies of the alignment process of the lifting line tip vortex wake are presented. The conditions for the alignment process is the same for all the results shown below. The radius of the lifting line is $R^* = 1.0$. The inflow to the lifting line is $V_a^* = 1.0$, $V_t^* = \pi$ and the angular velocity of the lifting line is $\omega^* = \pi$, corresponding to an advance coefficient, $J = \frac{V_a}{nD} = 1.0$. The vortex strength of the lifting line and all the components of its wake is $\Gamma^* = 0.1$.

Figure 6.10 shows the convergence of the aligned tip vortex wake with respect to the discretized angular coordinate, $\Delta\theta = 12^\circ, 6^\circ, 3^\circ$ and hence, with respect to the number of line vortex elements N present in the transition wake. The tip vortex geometry is initialized using 4 transition wake revolutions and 20 ultimate wake revolutions. The contraction of the aligned tip vortex wake can be seen for $\Delta\theta =$

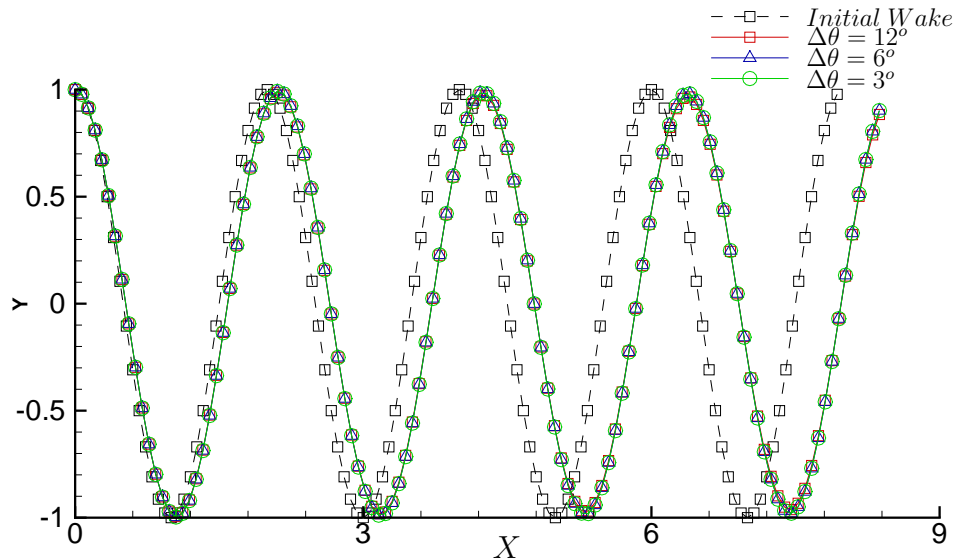
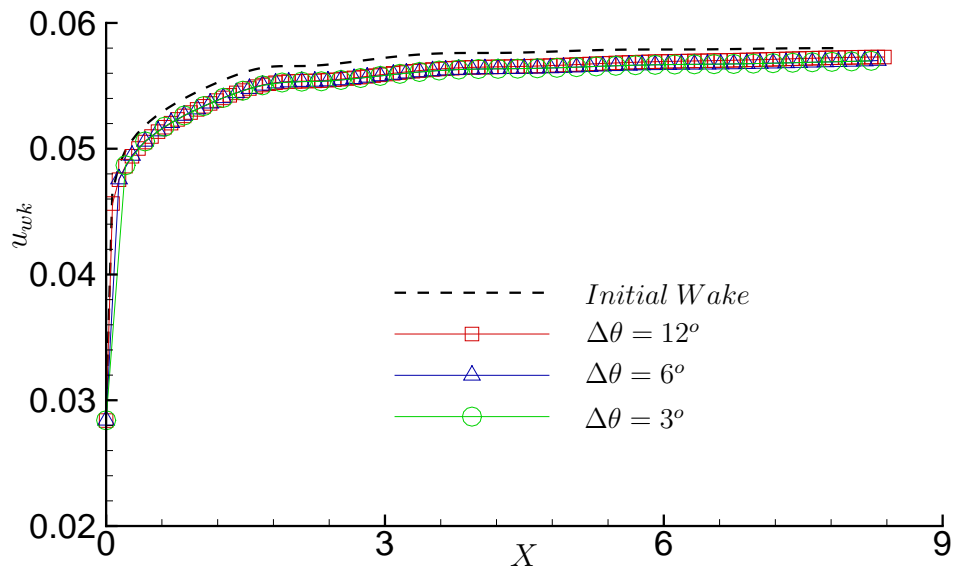


Figure 6.10: Convergence of aligned wake for $\Delta\theta = 12^\circ, 6^\circ$ and 3° . The vortex strength, $\Gamma^* = 0.1$ and $J = 1.0$.

12° , 6° and 3° . It can also be seen that the aligned tip vortex wake lie on the same geometry.

In Fig. 6.11, the induced velocities are shown along the tip vortex wake at the vertices of the wake elements for $\Delta\theta = 12^\circ$ and 3° .



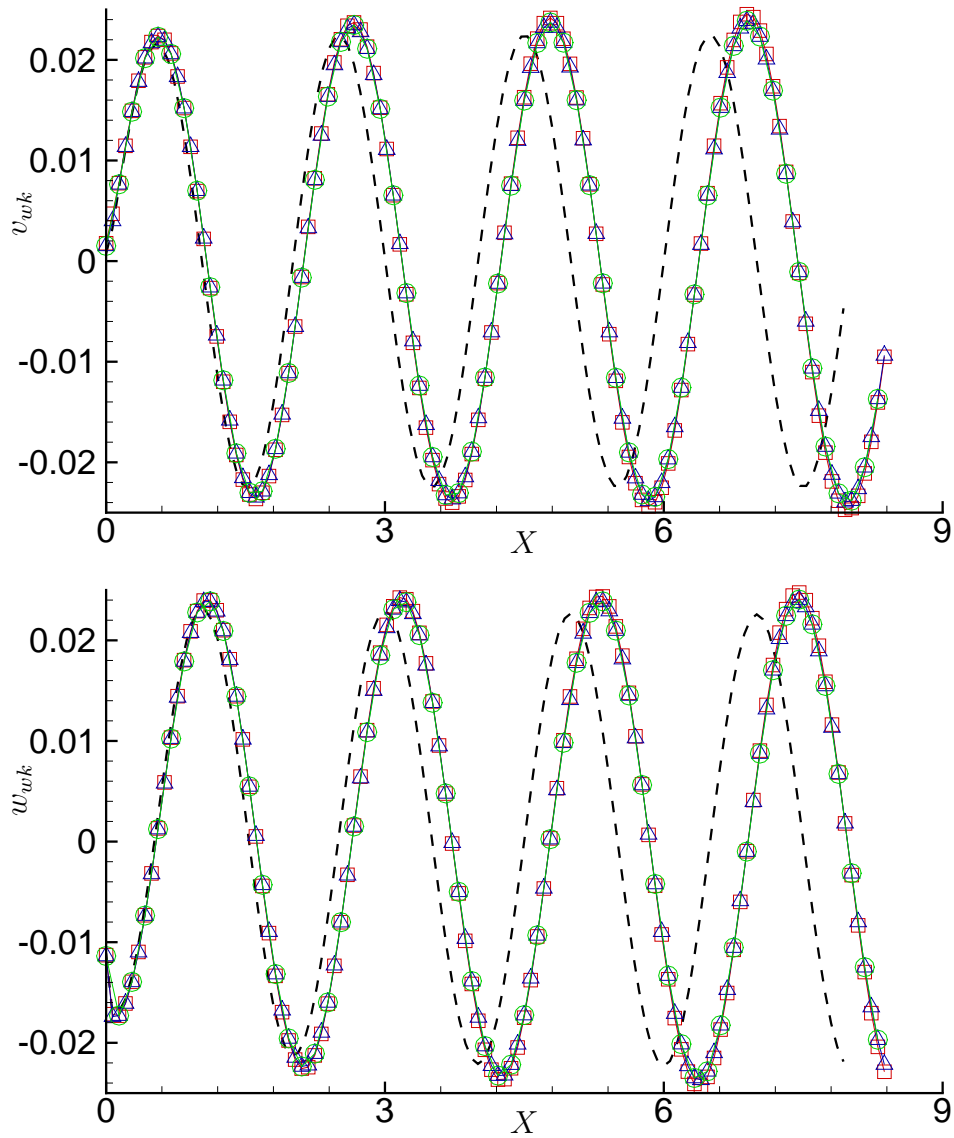


Figure 6.11: $(u, v, w)_{wk}$ along the tip vortex wake for $\Delta\theta = 12^\circ, 6^\circ$ and 3° . $\Gamma^* = 0.1$ and $J = 1.0$.

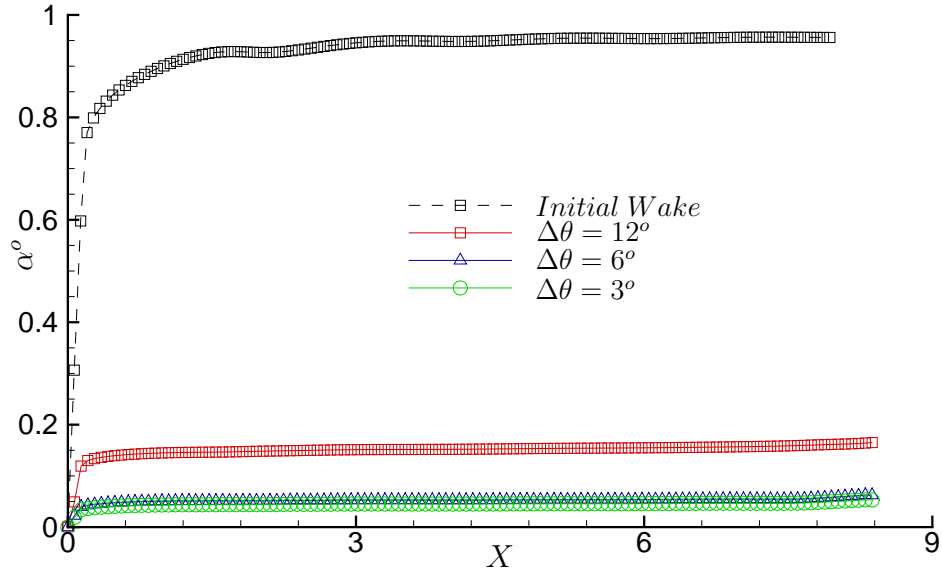


Figure 6.12: α along the tip vortex wake for $\Delta\theta = 12^\circ, 6^\circ$ and 3° . $\Gamma^* = 0.1$ and $J = 1.0$.

The convergence of the induced velocities along the aligned wake with $\Delta\theta$ can be seen in Fig. 6.11. The angle between the total velocity vectors and the directional vector, α at the vertices of the wake elements is shown in Fig. 6.12 for $\Delta\theta = 12^\circ, 6^\circ$ and 3° . It can be seen from Fig. 6.12 that α for the different discretized angular coordinate $\Delta\theta$ is close to 0° , thus showing that the velocity vectors are tangent to the directional vectors at the wake elements and hence, the tip vortex wake is force free.

For the same inflow, the tip vortex wake geometry is initialized with different pitch and the aligned wake geometry for different initial pitch is compared. The tip vortex wake geometry is initialised using half pitch, full pitch and twice the original pitch. The initial wake geometry is shown in Fig. 6.13. The initial tip vortex geometry for all the three cases of different pitch, P has 4 revolutions of the transition wake and 20 revolutions of the ultimate wake.

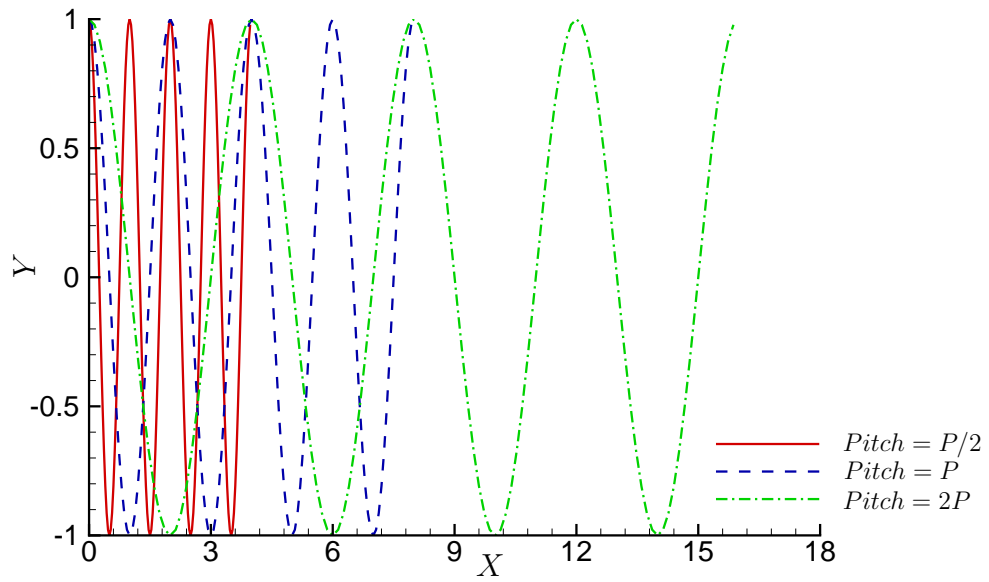


Figure 6.13: Initial tip vortex wake geometry for $0.5P$, P and $2P$, where P is the original pitch for the inflow conditions. $\Gamma^* = 0.1$, $J = 1.0$ and $\Delta\theta = 12^\circ$.

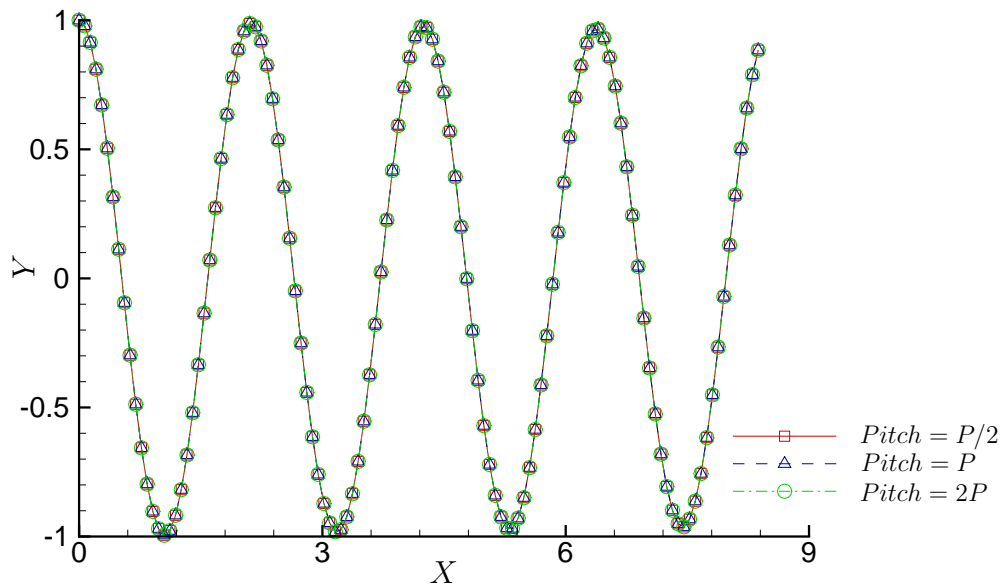


Figure 6.14: Aligned tip vortex wake geometry for initial pitch of $0.5P$, P and $2P$. $\Gamma^* = 0.1$, $J = 1.0$ and $\Delta\theta = 12^\circ$.

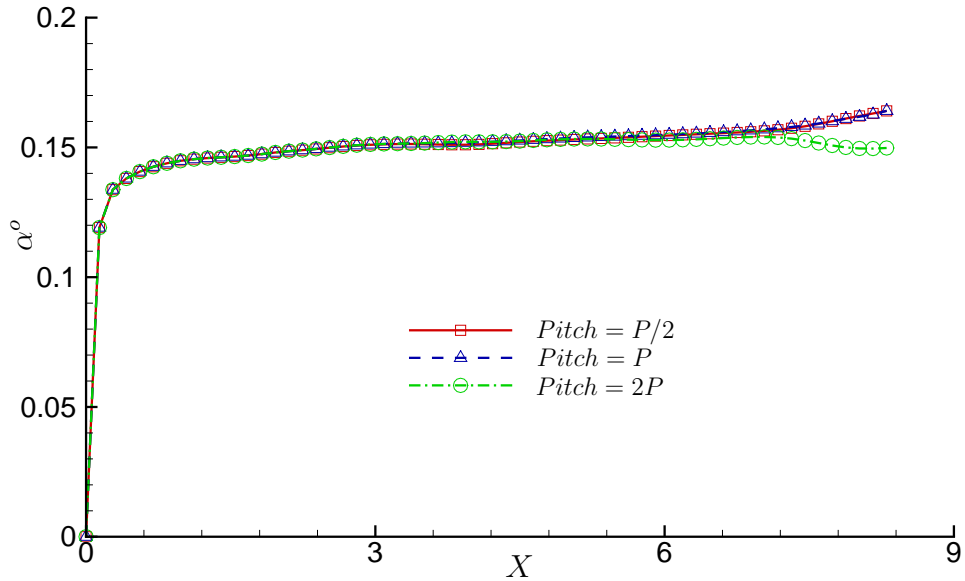


Figure 6.15: α along the aligned tip vortex wake geometry for initial pitch of $0.5P$, P and $2P$. $\Gamma^* = 0.1$, $J = 1.0$ and $\Delta\theta = 12^\circ$.

Figure 6.14 shows the convergence of the aligned wake geometry for each of the initial wake geometry. This is a good test that the alignment process works. Figure 6.15 shows the angle α between the velocity vector and the directional vector at the wake element vertices for the aligned wake, where the initial geometry of the wake was a constant pitch helix with pitch $0.5P$, P and $2P$. The pitch P corresponds to the actual inflow conditions.

From Figs. 6.14 and 6.15, it can be seen that irrespective of the initial pitch of the wake, for a given inflow condition, the tip vortex wake always aligns to the same final geometry. The aligned tip vortex wake geometry for the three different initial wake geometry all lie on the same aligned geometry. The contraction of the aligned tip vortex geometry can also be seen.

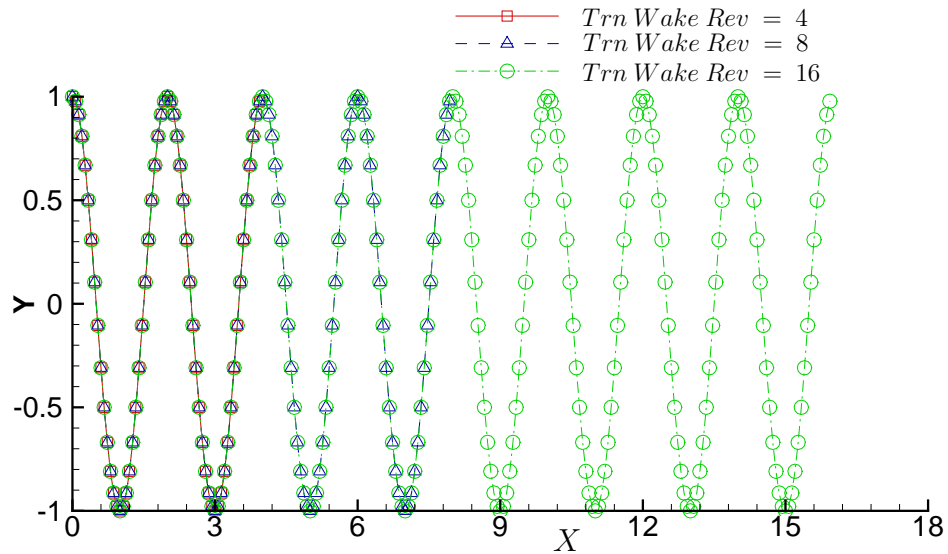


Figure 6.16: Initial wake geometry for 2, 4 and 8 revolutions of the transition wake. $\Gamma^* = 0.1$, $J = 1.0$ and $\Delta\theta = 12^\circ$.

The convergence of the aligned wake is also studied with respect to the number of transition wake revolutions. Irrespective of the number of revolutions of the transition wake, the aligned wake geometry should all be the same. The initial tip vortex wake geometry is shown for 2, 4, and 8 revolutions of the transition wake in Fig. 6.16. The number of revolutions for the ultimate wake is fixed at 20. Figure 6.17 shows the convergence of the aligned wake geometry with respect to the number of revolutions of the transition wake. The angle α along the aligned tip vortex wake is shown for the different revolutions of the transition wake in Fig. 6.18 It can be seen in Fig. 6.17 that the aligned tip vortex wake geometries for 2 and 4 revolutions of the transition wake lie on the geometry of the aligned tip vortex wake with 8 revolutions of the transition wake. This shows that the alignment procedure results in the same tip vortex wake geometry irrespective of the number of revolutions of the transition wake.

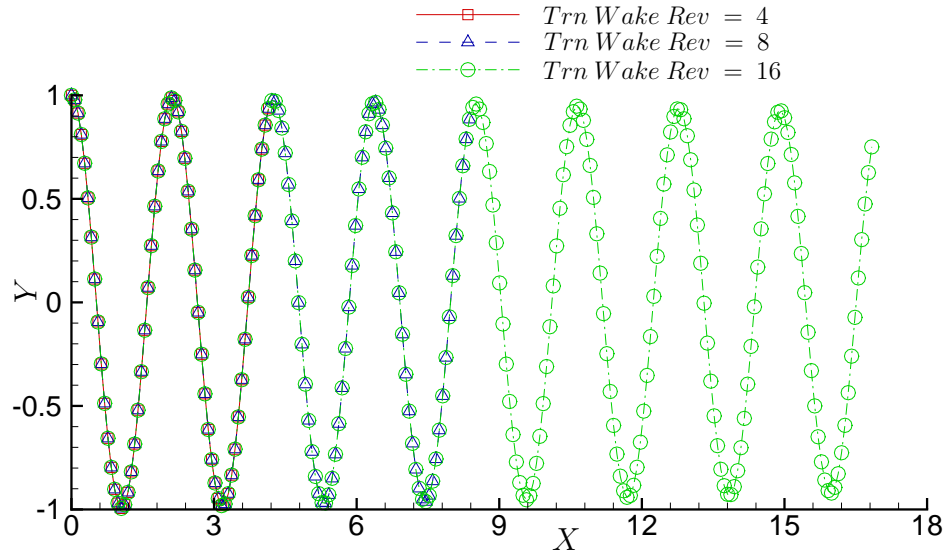


Figure 6.17: Convergence of aligned wake geometry for 2, 4 and 8 revolutions of the transition wake. $\Gamma^* = 0.1$, $J = 1.0$ and $\Delta\theta = 12^\circ$.

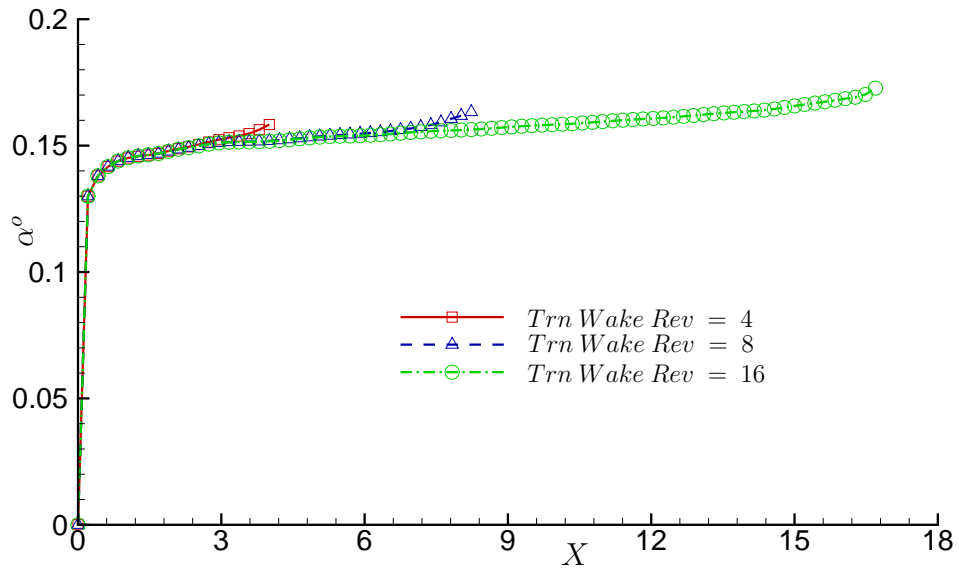


Figure 6.18: α along the aligned tip vortex wake for 2, 4 and 8 revolutions of the transition wake. $\Gamma^* = 0.1$, $J = 1.0$ and $\Delta\theta = 12^\circ$.

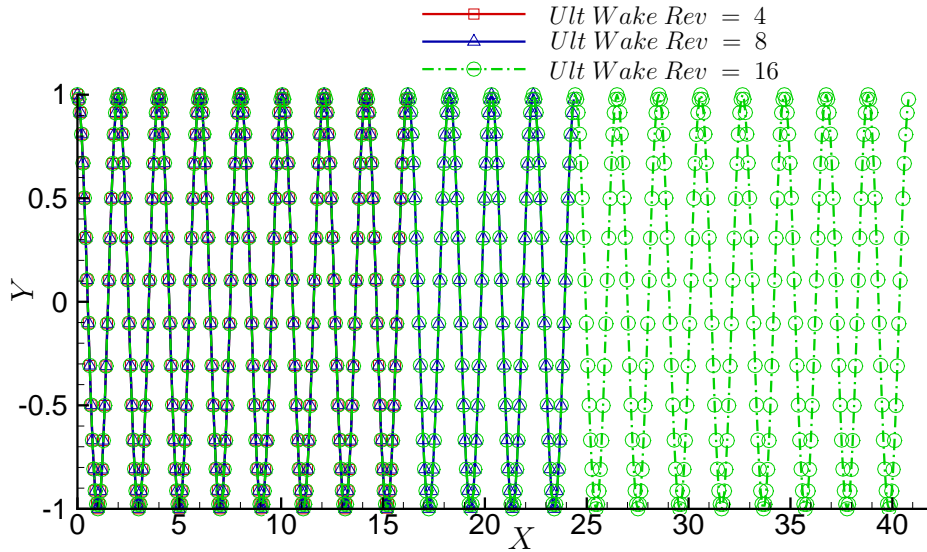


Figure 6.19: Initial wake geometry for 4, 8 and 16 revolutions of the ultimate wake. $\Gamma^* = 0.1$, $J = 1.0$ and $\Delta\theta = 12^\circ$.

Next, the convergence of the aligned wake is studied with respect to the number of ultimate wake revolutions. Different number of revolutions of the ultimate wake implies different ultimate wake lengths. The number of transition revolutions is fixed at 4 and the results are shown for 4, 8, and 16 revolutions of the ultimate wake.

The effect of the ultimate wake length on the alignment of the transition wake geometry is studied. The complete initial wake geometry is shown in Fig. 6.19 for 4, 8, and 16 revolutions of the ultimate wake. Figure 6.20 shows the convergence of the aligned wake geometry with respect to the number of revolutions of the ultimate wake. The angle α along the aligned tip vortex wake is shown for the different revolutions of the ultimate wake in Fig. 6.21

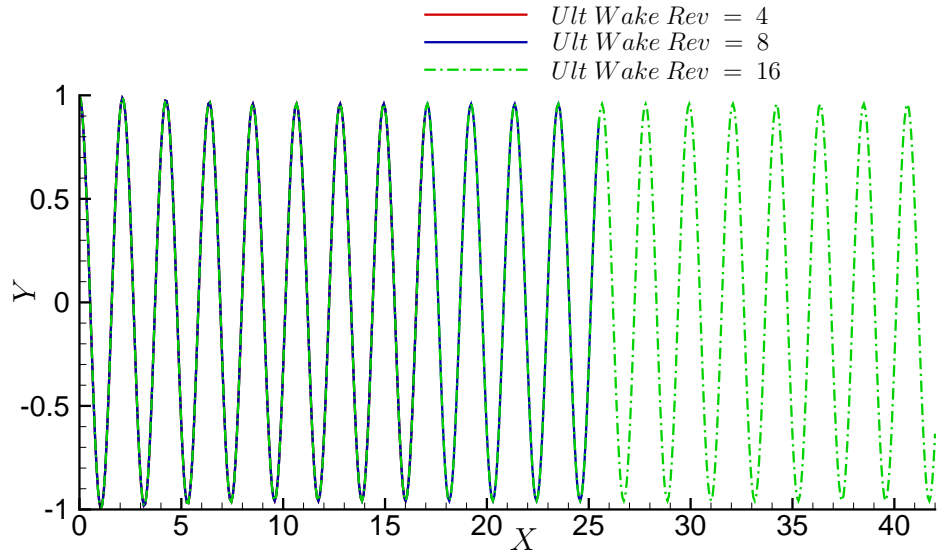


Figure 6.20: Convergence of aligned wake geometry for 4, 8 and 16 revolutions of the ultimate wake. $\Gamma^* = 0.1$, $J = 1.0$ and $\Delta\theta = 12^\circ$.

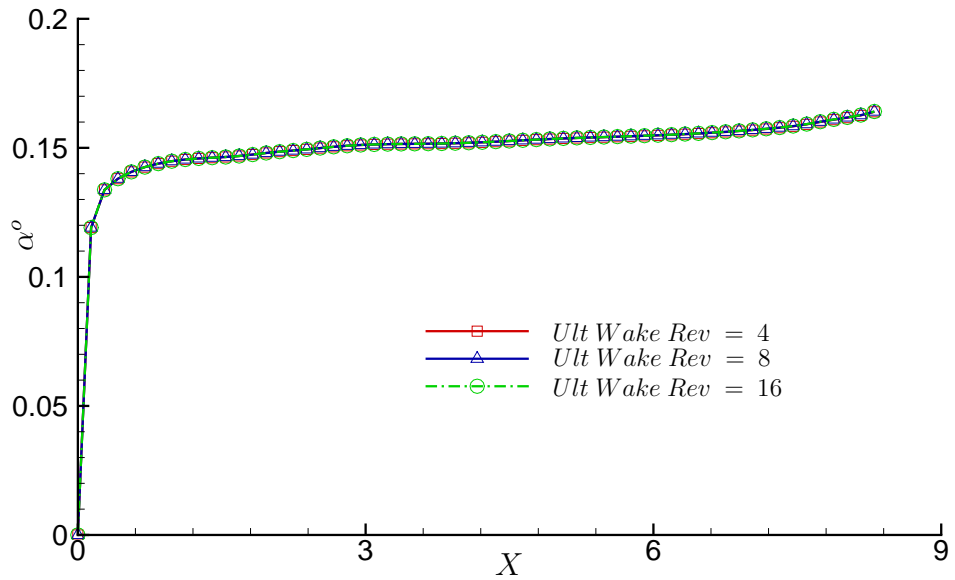


Figure 6.21: α along the aligned tip vortex wake for 4, 8 and 16 revolutions of the ultimate wake. $\Gamma^* = 0.1$, $J = 1.0$ and $\Delta\theta = 12^\circ$.

Chapter 7

Lifting Line Tip Vortex/Rudder interactions

The wake alignment routine is coupled with the line vortex/hydrofoil interaction model to simulate the interaction of propeller blade tip vortices and a rudder through the interaction of a lifting line tip vortex and a hydrofoil. The ease of modeling the line vortex/hydrofoil interactions as seen in Chapter 5 makes BEM a viable method to solve the interaction of a lifting line tip vortex wake with a hydrofoil.

In this chapter, results are shown in terms of the pressure distribution on the hydrofoil due to the lifting line tip vortex wake and convergence studies in terms of the lifting line wake discretization are presented.

7.1 Lifting Line tip vortex/hydrofoil interactions

The lifting line tip vortex system with the hydrofoil is shown in Fig. 7.1

The lifting line tip vortex wake is aligned with the total flow, \vec{V}_{tot} , which includes the inflow velocity, \vec{V}_{in} , the velocity induced by the lifting line system, \vec{V}_{wk} and the velocity induced by the foil and its wake \vec{V}_{rud} . At each iteration step of the alignment process, first the effect of the tip vortex wake is evaluated on the hydrofoil and then

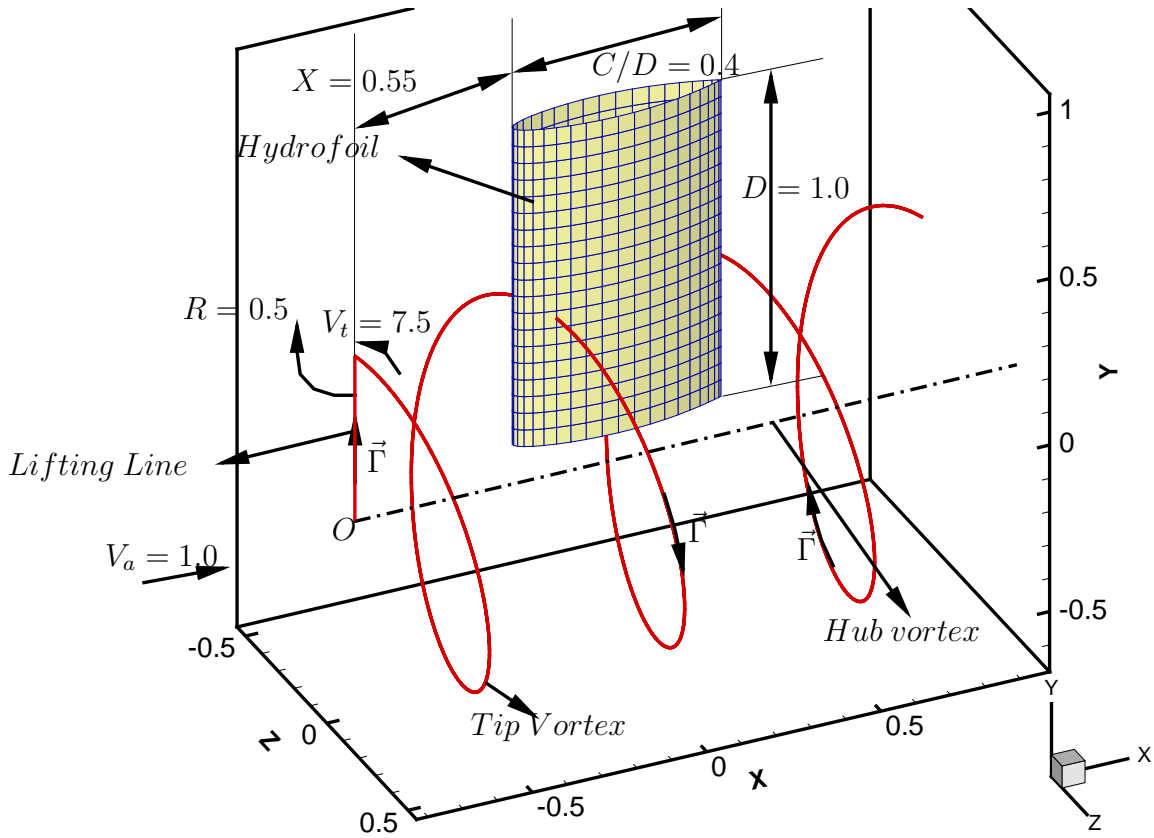


Figure 7.1: The lifting line tip vortex/hydrofoil interaction model.

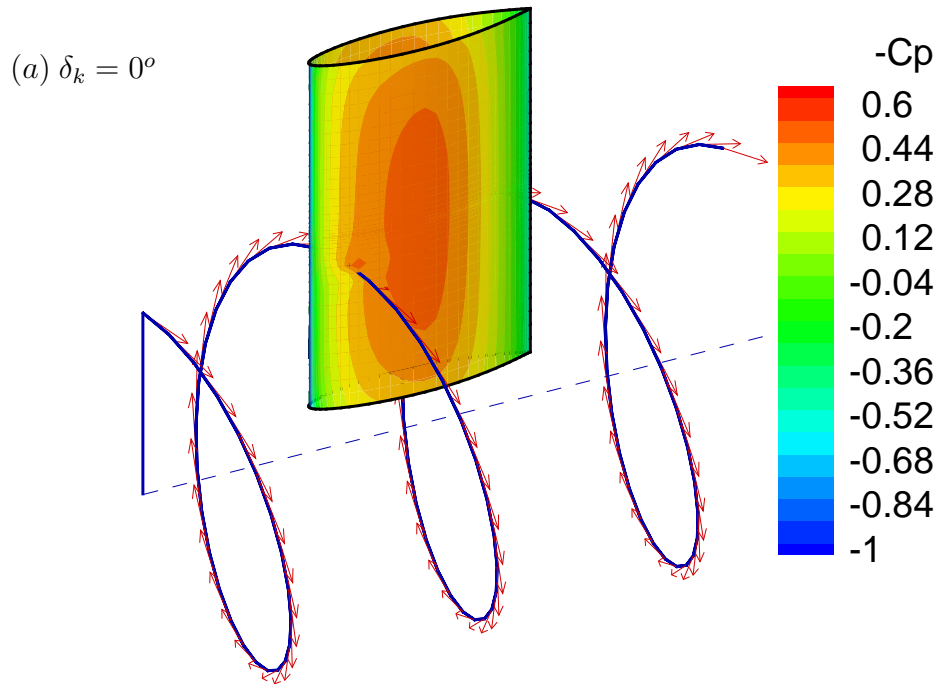
the total field velocity is obtained for the alignment process.

The parameters for the lifting line tip vortex/hydrofoil interaction model are shown below. All the distance variables are non dimensionalized using the hydrofoil span, $D = 1.0 \text{ m}$ and all the velocities are non dimensionalized using the axial inflow velocity, $V_a = 1.0 \text{ m/s}$. The vortex strength is non dimensionalized as $\Gamma^* = \frac{\Gamma}{V_a R}$, where R is the radius of the lifting line, $R = 0.5 \text{ m}$. The lifting line and the tip vortex wake system has the vortex strength, $\Gamma^* = 0.1$. The wake system has 3 revolutions of the transition wake and 3 revolutions of the ultimate wake. The results shown in Fig. 7.2 are for the tip vortex discretization of $\Delta\theta = 3^\circ$. The hydrofoil is a NACA66

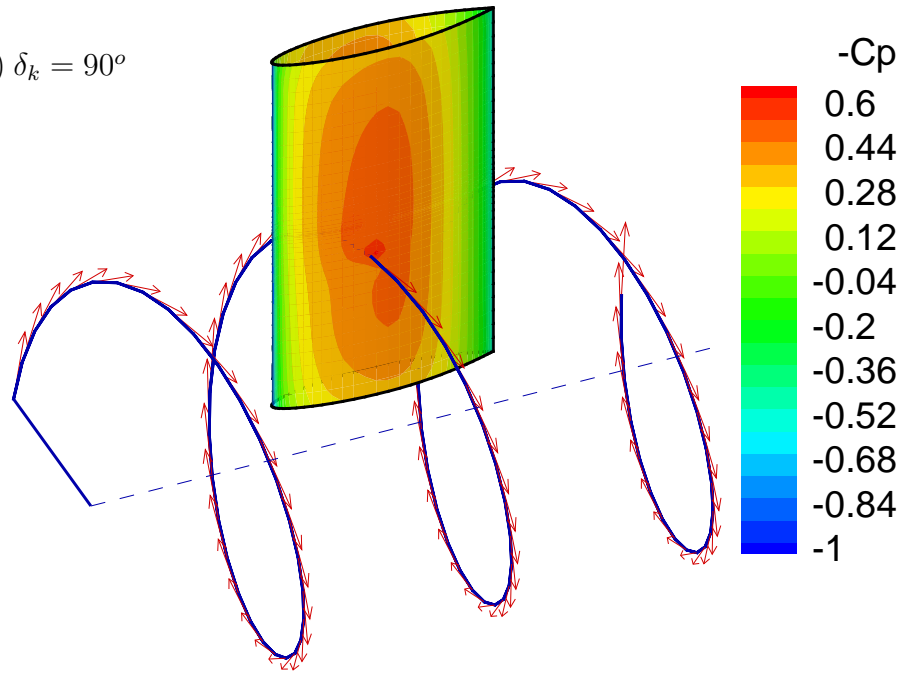
foil section with $D^* = 1.0$, $C^* = C/D = 0.4$ and maximum thickness of the foil section, $t_o^* = t_o/D = 0.12$. The hydrofoil is discretized using 40 panels in the chordwise direction and 20 panels in the spanwise direction.

In Fig. 7.2, the results are shown in terms of the pressure distribution on the hydrofoil and the velocity vectors on the aligned tip vortex wake geometry.

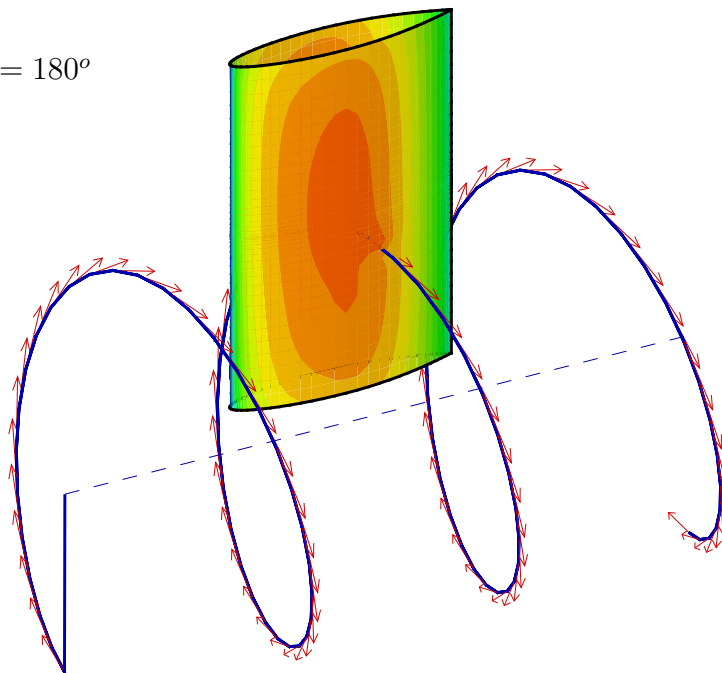
The vectors in Fig. 7.2 indicate that the velocity vectors are tangential to the directional vectors of the tip vortex wake, thus indicating that the wake is aligned to the total flow field. As seen earlier in the results of the lifting line/hydrofoil interactions, the tip vortex wake induces a low pressure on the foil in the vicinity of the tip vortex.



(b) $\delta_k = 90^\circ$



(c) $\delta_k = 180^\circ$



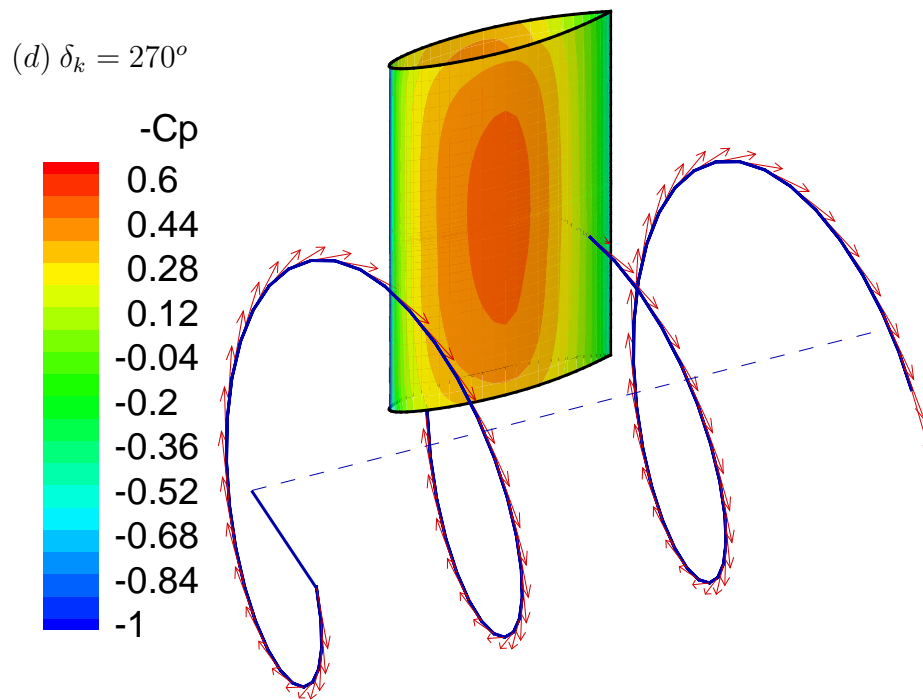


Figure 7.2: Contours of $-C_P$ on the foil for the lifting line location of (a) $\delta_k = 0^\circ$, (b) $\delta_k = 90^\circ$, (c) $\delta_k = 180^\circ$ and (d) $\delta_k = 270^\circ$.

When the effect of the tip vortex wake is evaluated on the hydrofoil, the portion of the tip vortex which passes through the hydrofoil is also included. However, for a real case, this portion inside the hydrofoil has to be neglected when the problem of the hydrofoil is solved.

Figure 7.3 shows the angle α in degrees along the tip vortex wake at the end of the alignment process.

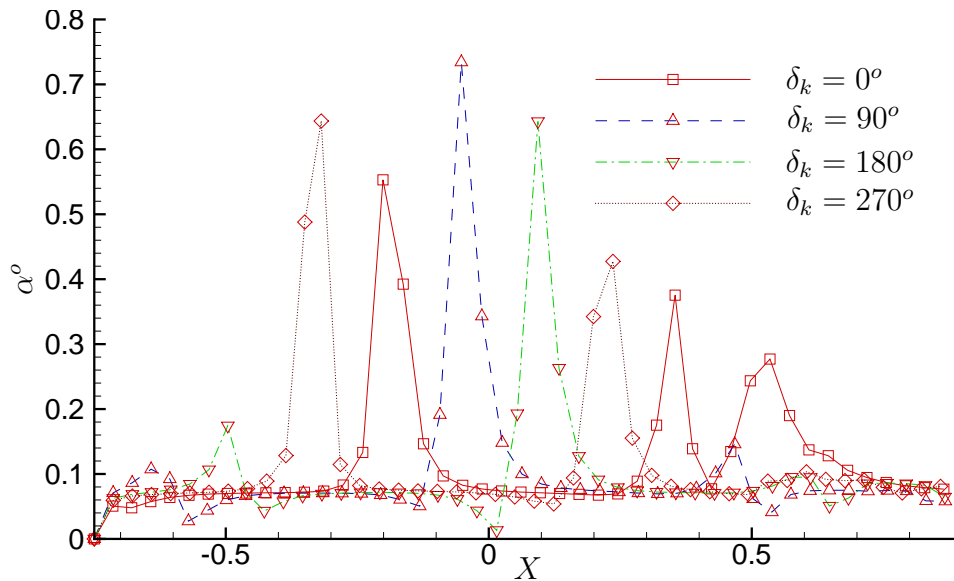


Figure 7.3: α° along the aligned tip vortex wake.

From the Fig. 7.3, we can see that the angle between the total velocity vector and the direction vector on the tip vortex wake is small. This confirms to the alignment of the tip vortex wake with the total velocity field. However, the spikes seen in Fig. 7.3 correspond to the location of the tip vortex when it is close to the foil. At those locations, the velocity induced by the foil is strong and this results in the large values of α compared to the rest of the tip vortex wake.

As the lifting line rotates, the minimum pressure coefficient at each location of the lifting line, on the hydrofoil is shown in Fig. 7.4

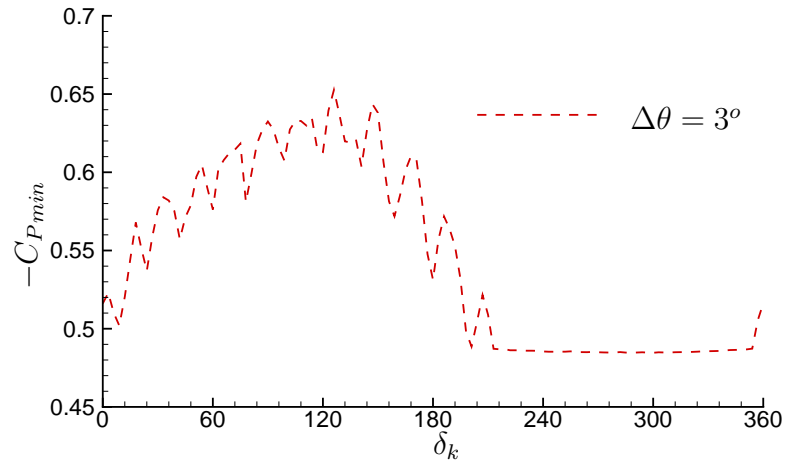


Figure 7.4: $-C_{P_{min}}$ on the foil surface at different lifting line angles.

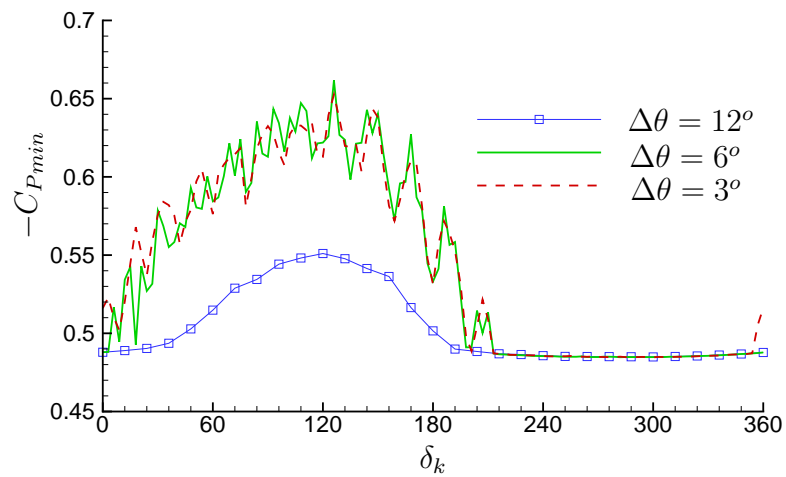


Figure 7.5: $-C_{P_{min}}$ along lifting line angle for $\Delta\theta = 12^\circ, 6^\circ,$ and 3° .

Through Fig. 7.4, we get an idea as to the possible location of the lifting line for the inception of cavitation on the hydrofoil. This measure can also be used to study the effect of the tip vortex wake discretization on $C_{P_{min}}$. Figure 7.5 shows the $C_{P_{min}}$ along the lifting line angle for $\Delta\theta = 12^\circ, 6^\circ, 3^\circ$. The oscillations seen in the values of $C_{P_{min}}$ along the lifting line angle could be due to the facet that when the problem for the hydrofoil is solved, the portion of the tip vortex wake inside the hydrofoil is also included. By neglecting this part, the oscillations may vanish.

The convergence of the aligned wake with the total flow field is shown in Fig. 7.6. This total velocity includes the inflow velocity, the lifting line tip vortex wake induced velocity and the velocity induced by the hydrofoil and its wake.

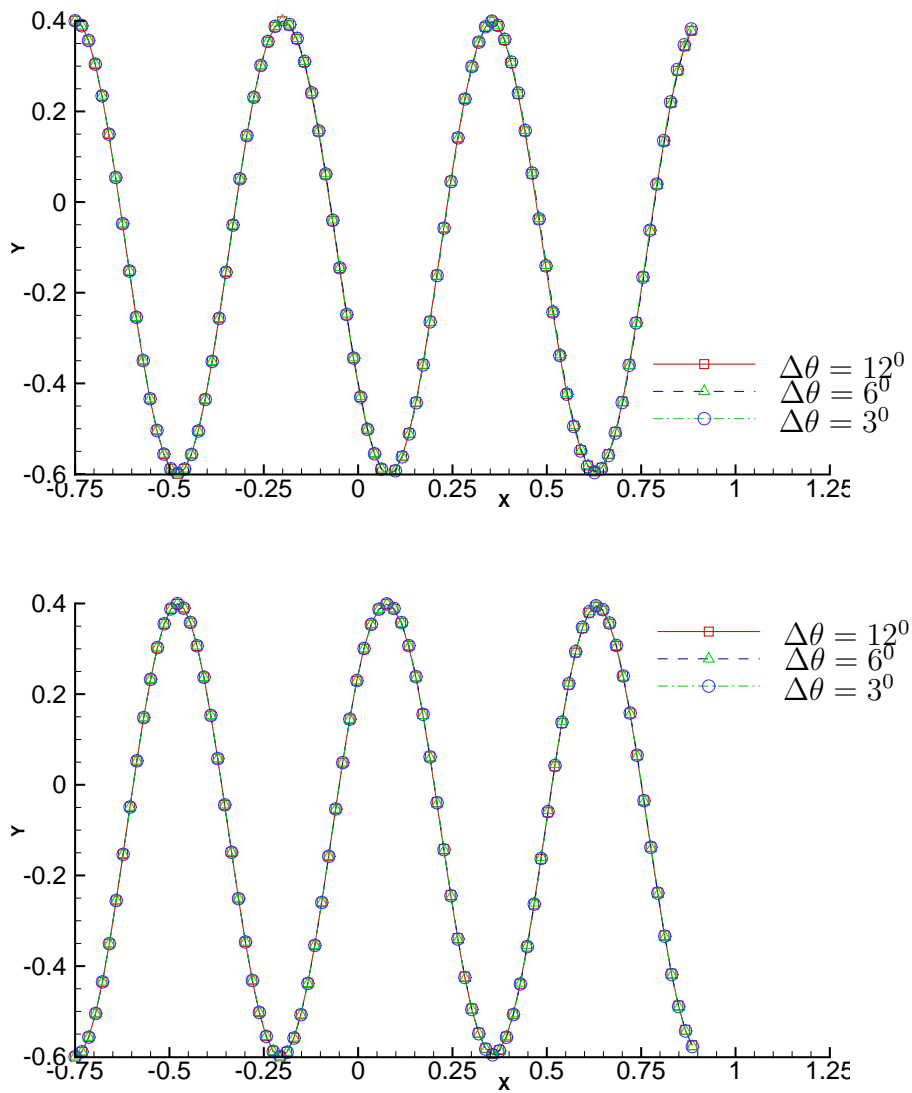


Figure 7.6: Convergence of the aligned tip vortex wake at (a) $\delta_k = 0^\circ$ and (b) $\delta_k = 180^\circ$ for $\Delta\theta = 12^\circ, 6^\circ,$ and 3° .

Chapter 8

Conclusions

8.1 Conclusions

Having a complete understanding of the dynamics of the flow around a rudder will help us to create accurate numerical models for rudder design and prediction of cavitation on a rudder. Of special interest is the interaction of the propeller blade tip vortices with the rudder. These cavitating vortices induce low pressure distribution on the rudder and could also give rise to acoustic noise and vibrations of the rudder and the hull. This work aims to understand the phenomenon of propeller blade tip vortex/rudder interaction and predict the pressure distribution on the rudder surface due to the tip vortices.

The vortex/hydrofoil interactions were initially modelled using a commercial CFD solver, FLUENT. The dynamics of a 2D vortex in a uniform flow were studied initially to understand the importance of the various modeling parameters such as grid size and the order of the time stepping scheme, etc. The 2D vortex in a uniform flow was found to be too dissipative in nature. Studies were done in order to control the dissipation of the vorticity over time. This was done because the numerical schemes in the CFD based solver FLUENT, has an inherent numerical dissipation and this makes it difficult to model problems of vortex flows. In 3D vortex/hydrofoil interac-

tions the dissipation of the vorticity is even more and by the time the vortex travels over the chord of the hydrofoil it has dissipated to a large extent. However as shown in Figs. 1.1 and 1.2, the tip vortices that travel over the rudder are tightly bound and do not dissipate much for the length of the rudder chord. Also, for a complete model of the propeller tip vortex rudder interaction, the entire domain, in which the propeller and the rudder is present, needs to be meshed. The size of the domain and the mesh size increases the computational time as well. Thus, CFD modeling in FLUENT makes it difficult to model the tip vortex rudder interaction and accurately capture the tip vortices and their effect on the pressure distribution on the rudder surface.

In BEM modeling, only the boundary of the domain need to be meshed. This makes it an attractive option to model complex flow problems, such as the tip vortex rudder interaction problem. A BEM based flow solver, PROPCAV for wetted hydrofoils is used to model this problem.

Initially, a line vortex/hydrofoil interaction model is implemented. The presence of the line vortex affects the inflow to the hydrofoil. Hence, by modifying the strength of the sources distributed on the hydrofoil panels, in terms of the new inflow, the effect of the line vortices on the hydrofoil is evaluated. The presence of a line vortex induces low pressures on the hydrofoil due to the strong inflow that it generates, and this is a concern for the inception of cavitation on the hydrofoil.

Next, a lifting line model for propeller flows is used to model the propeller blade tip vortices. A numerical model is developed to align the lifting line tip vortex with the total flow field in order to maintain the force free condition on the tip vortex wake. The lifting line tip vortex is discretized into line vortex elements and the total

velocity on the tip vortex wake is evaluated. Each point on the tip vortex wake is aligned with the total flow field by first rotating it about the original slipstream of the wake and then modifying the wake to account for the wake induced velocities. The contraction of the slipstream can be seen in the aligned tip vortex wake. Also, the tangency of the total velocity vectors and the directional vectors of the wake, and the angle between these vectors show that the wake is aligned to the total flow field. Various studies and tests verify the convergence process.

Finally, line vortex/hydrofoil interaction model and the wake alignment routine are coupled to evaluate the effect of the aligned tip vortex wake on the rudder. At each alignment iteration step, the problem for the flow around hydrofoil is solved with the altered inflow velocity and the total velocity field which also includes the induced velocity of the hydrofoil and its wake is evaluated. Then the wake geometry is changed to account for this total flow field. This process is repeated until the tip vortex wake aligns to the total flow field. The pressure distributions on the hydrofoil confirm the fact that the tip vortices induce low pressures on the rudder surface. A distribution of the C_{Pmin} with the lifting line angle gives an insight to the possible cavitation inception.

8.2 Recommendations for Future Work

Further study is required before the propeller blade tip vortex wake/rudder interactions model can predict accurate results for the flow around the rudder. Improvements are also needed on the model to reduce computational time. The following can be done to improve the interaction model:

- It is anticipated that a vortex model with a cavity core should be able to convect the vortex without significant dissipation and thus predict the hydrofoil vortex interactions more accurately. The two-phase FLUENT option should be utilized in this case. Then the results from the cavity core model from FLUENT can be compared with our model for the line vortex/hydrofoil interactions.
- The wake alignment technique needs to be studied further to make it more efficient and accurate. Also, the alignment technique does not seem to work for higher values of the vortex strength Γ . This needs to be investigated and corrected.
- The present model has to be extended for the case of a rudder subject to the slipstream of a Z bladed propeller. As a first step, this must be done in the case of Z lifting lines.
- The tip vortex/rudder interaction model needs to be implemented for the case with cavitation on the rudder surface. This requires some additional changes in the hydrofoil version of PROPCAV. Then the unsteady cavitation results can be compared with the cavitation results for the case of circumferentially averaged propeller flow/rudder interactions and the difference between the averaged and the unsteady results can be compared to check the validity of the models.
- Vortex trajectories, pressure distributions and cavity planforms from the current model should be compared with the measured quantities in experiments like those of Kracht [1989a] and Kracht [1989b].

Bibliography

- Achkinadze, A. S., Berg, A., Krasilnikov, V. I., and Stepanov, I. E. (2003). Numerical analysis of podded and steering system using a velocity based source Boundary Element Method with modified trailing edge. In *Propellers/Shafting '03 Symposium*, pages 1–22, Virginia Beach, VA. Society of Naval Architects and Marine Engineers.
- Ananthan, S., Leishman, J. G., and Ramasamy, M. (2002). The role of filament stretching in the free-vortex modeling of rotor wakes. In *58th Annual Forum and Technology Display of the American Helicopter Society International, Montreal Canada, June 11-13, 2002*.
- Crimi, P. (1965). Theoretical Prediction of the Flow in the Wake of a Helicopter Rotor. Technical Report BB-1994-S-1, Cornell Aero. Lab.
- Fine, N. E. and Kinnas, S. A. (1993). The nonlinear numerical prediction of unsteady sheet cavitation for propellers. In *Sixth International Conference On Numerical Ship Hydrodynamics, August 1993*, University of Iowa, Iowa.
- Greco, L. and Salvatore, F. (2004). Numerical modeling of unsteady hydrodynamics characteristics of a propeller rudder configuration. In *9th symposium on Practical Design of Ships and Other Floating Structures (PRADS2004)*, Luebeck-Travemuende, Germany.

- Han, J. M., Kong, D. S., Song, I. H., and Lee, C. S. (2001). Analysis of cavitating flow around the horn-type rudder in the race of a propeller. In *CAV2001: Fourth International Symposium on Cavitation*, California Institute of Technology, Pasadena, CA.
- Hsin, C. Y. (1990). *Development and Analysis of Panel Methods for Propellers in Unsteady Flow*. PhD thesis, Department of Ocean Engineering, Massachusetts Institute of Technology.
- Katz, J. and Plotkin, A. (2002). *Low-Speed Aerodynamics*. Cambridge University Press, 1st edition.
- Kerwin, J. E., Kinnas, S. A., Lee, J.-T., and Shih, W.-Z. (1987). A Surface Panel Method for the Hydrodynamic Analysis of Ducted Propellers. *Trans. SNAME*, 95.
- Kinnas, S. A. (2006). BEM Class Notes. Lecture notes for CE380P 4-Boundary Element Methods.
- Kinnas, S. A. and Fine, N. E. (1992). A nonlinear Boundary Element Method for the analysis of unsteady propeller sheet cavitation. In *Nineteenth Symposium on Naval Hydrodynamics, August 1992*, pages 717–737, Seoul, Korea.
- Kinnas, S. A. and Fine, N. E. (1993). A Boundary Element Method for the analysis of the flow around 3-d cavitating hydrofoils. *Journal of Ship Research*, 37:213–224.
- Kinnas, S. A. and Hsin, C. (1992). A Boundary Element Method for the analysis of the unsteady flow around extreme propeller geometries. *AIAA Journal*, 30 (3):688–696.

- Kinnas, S. A., Lee, H. S., Gu, H., and Natarajan, S. (2006). Prediction of sheet cavitation on a rudder subjected to propeller flow. *Journal of Ship Research (accepted)*.
- Kracht, A. M. (1989a). Rudder in the slipstream of a propeller. In *Proceedings of International Symposium on Ship Resistance and Powering Performance*, Shanghai, China.
- Kracht, A. M. (1989b). Ruderentwurf, Teil I. Technical Report 1137/89, Versuchsanstalt für Wasserbau und Schiffbau.
- Krishnamoorthy, S., Gossler, A. A., and Marshall, J. S. (1999). Normal vortex interaction with a circular cylinder. *AIAA Journal*, 37:50–57.
- Kuiper, G. (2001). New developments around sheet and tip vortex cavitation on ship propellers. In *CAV 2001: Fourth International Symposium on Cavitation, June 20-23, 2001*, California Institute of Technology, Pasadena, CA, USA.
- Lee, H. S. and Kinnas, S. A. (2001). Modeling of unsteady blade sheet and developed tip vortex cavitation. In *CAV 2001: Fourth International Symposium on Cavitation, June 20-23, 2001*, Pasadena, CA. California Institute of Technology.
- Lee, H. S. and Kinnas, S. A. (2004). Application of BEM in the prediction of unsteady blade sheet and developed tip vortex cavitation on marine propellers. *Journal of Ship Research*, 48 (1):15–30.
- Lee, J.-T. (1987). *A Potential Based Panel Method for The Analysis of Marine Propellers in Steady Flow*. PhD thesis, Department of Ocean Engineering, Massachusetts Institute of Technology.

- Li, H., Burggraf, O. R., and Conlisk, A. T. (2004). On the Formation of a Rotor Tip-Vortex. *Journal of Aircraft*, 39(5):739–749.
- Liu, X. and Marshall, J. S. (2004). Blade penetration into a vortex core with and without axial core flow. *Journal of Fluid Mechanics*, 519:81–103.
- Morino, L. and Kuo, C. C. (1974). Subsonic Potential Aerodynamic for Complex Configurations : A General Theory. *AIAA Journal*, 12(2):191–197.
- Mueller, A. C. and Kinnas, S. A. (1999). Propeller sheet cavitation predictions using a panel method. *Journal of Fluids Engineering*, 121:282–288.
- Newman, J. N. (1985). Distributions of sources and normal dipoles over a quadrilateral panel. *Journal of Engineering Mathematics*, 20(2).
- Pyo, S. and Suh, J. (2000). Numerical prediction of open water performance of flapped rudders. *Journal of Ship and Ocean Technology*, 4:1–10.
- Ramasamy, M. and Leishman, J. G. (2002). Reynolds number based tip vortex model. In *61st Annual Forum and Technology Display of the American Helicopter Society International, Montreal Canada, June 2002*.
- Rockwell, D. (1998). Vortex-Body Interactions. *Annual Review of Fluid Mechanics*, 30:199–229.
- Sadler, S. G. (1971). Development and Application of a Method for Predicting Rotor Free Wake Positions and Resulting Rotor Blade Air Loads. Technical Report NASA CR-1911, National Aeronautics and Space Administration.

- Wood, T. H. and Grace, S. M. (2001). Wing geometry effect on Blade Vortex Interaction response using BEM. In *Proceedings of 2001 ASME International Mechanical Engineering congress and Exposition, November 2001*, New York, NY, USA.
- Young, Y. and Kinnas, S. A. (2001). A BEM for the prediction of unsteady midchord face and/or back propeller cavitation. *Journal of Fluids Engineering*, 123(2):311–319.
- Young, Y. L. and Kinnas, S. A. (1999). Numerical and experimental validation of a cavitating propeller BEM code. In *Cavitation and Multiphase Flow Forum*, San Francisco, CA. 3rd ASME/JSME Joint Fluids Engineering Conference.
- Young, Y. L. and Kinnas, S. A. (2003). Analysis of supercavitating and surface-piercing propeller flows via BEM. *Journal of Computational Mechanics*, 32(4-6):269–280.

Vita

Fahad Mohammed was born in Guntur, India on March 4, 1982. He is the son of Mohammed Feroze and Hajira Feroze. He obtained his Bachelor of Technology in Naval Architecture and Ocean Engineering from the Indian Institute of Technology at Madras in July 2004. He started his Masters program in civil engineering at The University of Texas at Austin in September 2004.

Permanent address: 29/A MIGH Flat-103 Vengal Rao Nagar,
Hyderabad, India

This thesis was typeset with \LaTeX^\ddagger by the author.

[‡] \LaTeX is a document preparation system developed by Leslie Lamport as a special version of Donald Knuth's \TeX Program.